Optimising the Divergence Method

An investigation of methodology variations and corrections for global TROPOMI methane observations

Théo Huegens

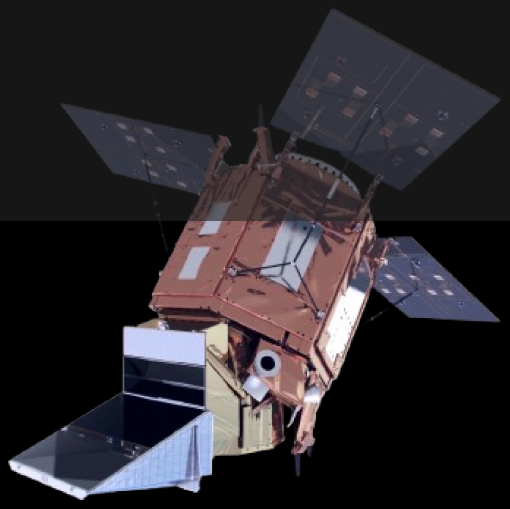

Delft University of Technology

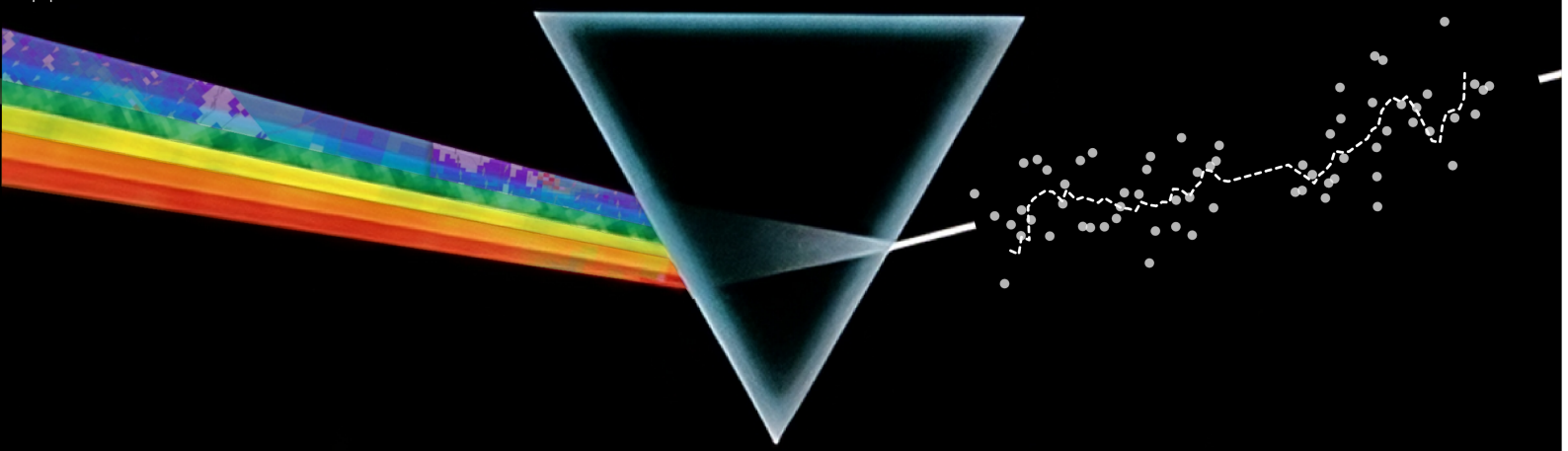

TU Delft

Optimising the Divergence Method

An investigation of methodology variations and corrections for global TROPOMI methane observations

by

Théo Huegens

to obtain the degree of Master of Science
at the Delft University of Technology,
to be defended publicly on 20/08/2025.

Student number:	5073502	
Project duration:	November 15, 2024 – August 20, 2025	
Thesis committee:	Dr. C. Roberts,	SRON, daily supervisor
	Dr. J. D. Maasakkers,	SRON, supervisor
	Prof. dr. ir. W. Van der Wal,	TU Delft, supervisor
	Prof. Dr. Ir. P.N.A.M. Visser	TU Delft, Chair
	Dr. S. (Sijme-Jan) Paardekooper	TU Delft, Examiner

Style:	TU Delft Report Style, with modifications by Daan Zwaneveld
Cover:	Own composition from ESA Sentinel-5P, Pink Floyd's dark side of the moon cover and results of this report

An electronic version of this thesis is available at http://repository.tudelft.nl/.

TU Delft

Preface

This thesis marks the culmination of an intensive period of learning, research, and personal growth. It would not have been possible without the invaluable support, guidance, and encouragement of many people, to whom I would like to express my deepest gratitude.

First and foremost, I would like to thank Clayton Roberts for his continuous and concrete support throughout this project. His insightful advice and critical feedback have been instrumental in shaping both the direction and quality of this work. I am equally grateful to Bram Maasakkers, whose experience in scientific research provided a solid foundation and perspective that helped me navigate various challenges. To Wouter van der Wal for his supervision and support through TU Delft, which played a vital role in the academic and structural development of this thesis.

For technical guidance and practical solutions, I woudl like to acknowledge Tobias de Jong, whose advice on coding best practices and python solutions proved immensely helpful. A sincere thank you to Shubham Sharma as well, for providing the WRF-Chem simulations used in this study. I am also grateful to Candice Chen for handing over her CH4 divergence codebase, which served as the foundation for the methodological framework of this research.

The whole SRON Earth group also deserves recognition for their essential contributions. Specifically for providing the TROPOMI methane data product, which gave me access to the array of existing geospatial codebases, and for constructive feedback on both the methodology and results. Their collective expertise and resources were pivotal to the success of this work.

On a more personal note, I wish to extend my heartfelt gratitude to Digna Jonikaitė, my fiancée, for her unwavering support, love, and patience throughout this journey. To my family and friends, thank you for your encouragement, understanding, and for keeping me grounded.

To all those mentioned, and those who offered support in big or small ways, thank you.

Théo Huegens
Delft, August 2025

Summary

Methane (CH4) is a potent greenhouse gas (GHG) with a global warming potential (GWP) 20-80 times that of carbon dioxide (CO2)(Balcombe et al. 2018). Knowledge of methane source's location and emission rates is essential for informing climate mitigation efforts. Space-based instruments like TROPOMI enable daily global monitoring of methane concentrations, but current estimation techniques often depend on tailored inverse models which are computationally expensive or rely on bottom-up inventories which only consider previously reported sources. Recently, divergence-based (DIV) techniques have emerged as a promising physics-driven framework for estimating emissions using concentration and wind fields obtained from satellites and reanalysis products of observational data, respectively. These approaches are computationally lightweight, reproducible, and avoid the need for training data or region-specific calibration from the user.

Although early studies have demonstrated their potential for various trace gases, including methane, key aspects of the method, such as background corrections and sensitivity, remain insufficiently explored in applied settings. In particular, there remains a lack of systematic research on how to best configure these methods for global application using TROPOMI observations. Most previous studies have been limited to simplified scenarios such as Gaussian plume simulations or have examined only selected components of the methodology, including specific estimator types or correction schemes. Notably, the two leading techniques used to account for background methane: pressure- and topographic-corrections, have not been compared under the same conditions, making it difficult to determine their relative performance. This study thus addresses the research question *"Which combinations of divergence method parametrisations yields the most accurate estimates of emission for TROPOMI methane observations?"* by implementing and testing a broad range of divergence method variations across three levels of complexity: idealized Gaussian plumes, simulated point-source emissions from a chemistry transport model (WRF), and a real world case study in the Permian Basin using TROPOMI satellite data.

Among configurations tested on background-free observations from WRF data, numerical gradient approximation methods were found to have only a minor influence on overall accuracy, with differences below 2% between the second-order (2), fourth-order (4), and combined fourth- and second-order (combo) schemes. The choice of order of operations in the estimator proved more consequential: Averaging the methane fluxes before applying the gradient operator lowered errors in emission estimations under 5% compared to divergence-averaged estimators, which were more sensitive to errors in the wind field and missing data, leading to error levels of 20 to 25%. Background tracers were then added to compare the background corrections. The topography-based approach was found to be unusable in global applications due to its sensitivity to the scale height parameter H, which must be fitted through simulations. Using physics-based approximations of H for methane yielded unpredictable error levels of 50 to 1000%. The pressure-based correction was thus used as a more reliable option with errors in the 10 to 50% range. The optimal configuration yielded monthly estimates for the Permian Basin emissions of 2019, averaging $3.39Tg$ with a monthly variability of $\pm 2.17Tg$, aligning well with previous studies. We found that extending the method to other years showed an increase of $2.14Tg$ on the 2023-2024 period compared to 2018-2022, which may be due to the recent increase in oil and gas production of the region highlighted by Varon et al. 2025.

Contents

List of Figures

List of Tables

Nomenclature

Abbreviations

Abbreviation	Definition
AMF	Air-mass factor
AK	Averaging Kernel (TROPOMI instrument's altitude sensitivity)
ALSW	Surface Albedo in SWIR band
AROP	Aerosol Optical Thickness
BM3D	Block Matching and filtering
CAMS	Copernicus Atmosphere Monitoring Service
CDS	Copernicus Climate Data Store
CF	Cloud Fraction
CH4	Methane
CO	Carbon monoxide
CO2	Carbon dioxide
CSF	Cross-sectional Flux Estimation (method)
CNN	Convolutional Neural Network
CTM	Chemical Transport Method
DIV	Divergence (method)
EAC4	ECMWF Atmospheric Composition reanalysis 4
ECMWF	European Centre for Medium-Range Weather Forecasts
ERA-5	Fifth generation ECMWF ReAnalysis
GEOS	Goddard Earth Observing System
GEOS-FP	Goddard Earth Observing System Forward Processing
GHG	GreenHouse Gas
GWP	Global Warming Potential
IME	Integrated Mass Enhancement
ISA	International Standard Atmosphere
IR	InfraRed
lat	Latitude
lon	Longitude
latlon	Latitude-longitude coordinates
lv2	TROPOMI operation level two data
LS	Least-Squares fitting
nan	Not A Number
NOx	NO (nitrogen oxide) and NO2 (nitrogen dioxide)
NOAA	National Oceanic and Atmospheric Administration
NIR	Near-InfraRed
ML	Machine Learning
PAL	Product Algorithm Laboratory
PBL	Planetary Boundary Layer
ppb	Particle Per Billion
ppm	Particle Per Million
ppbv	Particle Per Billion per Volume
SA	Surface altitude
SAA	Solar Azimuth Angle

Abbreviation	Definition
SP	Surface Pressure
SRON	Netherlands Institute for Space Research
SNR	Signal-to-Noise Ratio
SWIR	Short-Wave InfraRed
SZA	Solar Zenith Angle
TROPOMI	Tropospheric Monitoring Instrument
TVCD	Total Vertical Column Density
UV	Ultraviolet
UVIS	Ultraviolet-Visible
UVN	TROPOMI's (UV, UVIS and NIR) spectrometers and calibration unit
V&V	Verification and Validation
qa	Quality assurance value
WRF	Weather Research and Forecasting Model

Symbols

Symbol	Definition	Unit
E	Source magnitude	[kg/h]
F	Mass flux	[kg/s]
M	Mass	[kg]
Q	Emission rate	[ton/h]
S	Sink magnitude	[kg/h]
$\bar{U}$	Wind vector	[m/s]
U	Wind magnitude	[m/s]
U_{eff}	Effective wind speed	[m/s]
$U10$	10m resolution wind velocity in east-west direction	[m/s]
$V10$	10m resolution wind velocity in north-south direction	[m/s]
V	Volume	[m^3]
$XCH4$	Column-averaged dry-air mole fraction of methane	[ppbv]
W	Pixel resolution	[m]
ρ	Density	[kg/m^3]
Ω	Methane column density	[g/m^2]
$\Delta\Omega$	Methane column mass enhancement above background levels	[kg/m^2]
∇	Divergence operator	NA

1

Introduction

Methane (CH4) is a potent greenhouse gas (GHG), second only to carbon dioxide (CO2) in its global warming impact. The Intergovernmental Panel On Climate Change (Ipcc) 2023 indicates that CH4 contributed 0.28^oC to the total global warming of 1.1^oC since pre-industrial times. Accurate knowledge of atmospheric concentrations of methane and the location and quantities of emissions is thus essential for understanding its role in climate change and for identifying effective mitigation strategies. Satellite-based observations, such as those provided by the TROPOMI instrument, offer a unique opportunity to monitor methane emissions globally. However, many existing estimation methods are either tailored to specific cases, rely on computationally expensive simulations or require prior information from bottom-up emission estimates. While machine learning (ML)-based approaches offer an alternative, they are expensive to train and require extensive training data. In contrast, the physics-based divergence methods (DIV) have recently attracted attention due to their potential to provide fast emission estimates without relying on training sets or domain-specific parameters. The background components of CH4 concentration fields were shown to require a correction when using the divergence method (Liu et al. 2021) which may be done based on surface altitude (Sun 2022) or pressure (Veefkind et al. 2023). Other variations such as the choice in order of operations or numerical gradient approximations (De Foy and Schauer 2022) can also significantly impact the emission estimations' accuracy and robustness.

Although studies investigated the impact of methodology variations in the DIV method (Koene, Brunner, and Kuhlmann 2024) or applied it to TROPOMI CH4 (Veefkind et al. 2023), no systematic research has been conducted to find the most effective combination of divergence methods for TROPOMI-based methane estimation. Existing investigations have mostly focused on idealized test cases such as Gaussian-shaped plumes (Roberts et al. 2023) or have examined only a subset of possible methodological variations such as estimators (Rey-Pommier et al. 2025). Notably, both of the most promising methods for handling the background signal in CH4, that is, the topographic and pressure corrections, have not been compared on a similar basis. This highlights the need for a comprehensive evaluation of the divergence method's implementations to establish a robust and globally applicable configuration.

This thesis aims is to examine a wide range of variations in parameters, corrections and implementation of the divergence method proposed in literature and evaluate their respective performance on globally-applicable TROPOMI CH4 observations. To this end, simplified Gaussian models and simulated chemical transport model (CTM) observations of steady methane point sources will be used to assess the performance of various DIV configurations. Finally, a yearly emission estimation of the Permian basin based on real TROPOMI CH4 observations will be compared to literature emission estimates as a case study.

First, chapter 2 gives an overview of the DIV method's position within the current remote sensing landscape and its working principle. The research objectives, questions and approach are discussed in chapter 3. The data sources used and implementation solutions along with the verification steps taken are then described in chapter 4. Finally, the results are presented and reviewed in chapter 5 while the conclusions are outlined in chapter 6.

2

Background and Fundamentals

This chapter will start with a brief reminder on the role of methane in climate change (section 2.1) and the methods used for space-borne remote sensing of trace gases in our atmosphere section 2.2. Current state-of-the-art methodologies for estimating the location and emission rates of methane sources based on satellite observations will then be reviewed in section 2.3 before delving into the divergence method (section 2.4), its history and peculiarities compared to other methods, detailed working principle and applications.

2.1. The role of methane in climate change

The current state of the climate shows a consistent increase in global temperatures, driven largely by greenhouse gas emissions, including methane (Intergovernmental Panel On Climate Change (Ipcc) 2023). Methane (CH4) is a potent greenhouse gas (GHG) with a global warming potential (GWP) 20-80 times greater than that of carbon dioxide (CO2), depending on the time horizon considered (Balcombe et al. 2018). Additionally, methane also acts as a precursor to tropospheric ozone which impacts air quality and contributes to global warming (Shindell et al. 2012). Methane, like CO2, is a quasi-stable gas in the atmosphere with an atmospheric lifetime of 9.1 years $\pm$ 0.9 years (Intergovernmental Panel On Climate Change (Ipcc) 2023). This distinguishes it from other trace gases like nitrogen oxides (NO and NO2, abbreviated NOx) which have a lifetime of $\tau = 4.3 \pm 1.3$ hours before degrading into ozone (O3).

Anthropogenic methane emissions, primarily from agriculture, fossil fuel extraction, and landfills (Saunois et al. 2020) have shown a concerning upward trend from the 2000-2009 period to the 2010-2019 period (Saunois et al. 2024). Natural fluxes, from the freshwater and wetlands in particular, also contribute a significant portion of natural methane emissions and absorption and are sensitive to climate change themselves(Peng et al. 2022).

The Global Methane Pledge thus set a target in 2021 as part of the Paris Agreements to significantly reduce global methane emissions by 2030 (Commission and America 2021), making CH4 a primary target for near-term climate strategies and mitigation actions. Since methane emissions are subject to unexpected leaks from oil and gas operations or coal mines in particular and have both natural and anthropogenic contributions, tracking the reduction efforts towards this objective will require comprehensive, real-time methane monitoring to track emission sources and identify mitigation opportunities (European Commission. Joint Research Centre. 2017). The need for regular and accurate methane observations is, therefore, critical to meeting these ambitious climate targets and to ensure that emission reductions are achieved in a timely manner.

2.2. Remote sensing observations applied to methane

These sections will go through the working principle of trace-gas retrievals in subsection 2.2.1 before discussing the specificities of the TROPOMI instrument in particular in subsection 2.2.3.

2.2.1. Working principle

Remote sensing instruments used for trace gas detection typically consist of spectrometers operating in the short-wave infrared (SWIR) region of the electromagnetic spectrum. These instruments measure the amount of light coming from earth within each frequency bin. The width of those bins is the characteristic 'spectral resolution' of the instrument while the size of the ground area observed per spectra is the 'spatial resolution' of the instrument. The spectra measured at each pixel is called the level-1 data product of the instrument.

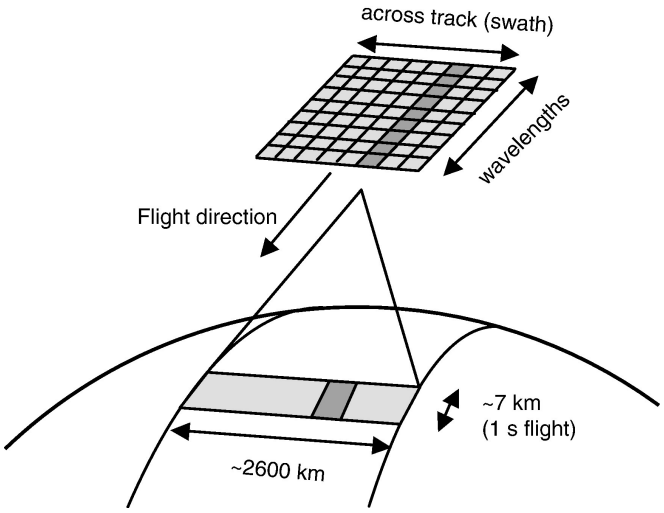

Figure 2.1: Schematic showing how the 2D sensor of TROPOMI maps onto one ground dimension and one spectral dimension for one-second observation. Figure taken from Veefkind et al. 2012

By comparing the initial, known, sun spectra with the measurements of the light which has travelled through the atmosphere, reflected on the ground and travelled back out of the atmosphere before hitting the satellite's pixels and considering the characteristic bands at which methane tends to absorb light it is possible to 'retrieve' the amount of methane in the atmospheric column observed within each pixel (Rodgers 2000). The resulting estimates in atmospheric methane column concentrations in parts per million (ppm) is also called the level 2 data product or 'observation'.

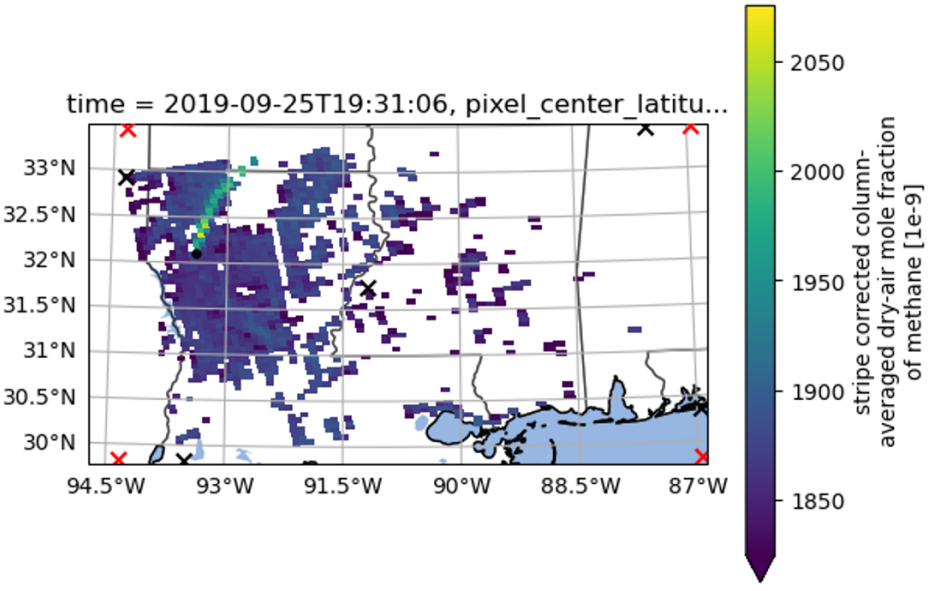

Figure 2.2: TROPOMI observation of a plume in Louisiana on 25/09/2019.

An example of a TROPOMI methane observation can be seen in Figure 2.2 where a source (indicated by a black dot) emits methane into the atmosphere at some mass flow, assumed constant over the observation time, called the 'source rate' $Q(kg/h)$. This CH4 is then transported by the environment's wind (advection) and scattered by the random, turbulent currents of the atmosphere (turbulent diffusion) (Roberts et al. 2023) eventually fading out into a fan. The observed quantity shown in Figure 2.2 is the column-averaged dry-air mole fraction of methane $XCH_4(ppbv)$. This value can then be converted to molar column densities $n_{CH4}(mol/m^2)$ or enhancements $\Delta n_{CH4}(mol/m^2)$ in case the local background is substracted. A unit change is generally performed on column mass densities $\Omega(g/m^2)$ to be used as an input for the estimation models (Koene, Brunner, and Kuhlmann 2024) in order to more directly yield a source rate in (ton/h). Quantifying the source rate from such observations is a hard inverse problem with complications such as measurement noise, wind direction and magnitude uncertainties as well as missing data due to clouds or water surfaces.

2.2.2. Methane-capable instruments

There are a number of current and planned methane monitoring satellites which differ in various spatial and spectral resolution resulting in a range of trace gas sensitivity and coverage. For example, satellites like GOSAT (Greenhouse Gases Observing Satellite) and MethaneSAT are designed with advanced spectrometers to detect methane concentrations at varying resolutions. GOSAT has been operational since 2009, providing global methane measurements, while the newly launched MethaneSAT offers enhanced capabilities specifically for detecting methane leaks and emissions. Similarly, the CO2M mission will provide high-resolution observations of methane alongside carbon dioxide, contributing to more comprehensive climate monitoring.

Table 2.1: Comparison of the capabilities of various methane observation instruments in operation (as of 13/01/2025). The return time is the 'Time interval between successive viewings of the same scene'. Table summarised from Table 1 of Jacob et al. 2022

Satellite	launch year	spectral resolution (nm)	spatial resolution (km)
GOSAT	2009	0.06	10 x 10
GHGSat	2016	0.3	0.025 x 0.025
TROPOMI	2017	0.25	5.5 x 7
PRISMA	2019	10	0.030 x 0.030
MethaneSAT	2024	0.3	0.13 x 0.4
CarbonMapper	2023	6	0.030 x 0.030
Sentinel-5	2025	0.25	7.5 x 7.5
CO2M	2025	0.3	2 x 2

These instruments are typically separated into two distinct categories: The first are the 'area flux mapper' which measure atmospheric methane concentrations across a broad, low resolution swath. These satellites are used for monitoring and detection as thanks to their wide coverage and repeated observations of the same areas. The second is made up of 'point source imagers' which offer high spatial resolution and are used to provide more detailed observations on specific facilities or areas of interest. Since point source imagers have a limited field of view they cannot be used for detection and are pointed by operators to get more precise information on sources detected through other means e.g. area flux mappers. By combining data from satellites observing the same area at different overpass times, researchers can generate a time series of methane concentrations or pinpoint specific point sources using a point source imager spacecraft after an area flux mapper identified an area of interest - providing critical insights into methane dynamics and supporting climate mitigation efforts.

2.2.3. Sentinel-5P and the TROPOMI instrument

The TROPOMI (Tropospheric Monitoring Instrument) aboard the Sentinel-5 Precursor (S-5P) satellite, launched in October 2017, provides continuous global coverage of atmospheric composition, offering daily measurements across the globe (Veefkind et al. 2012). TROPOMI uses ultraviolet (UV), ultraviolet-visible (UVIS), near-infrared (NIR) bands in its UVN module and the short-wave infrared (SWIR) band in the SWIR module which is cooled down to 200K, allowing it to observe a wide range of atmospheric constituents. In addition to methane (CH4) and carbon monoxide (CO) in the SWIR band, TROPOMI can

also monitor ozone (O_3), nitrogen oxides (NOx), sulfur dioxide (SO_2), formaldehyde (CH_2O), aerosols, and clouds, making it a versatile tool for atmospheric monitoring.

TROPOMI's methane retrievals from the SWIR bands are known to have a 2% accuracy and 0.6% precision under cloud-free conditions (Veefkind et al. 2012) which was validated to a precision of 3.4 ± 5.6 ppb once the retrieval of the observation has been executed (Lorente et al. 2021). However, since the accuracy of methane measurements are dependent on the presence of e.g. clouds or water which reflect light differently resulting in some pixels being masked out of the observation in order to keep only the measurements whose confidence is high. The instrument has a wide swath of 2600 km and its spatial resolution is 5.5 km by 7 km (Figure 2.1) which is relatively fine for flux-area mapper satellites. This is distinct from point-source imagers which can achieve resolutions on the order of the meter but need to be pointed at an area of interest.

TROPOMI has been proven to be effective in detecting methane emissions from various sources, including both point-source plumes and diffuse emissions. Studies such as those by Jacob et al. 2022 or Maasakkers et al. 2022 have demonstrated its capabilities in detecting methane emissions, making it a crucial tool for facility-level detection of methane leaks. In particular, methane sources with very high emission rates from a single facility, called super-emitters (Plant et al. 2022) have been a primary target for methane mitigation strategies. TROPOMI allowed the automated detection of super-emitters using a convolutional neural network (CNN) providing a weekly catalogue of high-priority mitigation actions (Schuit et al. 2023).

2.3. Emission estimation methodologies

This section explores various source rate estimation methods for trace gases using satellite observations, with a particular focus on methane observations from the TROPOMI satellite.

2.3.1. Inverse methods

Inverse methods consist use chemical transport models (CTM), a type of atmospheric transport simulations which track chemical species such as methane through air masses, to find what source conditions should have been to result in the concentration field observed by satellite. Since atmospheric transport is ruled by Navier-Stokes equations which are unsolvable, approximations and pre-computed meteorological fields are used to make up a forward model. An alternative approach is the Lagrangian particle dispersion model which tracks the movement of individual particles in the atmosphere to simulate the dispersion of pollutants (Figure 2.5). While more computationally demanding than the Gaussian approach, this can provide a more accurate representation of plume dynamics and is applied extensively in research (Lauvaux et al. 2022, Delfi et al. 2019, Freitas and Fornaro 2022, Crosman 2021) using the NOAA's HYSPLIT model (NOAA 2025b).

By assuming a source location and emission rate (circle in Figure 2.3), the forward model can transport the methane compounds to obtain a resulting plume structure (thick lines in Figure 2.3). Minimising the difference between this result and the observation (thin lines in Figure 2.3) by tweaking the various parameters can lead to an accurate and robust estimation as demonstrated for CO2 by Broquet et al. 2018, Houweling et al. 2015 and Ye et al. 2020. An example of such an extensive CTM is the GEOS-Chem model (NASA 2025)

Figure 2.3: Illustration of a complex atmospheric transport model fitted to a plume observation.

Figure 2.4: Illustration of a Gaussian plume model fitted to a plume observation.

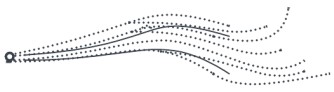

Figure 2.5: Illustration of a Lagrangian particle dispersion model fitted to a plume observation.

Bottom-up inventories, such as those provided by EDGAR (Emissions Database for Global Atmospheric Research) and CAMS (Copernicus Atmosphere Monitoring Service), are commonly used to relate remote sensing observations to known emission sources (Jacob et al. 2016) and give a starting

point (also called a 'prior') to these inversion methods. These inventories gather data from various sectors including natural sources, agriculture, fossil fuel combustion, and industrial activities from facility to regional level. While these inventories provide a useful resource for understanding emissions at a global scale and how their sources are distributed (Alvarez et al. 2018) they only account for the reported anthropogenic sources that can be measured directly which tends to result in under-estimations.

Furthermore, the many simulations that are required for inversion need substantial computational resources and are sensitive to a wide range of model parameters. As a result, they are often prohibitively expensive for high-resolution observations where small-scale effects such as turbulence and diffusion plays a non-negligible role in the species' distribution within the observed scene (Koene and Brunner n.d. This also makes it impractical for automated monitoring which is expected to process hundreds to thousands of plumes per year (Koene, Brunner, and Kuhlmann 2021).

Simplified models can be used to significantly reduce computational costs compared to full-scale atmospheric simulations. One of the simplest approaches is the Gaussian plume model (Figure 2.4), which assumes a steady-state turbulent diffusion from a point source (Stockie 2011). However, this model is limited in its application to methane plumes as most TROPOMI plumes are not Gaussian. Indeed, they are typically too small and localized for the assumptions of Gaussian dispersion to hold (Jongaramrungruang et al. 2019).

2.3.2. Physics-based methods

Physics-based approaches to emission estimation apply fundamental principles of mass conservation in order to quantify emissions. For a volume V bounded by surface s, the sum of the net mass flux of a non-reactive gas through s (F_s) and the accumulation of mass over time within that volume (M_V) corresponds to the magnitude of a net source (E) and/or sink (S) within that volume which can be interpreted as a source $Q = E - S$ (kg/s) (Koene, Brunner, and Kuhlmann 2024).

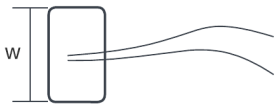

Figure 2.6: Illustration of the domain of a local mass balance of width W for near-source pixels.

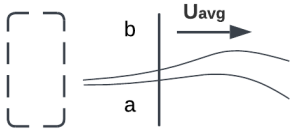

Figure 2.7: Illustration of a Cross-Sectional Flux (CSF) integral from a to b.

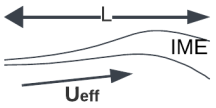

Figure 2.8: Illustration of the integrated mass enhancement (IME) with wind speed Ueff and characteristic plume length L.

If the source location is known the 'source pixel method' can be used as described in Jacob et al. 2016. This uses the ratio of the mean source pixel enhancement $\Delta\Omega(kg/m^2)$ with respect to the local background Ω_a along with the pixel dimension $W(m)$ colocated with a uniform wind vector $\bar{U}(m/s)$, surface pressure $p_s(Pa)$ and gravity constant $g_0(m/s^2)$ to directly infer a source rate $Q(kg/s)$ using Equation 2.1(Varon et al. 2018). This however results in noisy and uncertain estimates which requires researchers to average estimates over time.

$$Q_{pix} = \frac{\bar{U} \cdot W \cdot p}{g_0} \cdot \frac{\Delta\Omega}{\Omega_a} \tag{2.1}$$

The cross-sectional flux method (CSF) uses the same principle but instead evaluates a larger area by computing the cross-plume integral $C(kg/m^2)$, that is, the flux going through a user-defined boundary s, from a to b, perpendicular to the plume's direction i.e. the wind's mean direction within the area of interest ($\bar{U}_{avg}(m/s)$ (Figure 2.7). The source rate $Q(kg/s)$ upwind of s (Varon et al. 2018) is then estimated with Equation 2.2. In practice this is widely used with aircraft observations (White et al. 1976, Tratt et al. 2011 and Tratt et al. 2014) but often requires the computation of an indirect 'effective wind speed' (U_{eff}) or averaging of multiple cross-sections along the plume to improve accuracy.

$$Q_{CSF} = \int_a^b \Delta\Omega \cdot U_{avg} = C \cdot U_{eff} \tag{2.2}$$

The integrated mass enhancement (IME) method relates the total plume mass downwind of the source directly to the source rate. All the pixels comprising the plume structure are identified through a user-defined bounding box and summed up to find the IME (kg). This IME and other scalar values such as the effective wind speed U_{eff} (similar to the one computed for accurate CSF), characteristic plume length L (Figure 2.8) can then be used to estimate the source rate with Equation 2.3. Alternatively, these same values can be fed into a statistical or machine learning model which outputs a value for Q (Varon et al. 2018). This method is often used for (semi-)automated monitoring of trace gas but has limits due to its dependence on boundary definition (Schuit et al. 2023, Jacob et al. 2022, Cusworth et al. 2021).

$$Q_{IME} = \frac{U_{eff} \cdot IME}{L} \text{ with } IME = \Sigma_{j=1}^{N} \Delta\Omega_j \cdot A_j \tag{2.3}$$

2.3.3. Learning-based methods

Finally, machine-learning algorithms can be trained with a large set of input-output pairs (e.g. observation and source rate) in order to directly infer the source rate from a set of readily available inputs (Koene, Brunner, and Kuhlmann 2024). These training sets can be derived from real plumes whose source rate is estimated through other methods or simulated with a perfectly known source (also known as synthetic observations).

Convolutional Neural Networks (CNN) are a particular set of ML methods that take in a scene (aggregated observations over the area of interest) in matrix form (see Figure 2.9). The input is then multiplied by convolution kernels with trained weights to reduce the scene's size step by step, eventually yielding a vector and then a scalar point. This output is interpreted as the source rate Q. This was first applied to simulated observations of methane (Jongaramrungruang et al. 2021) with encouraging results but the generation of a training set and the validation of a non physics-based method poses numerous challenges.

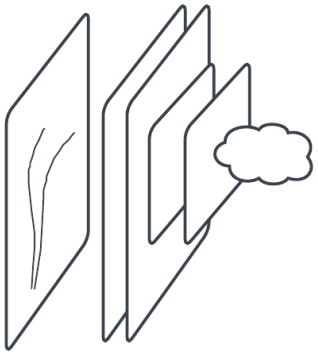

Figure 2.9: Illustration of a Convolutional Neural Network processing the plume for direct inversion.

2.4. The divergence method

This section will provide an introduction to the divergence method within the remote sensing scene in subsection 2.4.1 and a summary description of the divergence method's working principle and underlying mathematical foundations in subsection 2.4.2. The building blocks of the basic implementation and adaptations that have been explored in the literature to optimise the method for different species and satellite platforms will then be detailed in subsection 2.4.3, subsection 2.4.4, subsection 2.4.5 and subsection 2.4.6.

2.4.1. Introduction

The divergence method, introduced by Beirle et al. 2019, has emerged as a novel alternative to estimate trace gas emissions from satellite observations. This physics-based approach provides a better confidence and accuracy than the 'source-pixel' method while avoiding the user-defined domains of the CSF method. These characteristics makes it more suitable for large-scale use on area-flux mapper or applications without a-priori knowledge of the emission's location (see subsection 2.3.2).

Initially applied to TROPOMI NO2 data (Beirle et al. 2019), it was later extended to methane (Liu et al. 2021) as well as other trace gases such as carbon monoxide (CO) or carbon dioxide (CO2) in Hakkarainen et al. 2022 and applied to satellites such as GEMS (Xu et al. 2024).

2.4.2. Working principle

The divergence method (DIV) applies Gauss' theorem, also known as the divergence theorem, to rearrange the continuity equation such that the divergence of the flux $F_s = \Omega \cdot \bar{U}(kg \cdot m^{-2} \cdot s^{-1})$ is equal to the net source rate (Equation 2.4) (Beirle et al. 2019). This creates an emission map, that is, an estimation of the source rate within each pixel, at relatively low computational cost which can then be post-processed to find, fit or spatially integrate sources.

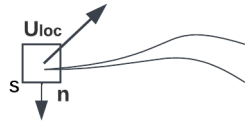

Figure 2.10: Illustration of a computation of the outward flux along a closed contour via the Divergence theorem.

$$\nabla F_s = E - S = Q(kg/s) \tag{2.4}$$

A notable difference between the CSF and DIV methods is that the CSF starts by defining the plume boundaries before computing the emissions whereas the divergence can identify sources after the computation has been done on a whole region, called 'domain'. Furthermore, the CSF is spatially averaged along the plume's length in a series of sections whereas the DIV method can average over multiple scenes taken at different times. This means the CSF is more suited for distinct, short-term plumes and the DIV is better at estimating low-emission sources emitting steadily over long periods.

The continuity equation (Equation 2.5) states that the difference between the net source rate $S[kg \cdot m^{-3} \cdot s^{-1}]$ in a region V and the time-varying accumulation of the mass $\frac{\delta\rho}{\delta t}$ equals the mass exiting the region's boundaries (Koene, Brunner, and Kuhlmann 2024). This is expressed by the flux vector $\bar{F} = \rho \cdot \bar{v}$ where ρ is the trace gas's concentration in $[kg \cdot m^{-3}]$ and $\bar{v}[m/s]$ is the transport vector (i.e. wind field).

$$\iiint_V \left(S_{(x,y,z,t)} - \frac{\delta\rho_{(x,y,z,t)}}{\delta t} \right) dV = \iiint_V \nabla \cdot \bar{F}_{(x,y,z,t;\rho,\bar{v})} dV \tag{2.5}$$

A series of assumptions taken from Koene, Brunner, and Kuhlmann 2024 below are then required to rearrange the steady-state continuity equation for all points (x_i,y_i) within S_a into Equation 2.6 in which each pixel's source is expressed in Q_i and required only the horizontal flux field $\bar{F}^Z$ to be computed. This creates an emission map for every valid pixel at relatively low computational cost which can be processed to find, fit or spatially integrate diffuse sources or plumes.

- *Assumption 1:* the mass flux $\bar{F}$ is dominated by advection, i.e. the diffusion of the trace gas cross-wind in negligible
- *Assumption 2:* the species does not leak to space or the ground ($\bar{F} \cdot \hat{n} = 0$)
- *Assumption 3:* the effective wind field $\bar{U}_{x,y}[m/s]$ (constant through the whole column altitude) can be computed accurately
- *Assumption 4:* the wind fields, sources and sinks are steady-state during the observation time
- *Assumption 5:* Sources $Q[kg/s$ can be expressed as the product of temporal ($Q_{(t)}$) and spatial ($Q_{x,y,z}$) distributions
- *Assumption 6:* Sinks $S[kg/s$ can be ignored ($S = 0$) or described by first-order reactions (see Equation 2.22)

$$\Sigma_i Q_i(t) = \iint_{S_A} \left(\nabla_{x,y} \cdot \bar{F}^Z(x,y,t) \right) dS_A \tag{2.6}$$

In practice, this method can be visualised as a series of operations steps on the 2D images from the satellite as follows: First, the effective wind field $\bar{U}[m/s]$ is co-located with the concentration grid $C[ppbv]$, expressed in units of column density $\Omega[g/m^2]$ as illustrated for a single pixel in Figure 2.11 and for a simplified Gaussian observation in Figure 2.15. Next, these fields are multiplied at each pixel location to obtain the effective flux $F[kg \cdot m^{-1} \cdot s^{-1}]$ [1] as shown in Figure 2.12 and Figure 2.16. Taking the gradient

[1] Flux units in some plots are shown as $kg \cdot m^{-2} \cdot s^{-1}$ but should be $kg \cdot m^{-1} \cdot s^{-1}$

$\nabla_{(x,y)}$ (i.e. the sum of the derivatives with respect to the x and y directions) of the flux field then yields the emission field $E_i(x,y)[kg \cdot s^{-1} \cdot m^{-2}]$ seen in Figure 2.14 or Figure 2.17 which can be multiplied by the pixel's area to get the source rates $Q_i(x,y)[kg \cdot s^{-1}]$. Alternatively, the last two steps can be done in reverse order: first computing the gradient of the column density field (see Figure 2.13) and then multiplying it by the wind field to obtain the emission field again. This variation is called 'directional derivative' (DD) and is mathematically equivalent since the gradient and multiplication operators are linear.

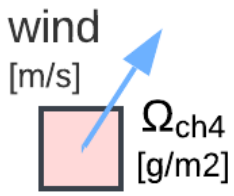

Figure 2.11: Illustration of a pixel with some concentration $\Omega[g/m^2]$ overlayed with a local wind vector $u[m/s]$.

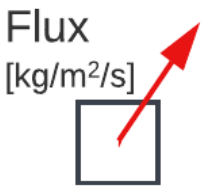

Figure 2.12: Illustration of a pixel's computed flux vector $F[g/m/s]$.

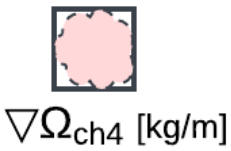

Figure 2.13: Illustration of the divergence of a pixel's concentration.

Figure 2.14: Illustration of the divergence of a pixel's flux i.e. the rate of mass increase (E) and decrease (S) within that pixel's column.

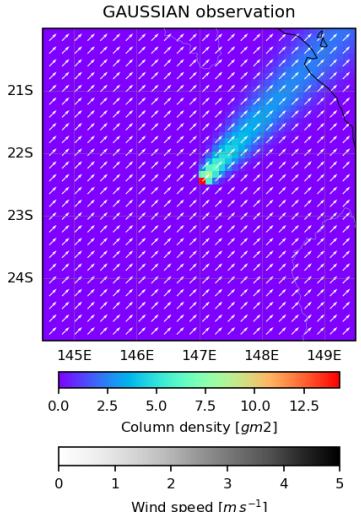

Figure 2.15: Illustration of a simplified plume observation's concentration field $\Omega[g/m^2]$ overlayed with a wind field $u[m/s]$.

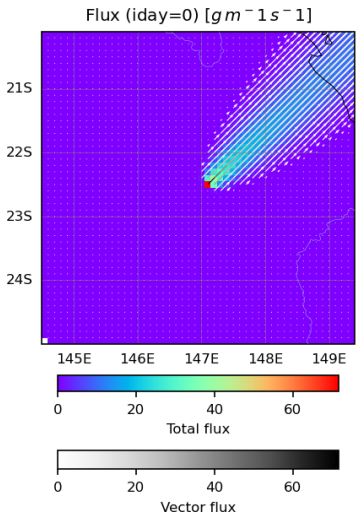

Figure 2.16: Illustration of a simplified plume observation's computed flux field $F[g/m/s]$.

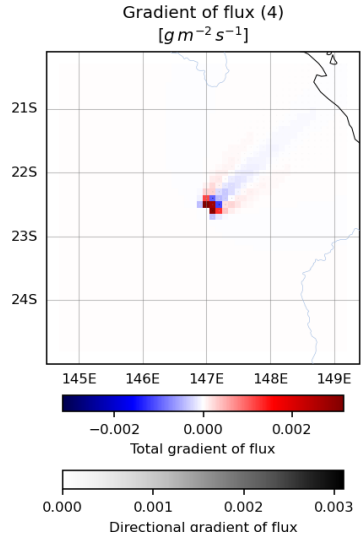

Figure 2.17: Illustration of the estimated emission field of a simplified plume i.e. the rate of mass increase (E) and decrease (S) within each pixel's column.

2.4.3. Gradient approximation

The gradient operator ∇ applied to a 2D field F is the sum of its directional derivatives with respect to axes x and y (see Equation 2.7). The components are thus computed separately and summed to a total as illustrated in Figure 2.18 where both $\frac{\delta F}{\delta x}$ and $\frac{\delta F}{\delta y}$ are local 1D derivatives.

$$\nabla(F) = \frac{\delta f}{\delta x} + \frac{\delta f}{\delta y} \tag{2.7}$$

Since the field is not continuously defined but instead discretised by pixels of size h x w [km] it is necessary to use a discrete approximation of the slope. Two are considered in literature (see Appendix A): the second-order approximation of the slope around some pixel at position $(x,y) = (i,j))$ defined in x (longitude axis) by Equation 2.8 and in y (latitude axis)by Equation 2.9 where h and w are the pixel's

height and width converted from degrees to metres and is accurate to some second-order term $\mathcal{O}$. This formulation requires four valid neighbouring pixels (the pixel evaluated is actually not needed) as shown in Figure 2.18. Similarly, a fourth-order approximation can be formulated in x by Equation 2.10 and y Equation 2.11 by extending the valid pixels required to eight neighbours and will have an error term $\mathcal{O}$ of order four. The trade-off that presents itself in choosing whether to use 2 or 4 is that 4 requires more valid pixels and is thus more sensitive to gaps in the scene whereas 2 has a lower-order error and will thus results in a more noisy and generally less accurate estimate.

$$\left(\frac{\delta f}{\delta x}\right)_{\mathcal{O}=2} = \frac{f(x, y+w) - f(x, y-w)}{2w} + \mathcal{O}_{(2)} = \frac{F(i, j+1) - F(i, j-1)}{2d_{lon}} + \mathcal{O}_{(2)} \tag{2.8}$$

$$\left(\frac{\delta f}{\delta y}\right)_{\mathcal{O}=2} = \frac{f(x+h, y) - f(x-h, y)}{2h} + \mathcal{O}_{(2)} = \frac{F(i+1, j) - F(i-1, j)}{2d_{lat}} + \mathcal{O}_{(2)} \tag{2.9}$$

$$\left(\frac{\delta f}{\delta x}\right)_{O=4} = \frac{f(x+2h, y) + 8f(x+h, y) - 8f(x-h, y) - f(x-2h, y)}{12h} + \mathcal{O}_{(4)} \tag{2.10}$$

$$\left(\frac{\delta f}{\delta y}\right)_{O=4} = \frac{f(x, y+2w) + 8f(x, y+w) - 8f(x, y-w) - f(x, y-2w)}{12w} + \mathcal{O}_{(4)} \tag{2.11}$$

Veefkind et al. 2023 added a non-pixel aligned finite difference approximation in the gradient computation using 8 gradient directions (4 orthogonal and 4 diagonal) as shown in Figure 2.19. In that case, the width and height can be expressed as $w' = h' = \sqrt{w^2 + h^2}$. This configuration will be referred to as "diagonal" gradients whereas the other will be referred to as "orthogonal" gradients. This allows a more accurate estimate of gradients in those diagonal directions and is particularly useful if a plume is narrow or the resolution is coarse as the enhancement or flux may only covers pixels e.g. $(i-1, j-1)$ and $(i+1, j+1)$ which would result in a net zero gradient if simply summing up the orthogonal components.

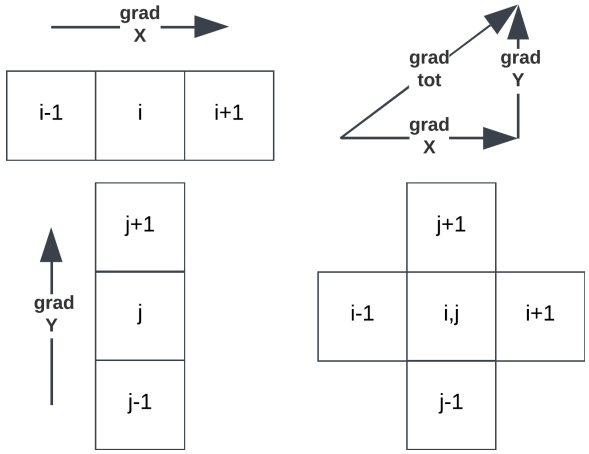

Figure 2.18: Representation of the neighbouring pixels considered for a second order orthogonal gradient approximation and the respective directions of computations.

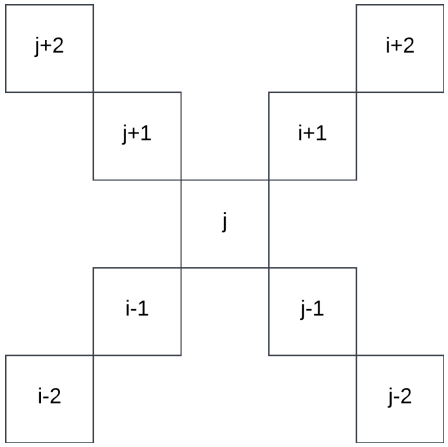

Figure 2.19: Representation of the neighbouring pixels considered for a fourth order diagonal gradient approximation.

Since gas plumes will generally flow in the direction of the wind, one can use the average wind direction Φ of a scene derived from the averages of the u and v components (Equation 2.12) to compute a directionally adaptive blending factor Equation 2.13 which gives more or less weight to either the orthogonal (maxima at $\Phi = 0, 90, 180, 270^o$) or diagonal (maxima at $\Phi = 45, 135, 225, 315^o$) gradients. Such an adaptive gradient direction will be referred to as "combo" and is computed with Equation 2.14.

$$\Phi = atan\left(\frac{v}{u}\right) \tag{2.12}$$

$$w_0 = ||\frac{\Phi}{45} - 1|| \tag{2.13}$$

$$\nabla_{combo} = w_0 \cdot \nabla_{ortho} + (1 - w_0) \cdot \nabla_{diag} \tag{2.14}$$

2.4.4. Variations in order of operations

The mathematical description of the basic divergence method, shown below in Equation 2.15, takes the gradient of the advective fluxes of a single observation. The fluxes are computed first as $F = \bar{u} \cdot \Omega$ based on the wind field $\bar{u}$ and column density field Ω while the gradient approximation described in subsection 2.4.3 would be applied next. However, even though all operators seen here are mathematically linear (the product here is applied pixel-wise, it is not a dot-product of the two matrices) the physical assumptions and numerical approximations used (see Equation 2.4.2) mean the order of operations has been observed to have a non-negligible effect on the results (De Foy and Schauer 2022), particularly when averaging over long time periods.

De Foy and Schauer 2022 thus proposed a different approach by altering the order of operations of the method with the aim of improving the handling of missing values and edges. Computing the fluxes over the whole period of interest (the 'flux-averaging period') first and then averaging them before computing the divergence. This method is referred to 'as (flux-averaged) divergence' and abbreviated E2. By contrast, the standard DIV method computes the divergence for each observation individually before averaging the emission maps and is henceforth referred to as E1 or the 'divergence (averaged)'' method.

$$\tilde{E}_{div} = \nabla \left(\bar{u} \cdot \Omega \right) \tag{2.15}$$

The first change in order of operation possible is to simply compute the gradient of the column density first and then multiply the result with the wind field. This is referred to as as the directional derivative method (abbreviated DD) and described per Equation 2.16 in contrast to the divergence method (abbreviated DIV) and described by Equation 2.15. The difference between DIV (Figure 2.14) and DD (Figure 2.13) on a single-observation of an idealised point-source, diffusion-corrected Gaussian plumes was seen to be on the order of $10^{-14} g/m^2$ compared to an estimated emission magnitude of $50g \cdot m^{-2} \cdot s{-}1$ which confirms both implementations are equally valid on perfect observations. This will however not hold when considering averaged observations, missing data, structured backgrounds and non-uniform wind fields (see subsection 5.2.4).

$$\tilde{E}_{dd} = \bar{u} \cdot (\nabla \Omega) \tag{2.16}$$

Averaging either DIV or DD results in the 'divergence averaged' (E1) and 'directional derivative averaged' (DD,avg) estimators. Both of which are implemented in the same way by taking the average of all emission grids generated over the period of interest for each observation. An alternative approach, first proposed by De Foy and Schauer 2022, is to first average the flux fields and only then take the gradient which results in a single emission grid. This will be referred to as the flux-averaged divergence estimator and abbreviate E2. All averaged estimators are presented in Equation 2.17. An analogous change for DD is excluded since taking the average of the concentration field separately from the wind field would not yield a flux field whose direction actually matches that of the gases observed.

$$\tilde{E}_{E1} = \langle \nabla \left(\bar{u} \cdot \Omega \right) \rangle \tag{2.17}$$

$$\tilde{E}_{E2} = \nabla \left(\langle \bar{u} \cdot \Omega \rangle \right) \tag{2.18}$$

$$\tilde{E}_{DD,avg} = \langle \bar{u} \cdot \nabla \left(\Omega \right) \rangle \tag{2.19}$$

Finally, because of the inherent noise observed in previous application of the divergence method (see Appendix A) and the need for temporal averaging to obtain usable results, only the averaged estimators E1, E2 and DD_avg will be considered going forward and their performance will be compared in

subsection 5.2.4. This of course limits the application of the divergence method presented here to long-term emitters whose source rate can be assumed steady such as the Permian region and excludes the study of short-lived, transient events such as the Louisiana blowout shown in Figure 4.1 which was seen in only a few TROPOMI observations or individual emission sources within the Permian basin.

2.4.5. Background correction

When Liu et al. 2021 adapted the divergence method to TROPOMI methane, the authors noted that methane's longer atmospheric lifetime compared to NO_x resulted in an inhomogeneous background component which needs to be subtracted to obtain the local enhancements which are indicative of local sources. Indeed Figure 2.20 shows worldwide observations for the year 2022 without any presampling, filtering or corrections of the methane $CH_4[g/m^2]$ channel which indicates systematic and prominent differences between regions of the world. This systematic bias needs to be corrected in order to get a valid estimate of emissions (Liu et al. 2021).

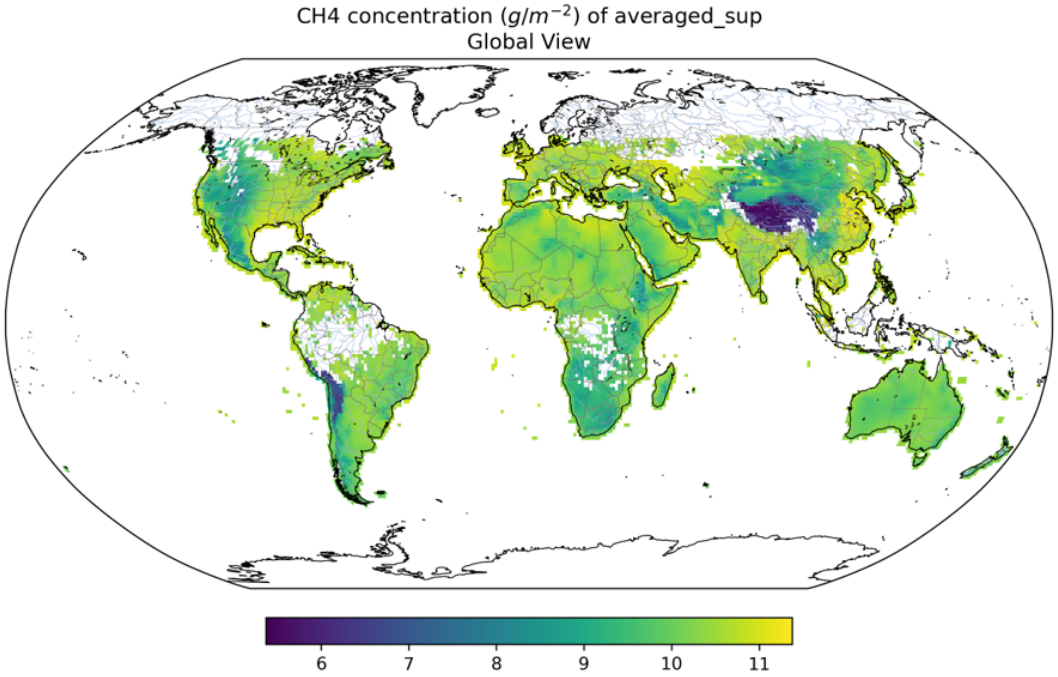

Figure 2.20: Worldwide (uncorrected) column density observations of TROPOMI for the year 2022

Removing the background component of a methane observation can be done in many ways, the simplest of which is to subtract a constant component which centres the average or median of the concentrations around zero as shown in Equation 4.5. This may be useful in other methods such as the IME to isolate the "local" trace gases from the "background" but because the divergence method only considers the change in concentration (or flux) removing a flat component does not influence the results. However, in the case of the divergence method, the background correction needs to remove the structure and variations of the methane transported from outside the domain (Liu et al. 2021) and the background correction thus needs to be applied pixel-wise. The approach taken by Liu et al. 2021 was as follows: XCH4 was destriped and albedo-corrected before the column above the planetary boundary layer (PBL) is removed based on meteorological reanalysis data from EAC4. The daily regional average is then substracted to obtain the enhancement. This however required access to prior emission estimates (EAC4) and is thus difficult to automate and apply globally.

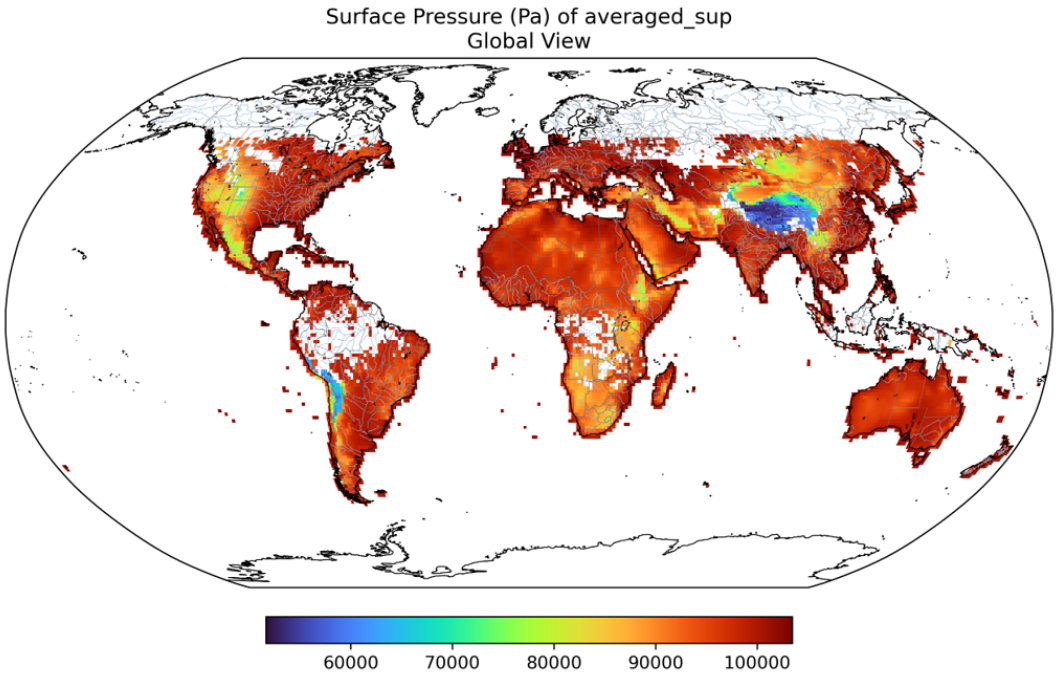

Figure 2.21: Worldwide (uncorrected) surface pressure from TROPOMI on the period for the year 2022

Pressure correction

Looking again at the column densities of Figure 2.20 and comparing it to the surface pressures, averaged over a year in Figure 2.21 one can see that the concentrations observed around high altitude areas (e.g. the Himalayan mountain ranges) are notably lower than more flat and low regions (e.g. Australia).

Veefkind et al. 2023 leveraged this fact and approximated the background contributions as a linear correlation with surface pressure as shown in Equation 2.20 by modelling the TVCD as a combination of lower tropospheric enhancement, lower tropospheric background and high stratospheric background component, the latter two can be approximated as a function of surface pressure defined through least-squares (LS) fitting of TROPOMI data over a long period and large region, which resulted in a 'pressure-corrected' column density which can be computed based on readily-available surface pressure data. The bias c_0 corresponds to the difference between the tropopause and stratospheric components of the observation and the slope c_1 describes the dependency on surface pressure of the tropospheric component. In order to make the fit applicable globally and render it less sensitive to temperature and seasonal effects the c_0 and c_1 factors are re-computed monthly for the domain of interest by taking the least-squares regression of the column-density values of each pixel with respect to the corresponding surface pressure values of those pixels (blue points in Figure 2.22). Veefkind et al. 2023 found that the fit was less sensitive to the enhanced CH4 column density values if the points were first binned (300 bins used monthly in our case) and the regression was done with the 25th percentile of Ω_{CH4} of each bin with respect to the median of the surface pressure.

$$\Omega_{corr} = \Omega - (c_0 + c_1 \cdot p_s) \tag{2.20}$$

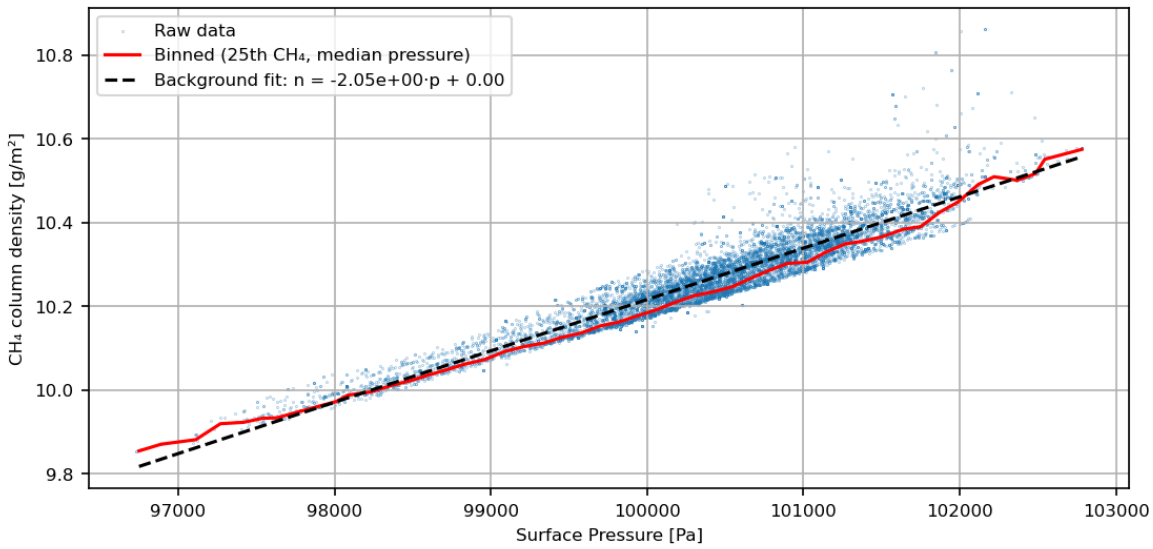

Figure 2.22: Correlation of the surface pressure and methane concentration of a TROPOMI observation, moving average over the binned 25-percentile CH4 and fitted line.

Topography correction

An alternative approach was proposed by Sun 2022 which followed-up on the observation from Liu et al. 2021 that the orography, or the influence of mountainous terrain can affect the atmospheric flow and distort the observed signal e.g. by concentrating the trace gases along a high ridge. It was thus proposed to handle the background directly on the emission map as a correction based on topography instead of a correction on the concentrations based on surface pressure.

In order to reduce the intermediate assumptions and their respective errors, the enhancements are computed directly from the observed TVCDs based on a linear regression with respect to the product algorithm laboratory (PAL) available for NO2, similarly to Veefkind et al. 2023. The wind gradient is then used instead of the flux gradient (a change in order of operation of the estimator referred to as the directional derivative method, abbreviated DD) which allows for a wind-topography term to correct for the terrain's influence (a chemical loss term is also included since this is applied to NO_x). The emissions are then obtained from the inner product of the wind and gradient of TVCD. This topography correction also required the addition of an effective surface wind field. The result is shown in Equation 2.21 and depends on the effective surface-level wind field $\bar{u_0}$, the surface altitude z_0 and a prefactor X approximating the local inverse scale height of the species of interest.

$$\tilde{E}_{corr,topo} = \tilde{E} + X\langle \Omega \bar{u_0} \cdot \nabla z_0 \rangle \tag{2.21}$$

2.4.6. Emission corrections

The rest of the corrections are also applied in the post-processing stage of the estimation and added directly on the outputted emission grid.

Lifetime correction

The first one was first described by Beirle et al. 2019 and applied on NO_x and corrects for the limited lifetime of some species: it assumed a constant rate of decay described by some reaction constant k. Using Equation 2.22 can then be used to increase the emission estimates to a level taking this decay into account. In the case of methane, which has a lifetime of about 9 years, this correction is not strictly necessary and is left as an optional addition.

$$\tilde{E}_{corr,life} = \tilde{E} + k\langle \Omega \rangle \tag{2.22}$$

Diffusion correction

Roberts et al. 2023 further developed the divergence method by introducing a turbulent diffusion correction term alongside the advective (i.e. wind) term in the fluxes' computation which results in better modelling of atmospheric behaviours and reduces local underestimations. Indeed, the standard divergence method only accounts for advective fluxes (Koene, Brunner, and Kuhlmann 2024) and assumes negligible cross-wind transport (as seen in Figure 2.23) but for high turbulence areas or high resolution observations this factor may be significant (as exemplified by Figure 2.24).

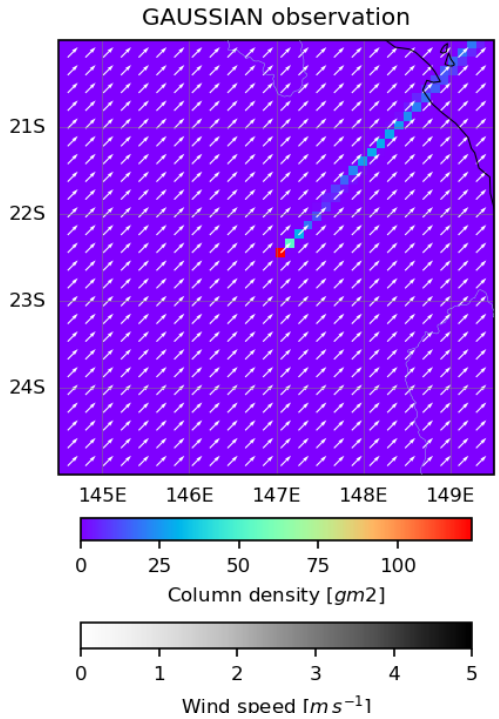

Figure 2.23: Example of a Gaussian plume observation with low diffusion (K=100)

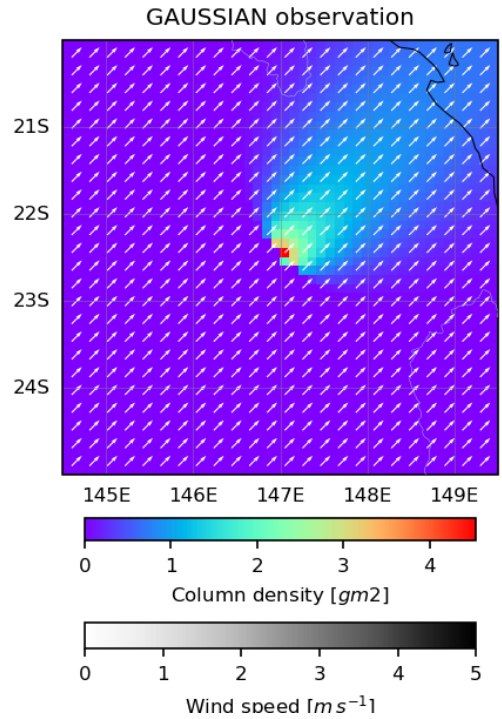

Figure 2.24: Example of a Gaussian plume observation with high diffusion (K=100,000)

Roberts et al. 2023 thus introduced diffusion term as part of the flux modelling shown in Equation 2.23 where $K[m^2 \cdot s^{-1}]$ is the molecular diffusion matrix used to approximate the spread of the plume cross-wind. Including this term into the divergence calculations was found to improve performance of point sources in particular but in order to keep our estimators and corrections separate for the sake of modularity it was decided to pull this term outside of the gradient operator and apply it separately as seen in Equation 2.24. This transformation is valid when considering the linearity of the gradient and pixel-wise multiplication operators but, as seen with the estimators' order of operation in section 4.4, this may affect performance and behaviour significantly. Furthermore, since estimating K requires prior knowledge of the field's characteristics or fitting with a known source, this correction is not applied on either the WRF-Chem or TROPOMI observations. It is however added to the Gaussian sensitivity analysis as it was seen to drastically reduce the bias of estimations, thus providing more clear comparisons between other parameters (see chapter 5)

$$E_{diff} = \nabla \cdot (\bar{F_{adv}} - \bar{F_{div}}) = \nabla \cdot (u \cdot \Omega - K \nabla \Omega) \tag{2.23}$$

$$\tilde{E}_{corr,diff} \approx \tilde{E} - \nabla(K \nabla \Omega) \tag{2.24}$$

3

Research objectives

The objective of this thesis is presented in the following chapter. The choices made here were based on the current state-of-the-art of the Divergence method presented in section 2.4 and the large variability in the implementation of the Divergence method on TROPOMI methane products as well as the resources available at SRON and their interest in this method among the other possibilities presented in section 2.3.

3.1. SRON context

The earth observation group within SRON aims to support the scientific community, policymakers, and the public by delivering information on greenhouse gases, aerosols and wildfires. The methane group among them uses the CH4 data product, based primarily on the TROPOMI instrument to "estimate methane emissions worldwide" (SRON 2025) in order to then identify and quantify so-called "super-emitters" such as landfills or fossil fuel facilities with a high potential for mitigation.

The current analysis process of CH4 in SRON is as follows: CNNs trained on manually labelled data comb through the large amount of TROPOMI observations and identify the most probable potential sources which are then confirmed on a weekly basis by scientists to avoid falsely labelling artefacts. Once a source is confirmed, the estimation of its source rate is done through other CNNs, IME method or inversions. This two-step approach handles the identification and quantification of potential sources independently whereas the divergence method has the potential to create a global gridded map of emission estimates, which are easily interpretable, at low computational cost which can help to identify sources and get an early estimate of their magnitude.

There is no requirements or specific deliverables from SRON's side that constrain this work's scope or objectives but the main goals in developing and optimising this method are to 1) have relatively low computational cost i.e. single pass estimations per observation instead of thousands of simulations for optimisation and 2) be applicable anywhere on earth without prior knowledge of emissions location and magnitude or domain-specific parameters. This last point ensures the method is not technically restricted to a specific location but cannot ensure that the results would be equally good everywhere or that it can be done at every location at once. Furthermore, the methods' foundation on physics-based estimation and worldwide applicability allows it to provide a valuable comparison point when researching new cutting-edge estimation methods such as IME or CNN without the computational cost and time investment of a CTM analysis.

3.2. Research definition

The main steps of the divergence method are summarized below and illustrated in Figure A.1, along with the various parameters associated with the contributions of method variations and corrections made in literature since. Given the wide range of implementations, corrections and application of this new divergence method (see section 2.4) a comprehensive investigation and comparison of those methodology variations and their assumed parameters can be a valuable resource for future research.

- define the spatial and temporal *domain* (centre in latitude longitude coordinates, extent in degrees, start and end dates) as well as the resolution to regrid the observations
- *filter* the observations for high-quality data points and select the ones overlapping the defined domain (a step called presampling for here on)
- co-locate a *wind field* defined by its source and effective wind height with the presampled observations
- perform any *pre-processing* steps required to the column density and flux fields
- *estimate* the emissions using the divergence operator
- perform any *post-processing* steps required to the estimated emission fields
- *integrate* the emission map over a region (defined by a shape and size) into a source rate

However, in order to constrain the scope to a reasonable amount, this investigation will be limited to TROPOMI methane observations and focus its analysis on the generation of the emission map based on available methane level-2 data products; excluding the retrieval of the methane TVCD product from the raw satellite data as well as the post-processing of the emission map via peak-fitting or other classification and identification methods into a catalog of quantified point and area sources. The implementation will be kept globally applicable, thus methodology variations requiring extensive regional tuning or simulations will be ignored in order to provide a consistent performance across the surface covered by TROPOMI.

Since no global and precise measurements of emissions exist, there is no objective ground truth that can be used to characterize the precision and accuracy of the method being evaluated. Nevertheless, the use of real-world data gives a good evaluation of the robustness and applicability of the method if the results can be compared to other studies. Synthetic observations can also be used to quantify the error in the source rate estimation in a similar way (Roberts et al. 2023, Koene, Brunner, and Kuhlmann 2024, Liu et al. 2021, Hakkarainen et al. 2022). In this case the source rate is an input into a CTM which propagates the trace gases which can be sampled and processes to look like satellite observations. This has the advantage of providing a perfect information of the source rate, wind speed and other factors which can be used to fully characterise a method's performance, strengths and downfalls.

Furthermore, the quantification of the difference and impact of each variation will be evaluated with respect to an existing synthetic dataset of WRF simulations which provide perfect information on the amount of methane present in each pixel. These synthetic test scenes can also be modified to evaluate the robustness of the method with respect to e.g. wind uncertainty, missing data or noise. Finally, a case-study of the Permian basin will be done to assess the applicability of the method on real TROPOMI CH4 data and determine whether this implementation of the divergence method is in line with other methods in use.

These restrictions allows the research objective and main research question to be defined as follows:

Research objective: *"Investigate the impact of methodology and parameter variations in the generation of an emission map via the Divergence Method based on TROPOMI methane observations."* This objective is tackled in two parts: First, this 'impact' metric is split into a few parts: The accuracy, i.e. how close the estimation is to the real emission over a certain area and the robustness i.e. how sensitive the estimation is to confounding factors such as wind uncertainty, missing data due to low quality pixels, etc. The accuracy will be evaluated quantitively by comparing emission estimations of WRF observations against the WRF source data (see RQ below) while the robustness will be investigated qualitatively through sensitivity analyses and small-scale tests.

Research question (RQ): *"Which combinations of divergence method parametrisations yields the most accurate estimates of emission for TROPOMI methane observations?"* The main research question of this thesis focuses on the accuracy of the methods on real TROPOMI data. However, since accuracy estimation can only be done for simulated data, the first four sub-questions will assess the method's performance on synthetic observations, each focusing on a specific part of the method, while the latter two will assess the applicability of the resulting divergence method on real TROPOMI observations.

Research sub-question 1 (SQ1): *"Which of the numerical gradient approximations order (4 or combination of 2+4 i.e. 'combo') yields the most accurate estimates for synthetic, background-free simulated*

TROPOMI methane observations?". In particular this will investigate the trade-off of having a more accurate and consistent fourth order gradient versus having more, lower accuracy (see subsection 2.4.3), data around artefacts and low quality pixels filled in by the second order method.

Research sub-question 2 (SQ2): *"Which of the estimators (averaged divergence, flux-averaged divergence or averaged directional derivative) yields the most accurate estimates for synthetic, background-free TROPOMI-like methane observations?"*. This part will investigate the effect of changing the order of operation around the gradient operator which, although mathematically the same, behave differently with real data containing backgrounds, artefacts and missing data (see subsection 2.4.4.

Research sub-question 3 (SQ3): *"Which of the background correction methods (pressure correction or topography correction) yields the most accurate estimates for synthetic TROPOMI-like methane observations?"* This question is important to methane in particular and will compare the applicability and accuracy of applying a pre-processing step to the methane field (pressure correction, see Figure 4.4.2) versus a post-processing step of the emission field (topography correction) in order to yield representative total emissions based on a spatially varying background.

Research sub-question 4 (SQ4): *"Which combinations of numerical gradients, estimators and background corrections parametrisations yields the most accurate estimates of time-averaged and spatially integrated emissions for simulated TROPOMI methane observations?"* Finally this will look at the possible interactions between the parameters previously investigated and assess which overall parameters should be used for case-studies using the divergence method and TROPOMI methane data.

In order to address whether this synthetic test set is representative of real TROPOMI data one of the variations will be evaluated on a case-study of the Permian basin for the year 2019 based on other studies compiled in Table 5.9.

Research sub-question 5 (SQ5): *"Are the yearly emissions, estimated through this implementation of the divergence method over the Permian basin, consistent with independent studies of the region?"* Where the independent studies are scientific publications using the divergence method and inversion method to ensure implementation and method verification. Consistency is defined here as a yearly estimation within the $Q_{est} \pm 3\sigma$ uncertainty margin of the studies considered.

Research sub-question 6 (SQ6): *"How do the yearly methane emission estimates for recent years in the Permian basin, derived in this study, compare to temporal patterns reported in previous literature?"* Although the Permian basin is a relatively well-studied region, most estimations use inversion methods which requires considerable effort and time resulting in very few analyses published for years after 2022. Varon et al. 2025 noted an increase in emissions on the 2022-2023 period, contrasting with the previously observed downwards trends of 2018-2022 (Varon et al. 2023), but no other estimations have been conducted yet to confirm this trend. This sub-question thus aims at investigating the yearly emissions of 2022-2024 in order to determine the trends of recent years and whether the hypothesised increase continues in 2024.

3.3. Scope and research activities

In order to answer these questions and achieve the research objective, this thesis is structured around three key research activities: verification, impact assessment and application.

Verification will involve testing and ensuring the validity and robustness of the existing codebase and newly implemented variations. This will include block and function-level tests to evaluate individual components of the Divergence Method, unit-level testing of the new variations (e.g., changes to algorithmic parameters), and system-level tests using idealized Gaussian plume simulations to assess the method's performance under controlled conditions.

Impact assessment will focus on the implementation of the proposed variations to the Divergence Method, followed by testing using synthetic observations generated from the Weather Research and Forecasting (WRF) model. This phase will assess the accuracy (pixel-wise and spatially integrated) and robustness of different variations and corrections on the emission maps and quantify the effects of these changes.

Application of the resulting method will be by evaluating a well-studied region using real TROPOMI

CH4 data: an evaluation of yearly methane emissions in the Permian Basin will thus be conducted on the 2018-2024 time period. The results obtained from this optimised implementation of the divergence method on the years 2018-2022 will give insights into the real-world applicability, performance and accuracy of the current codebase by comparing these to previous studies which have employed divergence, inversion, and inventory-based methods to estimate methane emissions. The results obtained on the, less-studied, 2022-2024 period will give new insights into the trends of methane emissions of the region.

4

Data and Methods

This chapter will focus on the methods used in this study. Some general points about testing approach (section 4.1) and codebase architecture (section 4.2) will be pointed out before describing the steps taken chronologically: starting with the datasets used and input formatting used in section 4.3, followed by a description of the implementation of the estimators themselves in section 4.4. Finally the evaluations of the outputs through integration and comparison of estimates leading to the results and statistics are described in section 4.5.

4.1. Testing approach

Evaluation of remote-sensing emission estimation algorithms is a critical step in characterising the accuracy and robustness of the information inferred from satellite data and is rendered difficult by the lack of an objective ground truth or control test to compare new methods against. The objective is instead to simplify the test conditions at the start and gradually reintroduce complexity, beginning with idealized Gaussian plumes (described in subsection 4.3.2), progressing to simulated observations of multi-pixel point-source emission fields using a chemical transport model (WRF-CTM in subsection 4.3.3), and ultimately applying the method to real TROPOMI CH4 observations (see subsection 4.3.1). This progression enables controlled examination of individual effects and builds confidence in the method's applicability under realistic conditions.

The verification steps are first taken at the implementation stage in which the methane observations and other support variables are compared to similar datasets and literature results using the same sort of observations. Once an end-to-end pipeline has been built, the code verification starts by using synthetic Gaussian plume scenarios investigated in section 5.1. These idealized test cases allow for visual inspection and comparison of the estimated emission map with the inputted (single-pixel) point source. Because of their simplicity, Gaussian plumes make it possible to isolate and study specific artifacts, distortions or unexpected behaviours that may arise in the implementation. The verification criteria in this phase include ensuring that all method variations return estimates close to the known source rate and that the impact of background signals, data gaps, and noise behaves as expected. While this phase does not allow for conclusions about the relative performance of different method configurations with respect to TROPOMI methane observations, it is critical for confirming that the methods are implemented correctly and behave consistently.

The verification then moves on to using synthetic CH4 fields generated by the WRF-Chem CTM model, which includes known, spatially distributed (i.e. multi-point), emission patterns. This setup better represents real-world complexities such as non-uniform wind fields, surface altitude and pressure. The use of WRF-CTM data serves as a transition between the simplified Gaussian point sources and the real TROPOMI observations the method will ultimately be used on. The distributed nature of the observation also allow for statistical and spatial comparison of the estimations with respect to the ground-truth, something which cannot be achieved with simulated point source emitters, along with the derivation of certain statistics which can be used to assess each methods' performance.

The study will then move on to the method optimisation phase in which the focus shifts to answering key research questions using the WRF-CTM dataset in section 5.2. The testing is structured around the four sub-questions defined in section 3.2. First, end-to-end divergence evaluations are conducted on one year of observations excluding the background tracer (i.e. enhancement only) for three sets of gradient order 2, 4 and their combination (2+4) while all other parameters remain the same to evaluate the effects of gradient approximation schemes (SQ1, subsection 5.2.3). A similar test set is run for the order of operations of the estimator using the divergence-averaged (E1), flux-averaged divergence (E2) and directional directive (DD) to answer (SQ2, subsection 5.2.4). Next, the background tracer is introduced to investigate the effect of background corrections in which the pressure-based and topography-based corrections are compared to an evaluation without any corrections (SQ3, subsection 5.2.5). Finally, all method components are evaluated together under the most realistic conditions (SQ4, subsection 5.2.6) to determine whether the best-performing options from earlier stages also perform well in combination. This phase also examines whether any interactions between parameters result in unexpectedly strong or weak performance (e.g. the DD estimator working better with the topography correction than the E2 method as seen in Sun 2022), ultimately guiding the selection of an optimal configuration.

The final stage is a real-world case study over the Permian Basin in the southern United States, one of the world's largest methane-emitting regions. Using the optimal method configuration derived from the previous phases, this divergence method will be applied to estimate yearly emission estimates from TROPOMI data for the 2018–2024 period (section 5.3). The results will be compared with existing literature over the same geographical region and time period, including estimates derived from inverse modelling, bottom-up inventories, and other divergence-based studies. While this does not constitute formal validation, matching patterns and emission trends strengthens confidence in the method's reliability. Furthermore, the analysis will extend to the 2022–2024 period, which has received limited attention in prior studies so far with the aim of providing initial estimates for those periods and delivering new insights for ongoing monitoring efforts.

4.2. Codebase architecture

The codebase developed for this study is based on the implementation of the method described in Veefkind et al. 2023 by Candice Chen, Msc student at SRON in 2023. It was restructured in a modular architecture designed to support flexible testing of every valid combination of the method variations mentioned in section 2.4. This function-based approach also allowed for easy reproducibility and clear verification of each method component. The workflow is divided into three main functional blocks: input handling, emission estimation, and spatial-temporal integration. Each block plays a specific role in enabling the evaluation of various divergence method configurations across synthetic and real datasets.

The input block is responsible for preparing data from readily available data sources into a uniform, analysis-ready format. This includes pre-sampling procedures such as filtering incomplete data, filling missing values, and regridding input fields to a consistent spatial resolution. This standardization ensures that all estimators operate on homogeneous input data, which is necessary for averaging the fluxes or emission maps in a similar way across all test cases. This block also accommodates data from diverse sources, including TROPOMI observations, WRF outputs, and synthetic Gaussian plumes and strives to minimize source-specific operations in order to reduce the risk of untested branches or silently skipped operations such that verification on one source set is also applicable on the others.

The estimation block constitutes the core of the divergence-based methodology and is subdivided into three main stages as shown in Figure A.1. First, the pre-processing stage applies corrections to the concentration fields and computes the flux which is optionally averaged before the next stage. Second, the estimation stage performs the actual emission inference. This is the defining step of the divergence method, converting methane flux fields into emission estimates. Several estimator variations from literature are implemented including E1, E2, and DD formulations. Finally, the post-processing stage applies optional corrections directly to the emission grids such as lifetime, diffusion or topography corrections.

The final integration block aggregates the emission estimates over a defined time period and spatial domain, which are then integrated into a total source estimate. When applied to synthetic benchmarks, this block also includes the pixel-wise comparisons between inferred and true emissions and computes

the statistical metrics used to assess method performance.

The codebase follows a function-based architecture with control-model-view design. Each module is self-contained, focusing on a specific task within the pipeline. The implementation adheres to PEP-8 style guidelines and emphasizes modularity and reusability in order to adapt it dynamically to each variation of the divergence method used in literature. Collaborative development practices were applied to ensure clarity and extensibility, allowing future researchers to adapt or extend the framework for related applications in emission monitoring. A graphical representation of the workflow is shown in Appendix B.

4.3. Inputs and data

This section describes the dataset chosen as inputs to the divergence method and the formatting steps taken. The main methane product is taken from one of three sources: subsection 4.3.1 goes into the TROPOMI level-2 (lv2) methane product and associated support variables, subsection 4.3.2 details the generation of the idealised Gaussian plume model and their integration as a TROPOMI-like dataset and subsection 4.3.3 describes the outputs of the WRF-Chem simulations and the subset used for performance evaluation in particular. Some attention is then devoted to the wind products in subsection 4.3.4 and the regridding step that ensures a regular lat-lon grid is fed into the next phase in subsection 4.3.5.

4.3.1. TROPOMI level-2 methane product

The TROPOMII Level 2 (lv2) product consist of a multitude of data channels described in detail in Apituley et al. 2022. The main input to this study is the column-averaged dry air mole fraction of methane $XCH4[ppbv]$ which indicates the estimated average methane concentration within each pixel's air column in particles per billion per volume (ppbv). Other channels such as the aerosol optical thickness (AROP), cloud fraction (CF), surface albedo in the SWIR band (ALSW) and the quality assurance value (QA), which is a summary indicator of each retrieval's confidence, are used. Additionally, the surface pressure channel ($P_s[hPa]$) of the lv2 reprocessed TROPOMI methane product is included in this dataset to be used in the pressure-correction (see Figure 4.4.2).

The first step is to presample the large TROPOMI dataset into a subset relevant for the analysis at hand. That is, look through the files of all days within the period of interest and cropping out the pixels whose latitude and longitude fall between the domain limits (a margin is included to ensure all locations in the domain contain pixels at the edges). This step also removes any data products not specifically required for the divergence method in order to minimise the data size of the presampled set. Valid pixels are then filtered in order to keep only the datapoints with high confidence. Filtering is done by keeping pixels with high quality-assurance values, typically around $qa > 70 - 75\%$, low cloud fractions $CF < 30\%$ and constraining the solar zenith angle (SZA) to reduce pixel area differences throughout an image $SZA < 65°$ (see the settings used by previous divergence papers under "TROPOMI filter" in Table A.1). Latitude, longitude and time ranges can also be constrained to provide more consistent data (Beirle et al. 2019, Beirle et al. 2021, Beirle et al. 2023 and De Foy and Schauer 2022). In the case of this implementation of the divergence method we used $qa >= 0.75$ similarly to the study of a Louisiana blowout using TROPOMI methane observations in 2021 Maasakkers et al. 2021. This simple criteria is a good summary of overall quality, easy to replicate and applicable globally. More complex filtering schemes can be readily applied in future studies as all the variables discussed above are included in the presampled dataset.

Finally the observations' units need to be changed from the concentrations in $ppbv$ given in the retrieval to column-densities of $\Omega[g/m^2]$ as required by the divergence method (see Figure 2.11). This is done following Equation 4.1 as per Veefkind et al. 2023 which requires the molar mass of methane $M_{CH4} = 16.03 \cdot 10^{-3}[kg/mol]$ and the average molar mass of air $M_{air} = 28.964 \cdot 10^{-3}[kg/mol]$ as well as the gravitational constant $g_0 = 9.80665[m/s^2]$ and the dry surface pressure. The pressure value used is the per-pixel surface pressure channel from the TROPOMI product when using TROPOMI or WRF concentration fields and the sea-level atmospheric pressure $p_s = 101325[Pa]$ from the international standard atmosphere (ISA) when using Gaussian plumes.

$$\Omega = X_{CH4} \cdot 10^{-6} \cdot \frac{M_{CH4}}{M_{air}} \cdot \frac{p_s}{g_0} \tag{4.1}$$

This is verified by comparing the same location as Maasakkers et al. 2021 at the same date and using the same filtering option of $QA >= 0.75$ resulting in the presence of the characteristic plume in both the original (Figure 4.1) and our implementation (Figure 4.2). Furthermore, we can observe that approximately the same region is masked out in both cases. The difference is due to the resampling of Figure 4.2 onto a regular grid as explained in subsection 4.3.5.

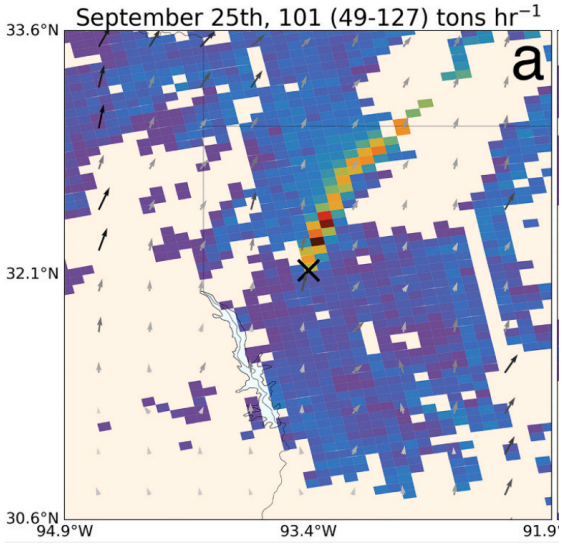

Figure 4.1: TROPOMI methane observation from Maasakkers et al. 2021

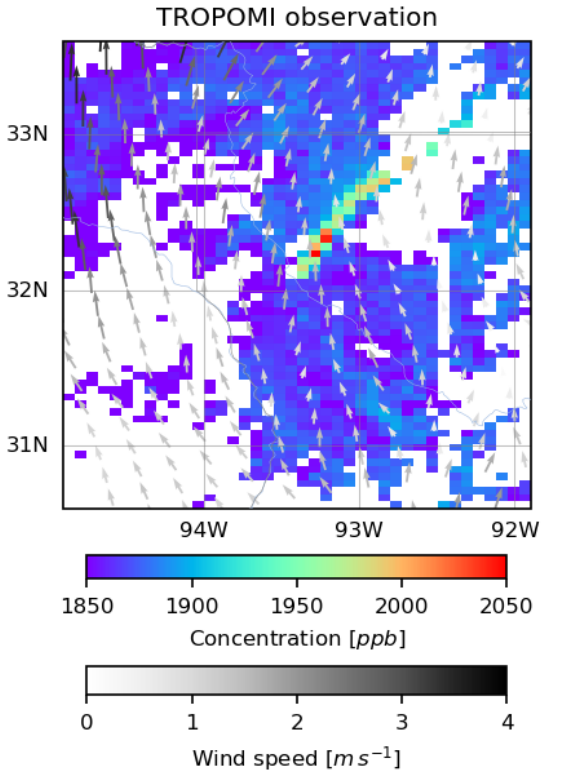

Figure 4.2: Concentrations on the same location and date as Figure 4.1 pre-processed and filtered using the divergence method pipeline developed in this study, overlayed with the GEOS-FP 10m winds at the time of measurement (rounded to the nearest hour).

4.3.2. Synthetic Gaussian plumes

The simplest testing set used in this work (see section 4.1) is the ideal Gaussian plume:

the 3D solution to a point source of strength $Q[kg \cdot s^{-1}]$ located at some height, assumed constant here, $H = 10[m]$ whose contents are transported via advection along a uniform wind field of speed $w[m/s]$ and diffusing in the cross-wind direction based on its constant of turbulent diffusion $K[m^2 \cdot s^{-1}]$ (Stockie 2011). Such a concentration field is shown in Figure 4.3 and described for each position in a Cartesian volume (x,y,z) per Equation 4.2 assuming the wind field is aligned with the x-axis.

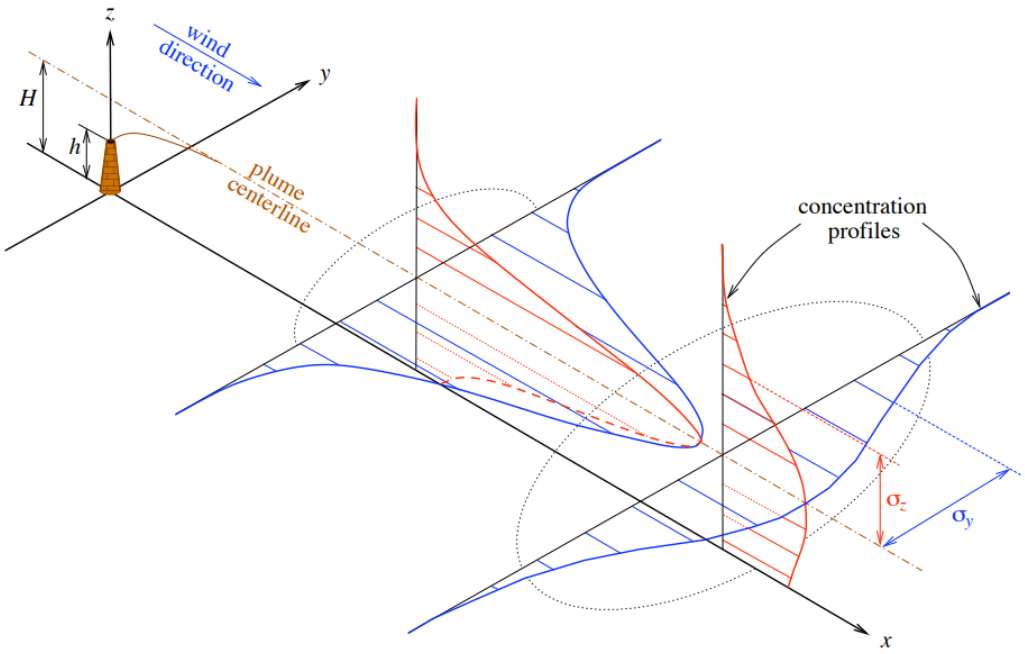

Figure 4.3: visualization of a Gaussian air pollutant dispersion plume from Stockie 2011

$$C(x,y,z) = \frac{Q}{4\pi K x} \cdot exp\left(-\frac{y^2 w}{4Kx}\right) \cdot \left[exp\left(-\frac{(z-H)^2 w}{4Kx}\right) + exp\left(-\frac{(z+H)^2 w}{4Kx}\right)\right] [kg/m^3] \quad (4.2)$$

Integrating this solution along the z-axis results in a satellite-like observation where whole column is seen at once and the concentrations are given in units of $[kg/m^2]$ as required by the divergence method (similarly to subsection 4.3.1). Relaxing the assumption that the wind blows in the x-direction (as in Equation 4.2) and letting it be defined by some angle θ yields Equation 4.3 (Stockie 2011).

$$C(x,y,\theta) = \frac{Q}{2\sqrt{\pi w K (xcos(\theta) + ysin(\theta)}} exp\left[-\frac{((ycos(\theta) - xsin(\theta))^2}{4K\left((xcos(\theta) + ysin(\theta)\right)}\right] [kg/m^2] \quad (4.3)$$

Since the x- and y- values in Equation 4.3 are in distance units (m) the first step in making this synthetic set of observations is to transform the latitude-longitude domain in units (deg) into an eastings-northings grid (m). Equation 4.3 can then be applied for a set of parameters $C(x,y) = f(Q,K,w,\theta_i)$ where the angle of each observation i is defined as $\theta_i = \theta_0 + \Delta\theta$. The resulting concentration grid is then regridded to the original latitude-longitude grid and normalised for pixel-area in order to conserve total mass across the observation. Optionally, some amount of pixels can be randomly masked out (missing data %) and a simple background B can be added with a constant (B_0) and noise (σ_B) component following $B = B_0 \pm \sigma_B$.

Support variables such as surface pressure, surface altitude, ALSW and AROP are then added as constant grids of ones in the same format as the TROPOMI grid - this simplification is done as the concentration grid is idealised and independent from all of these support variables but also means any investigation using these cannot be conducted with the Gaussian plumes.

4.3.3. Simulated WRF emitters

The more rigorous synthetic observations required to properly verify, characterise and optimise the divergence method uses concentration fields obtained from the Weather Research and Forecasting (WRF) model, coupled with Chemistry (WRF-chem). The simulation is conducted on a coarse ”outer”

domain using ERA-5 as its meteorological boundary conditions and an ”inner” domain with finer resolution as well as scheme-2 for its planetary boundary layer (PBL) definition. The emitters are defined as 2D surface grids and differentiated by their tracer number. These tracers are then propagated through the simulated wind field independently and sampled 24 times per day as 3D concentration fields on the WRF grids.

In particular the simulations used were initially conducted for an inversion study similar to (Guanter et al. 2024) but unpublished as of yet. The set of simulations used were that of a Russian mine (abbreviated as the RUS domain) which spanned the period from 2022/01/01 to 2022/01/31 with the inner domain cropped to 52.172-57.172 deg latitude, 81.122-86.122 degree longitude (highlighted in Figure 4.4).

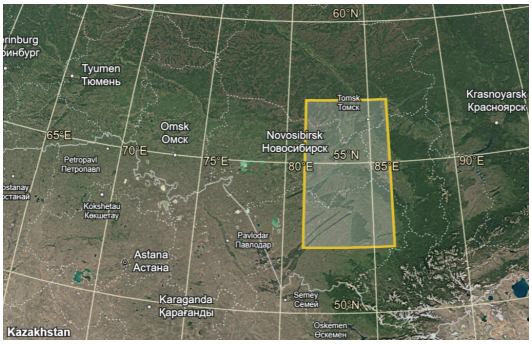

Figure 4.4: Latitude-Longitude domain of the WRF-RUS region of interest

These contains a series of multi-pixel diffuse or point sources (Figure 4.6), single-pixel point sources (Figure 4.7) and a background tracer (Figure 4.5) which does not emit within the inner domain but transports methane from outside the domain into the scene of interest. The strength of each tracer, integrated along the z-axis, for the outer and inner domain of hours 0-12 and 12-24 is constant. Since these are independent their resulting concentrations can be summed up linearly to include the background, or not, to the tracer of interest.

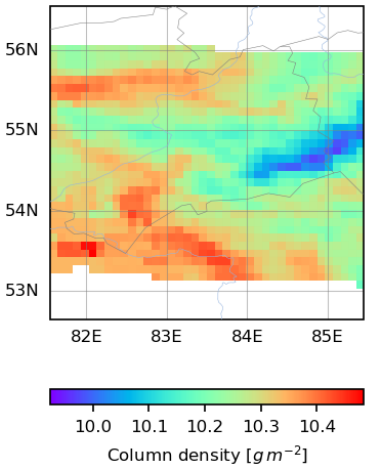

Figure 4.5: Concentration field of the background WRF tracer (#1) for RUS 2022/01/01 to 2023/12/31.

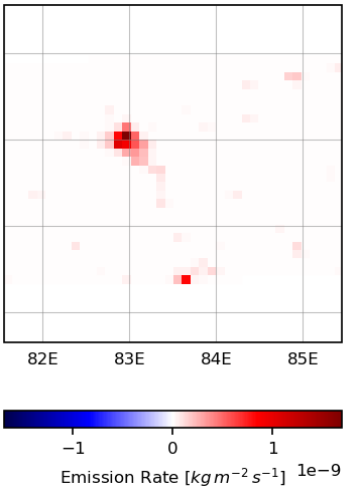

Figure 4.6: Emission strength of a multi-pixel point source WRF tracer (#3) for RUS 2022/01/01 to 2023/12/31.

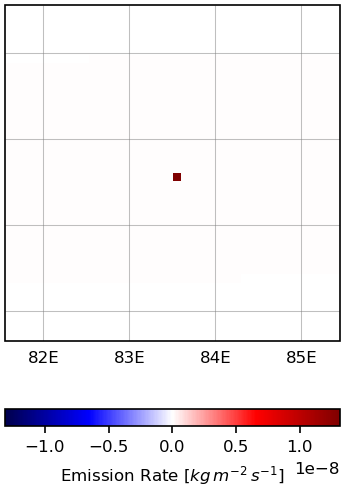

Figure 4.7: Emission strength of a single-pixel point source WRF tracer (#20) for RUS 2022/01/01 to 2023/12/31.

Since the objective of the divergence method evaluated here is to estimate sources averaged over long time periods (on the order of months-years), the tracers chosen were the background along with multi-pixel point source which is steady throughout the day, constant over the year 2022 and whose spatial distribution includes a main source spread out in the centre of the domain. The emitters' strength are initially for the inversion they were meant for and thus need to be rescaled for our purposes: this is done by taking the emission grid used to drive the simulation, formatted similarly to the concentration grids of the outputs, and integrating the emission over the target domain (see subsection 4.5.1 for details on method) to find the total emissions of each tracer $Q_{ref,init}[ton/h]$. Each grid is then multiplied by a prefactor $Q_{param}/Q_{ref,init}$ such that their resulting total emissions is $Q_{param}[ton/h]$.

Although most support variables necessary are present in the WRF-Chem dataset, the altitude is no-

tably absent: instead of presampling the corresponding TROPOMI observation for each WRF simulation required, which would require significant memory and processing usage, it was decided to use an external digital elevation model (DEM) instead. The NOAA ETOPO global relief model (NOAA 2025a) was resampled to the regular lat-lon grid globally, bound to a minimum altitude of $H = 0$ and saved as a separate local file (*ETOPO1_Bed_g_gmt4*). This could then be quickly presampled to the correct location (see Figure 4.8) and resampled as an additional channel on the final TROPOMI-like grid (see Figure 4.9, note the slight angle due to the satellite's orbital inclination in the overpass)

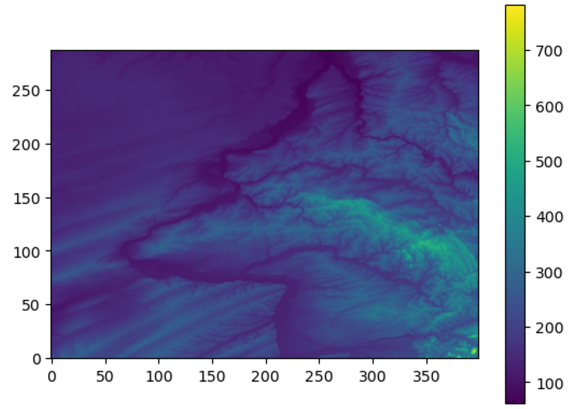

Figure 4.8: DEM presampled to the domain of interest

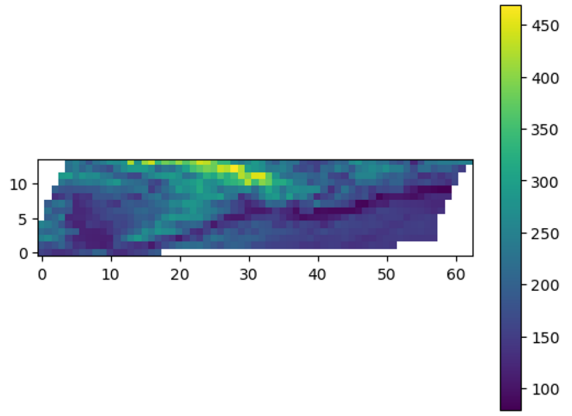

Figure 4.9: DEM presampled and regridded to the TROPOMI grid

The WRF-Chem outputs used are pre-processed to be co-located with TROPOMI observations and thus include the same scanline and groundpixel along with most of the support variables which ensures the distribution of missing data across the domain is representative. However, the format of the output files is vastly different from the TROPOMI observations, being presented a a 1D vector of length N_{obs} which needs to be reshaped to a 2D lat-lon grid onto which the TROPOMI coordinates and variables are added. Furthermore, it should be noted that the WRF-Chem simulations contains three different altitude averaging schemes: unweighted average (no_ak), using an averaging kernel (by default) and using a pressure-weighted scheme (_pw). In all cases discussed here the default scheme is used.

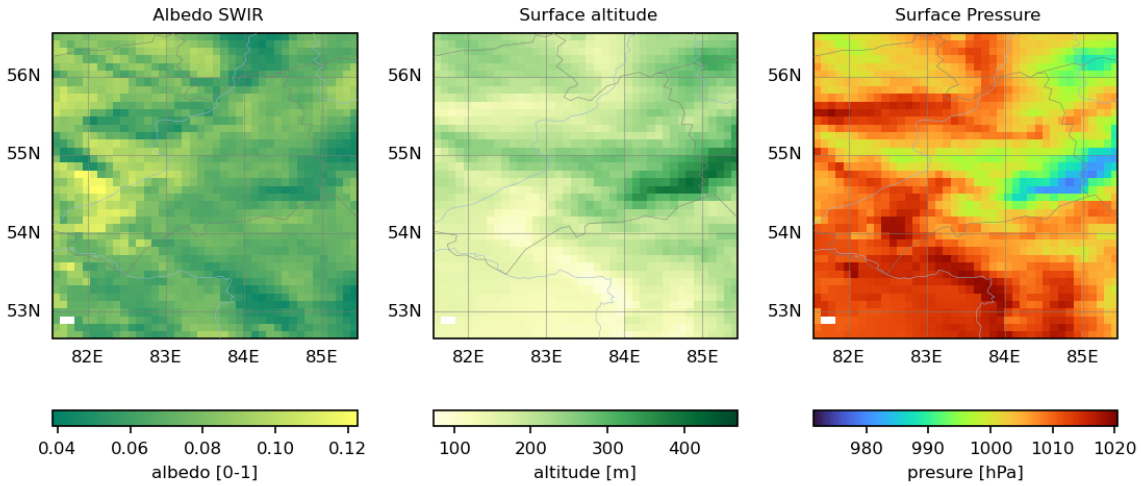

Figure 4.10: Support variables obtained via the TROPOMI input pipeline

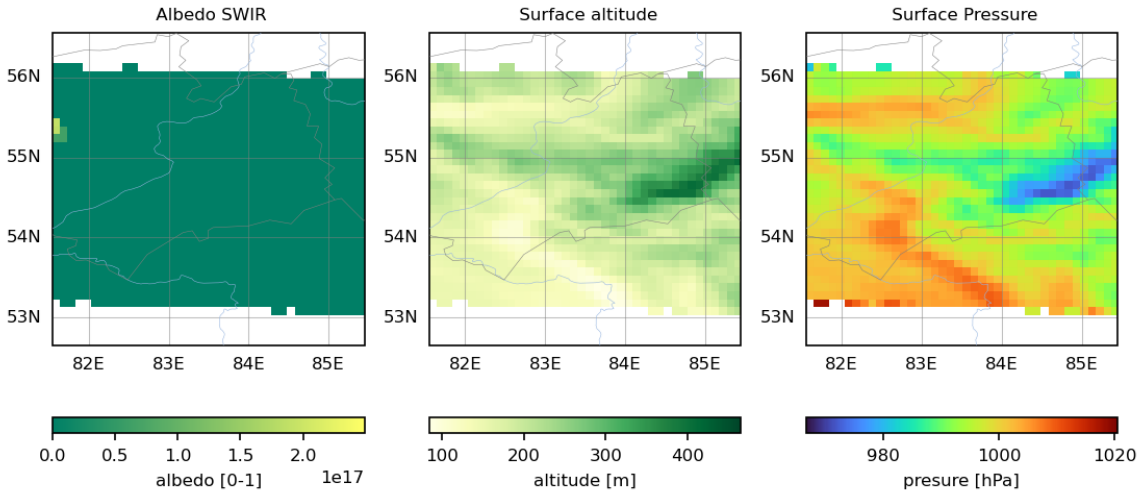

Figure 4.11: Support variables obtained via the WRF input pipeline

The support variables were verified by inspection by comparing and plotting the final grids using TROPOMI as a data-source (Figure 4.10) and doing the same steps, domain and days using WRF as a data-source (Figure 4.11). Since the SWIR albedo was not used in this method it was not added to the WRF set, both the surface altitude and pressure have similar magnitudes and spatial distributions, though not exactly the same. In this case the missing top part of the image can be explained by the fact the domain presampled is situated at the top edge of the domain, this also causes the scale to shift but the magnitudes are the same ($\pm 0.5m$ or $\pm 100Pa$ likely due to resampling approximations in the last regridding step, see Figure 4.17).

4.3.4. Wind field

Wind fields play a critical role in the estimation of trace-gas emissions from satellite observations, as they directly influence the transport of trace gases in the atmosphere and their estimation is itself a remote-sensing problem with uncertainties. This work uses both the fifth generation ECMWF reanalysis (ERA-5) dataset (ECMWF 2025) provided by Copernicus and the GEOS forward-processing (FP, near real-time) data product (modelling and (GMAO) 2025) by NASA's global modelling and assimilation office (GMAO). Two independent datasets are used in order to evaluate the impact of wind uncertainty on emission estimations. In particular, the WRF-Chem model used GEOS-50 and thus the GEOS-FP dataset can be considered a "true wind" field and the difference observed by using ERA-5 instead should be indicative of the difference between real wind and either ERA-5 or GEOS-FP.

Additionally, the vertical altitude of the gas layer not only affects atmospheric transport but also the satellite retrieval process itself, as highlighted by Veefkind et al. 2023. This effect can be mitigated by choosing the correct wind altitude level corresponding to true mean altitude of the methane plume. However, since that altitude is not known, studies vary significantly in the wind altitude level they use (see Table A.1) which leads to substantial differences in the resulting emission estimates.

The chosen wind source dataset is first presampled to the target domain at the hour nearest to the observation time and at the effective wind altitude chosen (either 10, 50 or 100 $[m]$). The presampled field is then interpolated using a bi-linear scheme to the TROPOMI grid. When using a regular lat-lon grid the wind vectors need to be rotated by the average inclination of the observation (around $i = 15^o$) in order to keep the field aligned with respect to the ground. Additionally, a copy of the wind field is rotated a further 45 degrees in order to compute the diagonal flux gradient (see Figure 2.19).

This approach is verified for both wind fields and all altitude levels by comparing the co-located regular grids (see Figure 4.2) with an observation from Maasakkers et al. 2021 (see Figure 4.1). Both can be seen to be properly aligned with the plume direction and have similar magnitudes.

4.3.5. Resampling

The CH4 observations of TROPOMI have a spatial resolution of approximately 7 x 5.5 km directly below it (Veefkind et al. 2012) which grows wider further away from the nadir point due to the angled projection of the beam (see Figure 2.1). This results in an irregular grid in scanline-groundpixel coordinates which cannot be co-located with another orbit's observation, as is needed when averaging over a long time period (see Figure B.3). All grids are thus regridded to a regular, latitude-longitude grid of pre-defined resolution, a step also called resampling. If specifically using the divergence-averaged (E1) method then the native TROPOMI grid can be kept intact for the flux and gradient calculations and is only resampled at the end of the estimation phase (see Figure B.4). The method used is described below:

For a satellite pixel p with an area $S(p)$ and (e.g. column density) value $\Omega(p)$ associated with an uncertainty value $\sigma(p)$ the latitude-longitude grid cell i has an overlapping area $A(p,i)$ with p as shown inFigure 4.12. The new grid cell value $\bar{\Omega}(i)$ can then computed using Equation 4.4 where $N(i)$ is the number of grid cells intersected by p.
Equation 4.4

$$\bar{\Omega}(i) = \frac{\Sigma_{p=1}^{N(i)} \frac{A(p,i)}{S(p)\cdot\sigma(p)} \Omega(p)}{\Sigma_{p=1}^{N(i)} \frac{A(p,i)}{S(p)\cdot\sigma(p)}} \tag{4.4}$$

This method has the advantage of being computationally fast while it fully uses and appropriately weighs the information from all individual satellite observations with a wide range of pixel sizes and column uncertainties.

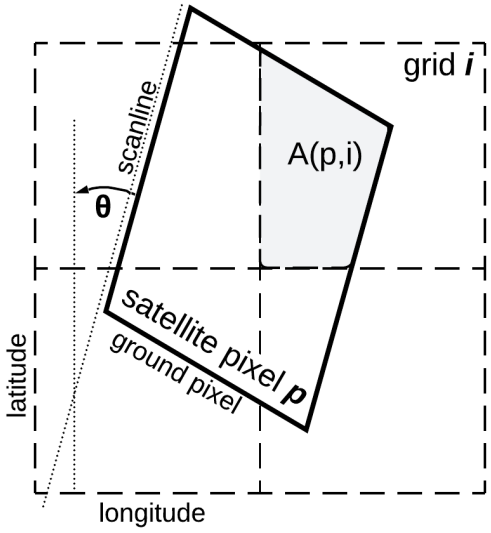

Figure 4.12: Schematic of the resampling method used to map satellite pixel values to a regular grid

This was implemented in fortran (f90) by Kai Yang as the "CAKECUT" algorithm in 1998, applied by Lei Zhu in 2015 for pixel regridding and adapted to SCIA resampling by J.D. Maasakkers in 2016.

4.4. Estimator

This section discusses the implementation, adaptation and verification steps taken to include the numerical gradient approximation (subsection 4.4.1) and corrections (subsection 4.4.2).

4.4.1. Gradient operator

The gradients of both the concentration and flux grids (either daily or averaged) are computed for order 2 and 4 in orthogonal and diagonal directions. The total gradient is then obtained, depending on the settings used, by summing the x and y components of order 2 or 4 of the chosen direction. Similarly to the direction, it is possible to combine these as seen in Veefkind et al. 2023 where the fourth order is used wherever possible (i.e. all 8 neighbours are valid) and the second order fills the gaps. This combination of gradient order is abbreviated "combo". The effect on estimation performance of the choice of gradient order will be discussed in subsection 5.2.3.

In order to retain the form of the gradient approximation seen in Equation 2.7, the pixel width and height are assumed constant throughout the gradient region. The d_{lat} and d_{lon} are first computed as the average width and height of every pixel in the scene and then converted to meters based on the average latitude (see Equation 4.10 for analogous conversion). This is a first-order approximation chosen for its low computational cost although it may result in skewed results at high latitudes, coarse resolutions or for very large domains.

4.4.2. Corrections

This section will first discuss the background-corrections required to test the Gaussian plumes' emission estimation performance in subsection 4.4.2 before delving into the verifications steps taken for

the pressure (Figure 4.4.2) and the assumptions required for the topography (Figure 4.4.2) correction. Finally, the other corrections mentioned in subsection 2.4.6 will be addressed.

Gaussian plume masking

In order to reduce observational bias in Gaussian testing it was deemed necessary to only consider the pixels outside of the plume when computing the background component. Indeed, using a background of exactly 0 leads to pixels being simplified to NAN values as part of the optimisation process which creates artefacts and does not create representative results of the ideal case studied here. This step is referred to as ”masking” and an example of which is shown in Figure 4.13: all pixels whose value is strictly higher than the average over the whole scene plus one standard deviation of the pixel values are considered as the plume $\Omega_i > \langle\Omega\rangle + 1 \cdot \sigma_\Omega$. Background corrections based on the average, median and masked average and median of the scenes are included in order to demonstrate this effect (see Figure 5.11).

$$\Omega_{corr} = \Omega - \langle\Omega\rangle \tag{4.5}$$

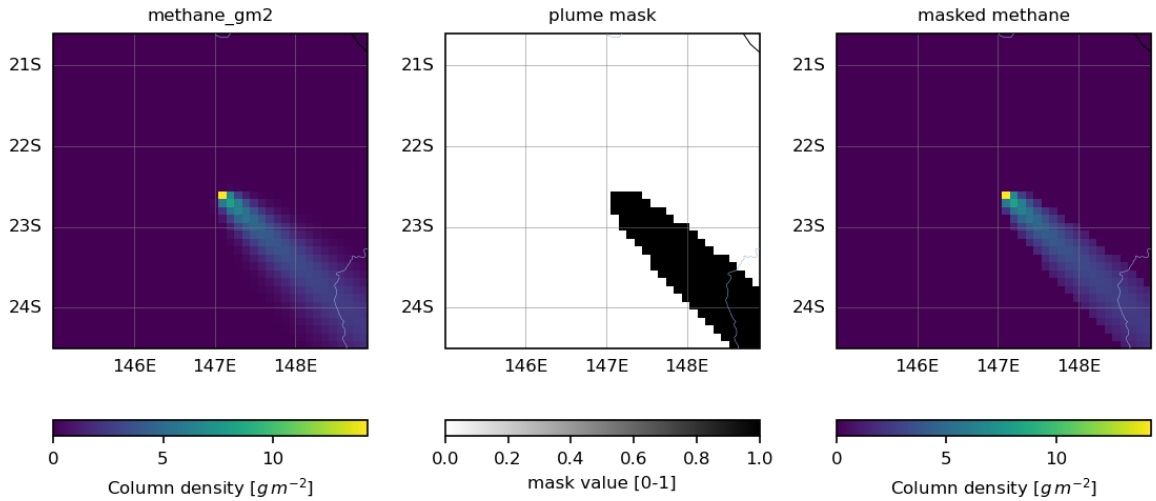

Figure 4.13: Boolean mask (middle) indicating the probable location of the positive enhancements of interest (right) based on the column densities of an ideal plume (left)

Pressure correction verification

The pressure correction implemented in our case is the binned version (see Figure 4.4.2) which was then verified by applying it on the same location and time as Veefkind et al. 2023 (the Permian region for October 6th 2020): The resulting corrected column density field (Figure 4.15) can be verified by comparing it to the one obtained by Veefkind et al. 2023 (Figure 4.16) based on the uncorrected field of that location (Figure 4.14).

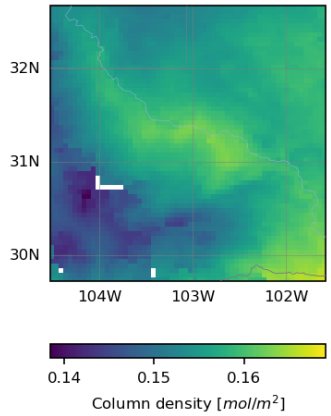

Figure 4.14: Concentration field of a TROPOMI observation

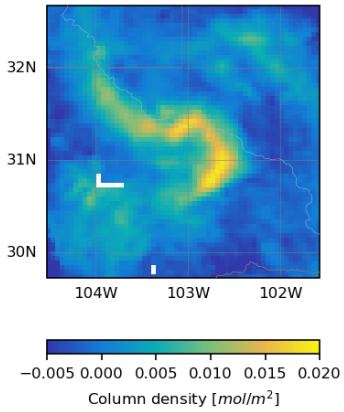

Figure 4.15: Enhancement field of the same TROPOMI observation after pressure correction as done in this study

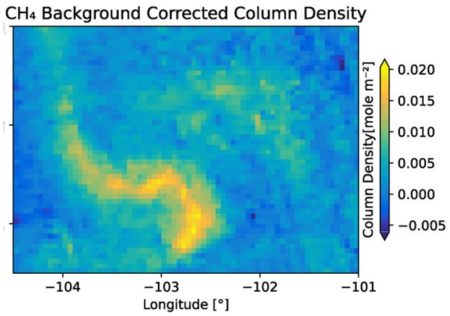

Figure 4.16: Enhancement field of the same TROPOMI observation after pressure correction as done in Veefkind et al. 2023

Both are seen to be centred around 0 mol/m^2 and show a similar spatial distribution with a quasi-null background and an enhancement in the top-right quadrant. It should be noted that since this method depends on a correlation with the data within the domain instead of a reference day and time of known quantities, the pressure correction's performance is region-dependent and will perform best if most the study area is not an emitter as this would bias the correction to obscure all sources.

Topography correction fitting

This factor X however, cannot be derived from readily available data products similarly to what was done in Figure 2.22. Sun 2022 instead fits it (β_1) using the relative abundance of methane in each level of the 3D simulations used in their study, an approach that cannot be replicated with real data where the height of the gases is not known. An alternative path was thus used in which X was computed assuming a constant inverse scale height $1/H[m^{-1}]$. The scale height of a species describes its distribution along the column's height and can approximated analytically using Equation 4.6 where k_B is the Boltzmann constant, N_A the Avogadro constant, M_X the molar mass of the species and T the characteristic temperature.

$$C_{z=0}[g/m^3] = X[1/m] \cdot \Omega[g/m^2] \text{ where } \beta_1 \approx X = 1/H \tag{4.6}$$

$$H = \frac{k_B \cdot T}{m_x \cdot g_0} = \frac{k_B \cdot N_A}{g_0} \cdot \frac{T}{M_x} \tag{4.7}$$

Most of these factors are known constants and the scale height can thus be computed for various temperatures: in our case we used $T = -50, 0, 15, 50^oC$ and tabulated the values of H for most of the species considered in the divergence method in Table 4.1. X was then taken to be $1/H$ for an assumed temperature of $T = 15^oC$ (standard sea-level ISA atmosphere model) as a baseline. Other values of X based on the other temperatures are used in sensitivity analysis seen in Figure 5.11. This approach is of course expected to be less reliable and more subject to local variations than the one used in Sun 2022 but has the advantage of being applicable anywhere without requiring extensive simulations that essentially perform an inverse analysis on the concentration fields.

Table 4.1: Computed scale height factors based on species molar mass and assumed temperature.

		H [m] computed				
T [C]	M [g/mol]	*-50*	*0*	*15*	*50*	X [1/Km]
T [K]		*223.15*	*273.15*	*288.15*	*323.15*	
NO	30	6303.4	7715.77	8139.48	9128.14	0.01229
NO2	46	4110.91	5032.02	5308.35	5953.13	0.01884
NO3	62	3050.03	3733.44	3938.46	4416.84	0.02539
CH4	**16**	11818.9	14467.1	**15261.5**	17115.3	**0.00584**
CO	28	6753.64	8266.89	8720.87	9780.14	0.01022
CO2	44	4297.77	5260.75	5549.64	6223.73	0.01802

Other corrections

$$\Omega_{corr} = \Omega + \alpha_0 + \alpha_1 \cdot a + \alpha_2^2 a \tag{4.8}$$

Finally, other correction used in literature (see Appendix A) such as the polynomial bias correction for e.g. albedo (Equation 4.8) or destriping steps are already included in the methane product used and thus not repeated in this phase.

4.5. Evaluation of emissions

This section will describe the last phase of the divergence method: the steps taken to spatially integrate the emission map over a region in order to retrieve the total emissions in subsection 4.5.1 and will describe the objectives functions and metrics used to assess the performance of each method when comparing it to a known ground-truth in subsection 4.5.2 and subsection 4.5.3 before discussing the way in which uncertainties are estimated in subsection 4.5.4.

4.5.1. Emission integration

Since the emission field outputted after the estimator (and optionally corrected) has units of $kg \cdot m^{-2} \cdot s^{-1}$, an spatial integration step is required to obtain a source rate in kg/s. This is done by first multiplying each grid value by their respective area $A_i[m^2]$ and then summing all pixel values $q_i[kg/s]$ within the domain as per Equation 4.9.

$$Q_{est} = \Sigma_{i=1}^{N} \tilde{E}_i \cdot A_i \tag{4.9}$$

Practically, this sum is done by masking out the domain and adding every pixel whose centre lies within the defined shape (circle / square of a predetermined size or otherwise defined geographical region). A more accurate approach would be to do a weighted sum based on the proportion of each pixel in or out of the domain (similarly to Equation 4.4) but since the vast majority of pixels are either in or out and the computational cost is not negligible it was decided to simplify it to a boolean case.

To convert the pixel coordinates on the latitude-longitude in degrees to square meters, it is necessary to account for the Earth's curvature using the haversine function which provides a geodesic distance in meters based on two coordinates in lat-lon space. Since lines of longitude are evenly spaced, the height of the pixel is computed using the distance between the two left-side corners. The width, however, varies with latitude due to the convergence of meridians toward the poles: to approximate this, we first compute the midpoint latitude between two leftmost corners and then use the haversine distance along that horizontal midline between the left and right sides of the pixel.

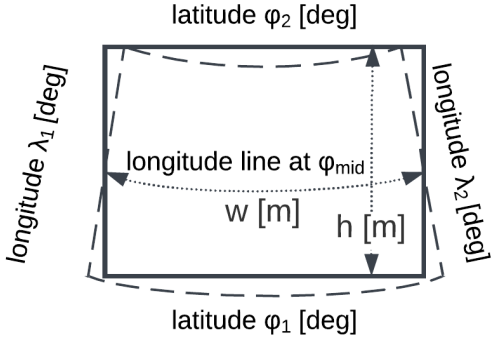

Figure 4.17: Schematic of the pixel area calculation based on latitude and longitude corner values.

This is expressed in full by Equation 4.10. This method introduces small geometric errors which mostly cancel out when considering the entire pixel (illustrated in Figure 4.17). It should be noted that pixels at higher latitudes may slightly overestimate or underestimate the actual area but this approximation remains valid for the purposes of this study, particularly since other assumptions (e.g., wind field uniformity, plume altitude) typically introduce larger errors.

$$A_i \approx w_{(\varphi_{mid})} \cdot h_{(\lambda 1)} = hav\left[(\lambda_1, \frac{\phi_1+\phi_2}{2}); (\lambda_2, \frac{\phi_1+\phi_2}{2})\right] \cdot hav\left[(\lambda_1, \phi_1); (\lambda_1, \phi_2)\right] \tag{4.10}$$

Performing these integration steps on the emission estimation grid yields the total estimated source rate $Q_{est}[kg/s]$ but can also be applied to the reference emission grid (EMIS files of the WRF simulations in our case) and yield the total reference source rate $Q_{ref}[kg/s]$ over the same domain. Since the same function is used for both, any errors in geometric misalignments over the domain boundary or pixel area errors will be the same in both Q_{ref} and Q_{est} thus giving a good idea of the performance of the divergence itself.

4.5.2. Objective functions and testing methods

The first step in finding a good metric to assess our estimation performance is to identify which outputs are going to be evaluated and how they can be tested: the location and extent (or boundaries) of sources can be evaluated by metrics such as peak area fraction (De Foy and Schauer 2022), classification into types such as point (PS), area (AS), urban or multipoint sources (De Foy and Schauer 2022 and Beirle et al. 2021) Additionally, locations can be verified by matching identified sources with known cities or power plants from bottom-up inventories (Beirle et al. 2023), (Veefkind et al. 2023) or simulated transport of an assumed emission rate (Liu et al. 2021). Alternatively, the source rate (quantity of methane emitted in ton/h) can be quantified and compared to the ground truth. This can be done by evaluating the total source rate error over a specific domain and comparing it to the summed-up source rates of the same domain (see Equation 4.11) where E is based on simulation results or other papers' estimates (De Foy and Schauer 2022, Sun 2022, Liu et al. 2020) if it is a well-studied area. This second metric is used for the simulated observations since we only deal with static, steady sources.

$$\Delta Q = Q_{est} - Q_{ref} \tag{4.11}$$

This can be extended to a correlation of estimated measurements with the true emission estimates over a range of source rates (Beirle et al. 2019) which can be obtained by repeated comparison of total emissions over a range of times, locations or simulated source rates. However, a similar evaluation can be achieved by considering each pixel i of the emission map as an independent source E_i in which case a single domain and time is sufficient to gather information on the detection limit and uncertainty of the estimation (see Equation 4.12)

$$\Delta q_i = q_{i,est} - q_{i,ref} \tag{4.12}$$

4.5.3. Grid comparison

One way to visualise Equation 4.12 is to plot each pixel as a single data point where the x-axis value corresponds to the emissions on the reference grid and the y-axis value corresponds to the estimated emissions on the divergence grid (Figure 4.18, left). In the case of a perfect estimation, all points would lie on the 1:1 line (highlighted in black). However, since the WRF files are pre-processed to match TROPOMI observations and the emission fields are given on a regular lat-lon grid for averaging purposed, it is necessary to repeat the formatting regridding steps from subsection 4.3.3 and subsection 4.3.5 to the emissions files (abbreviated EMIS) in order to match each pixel one-to-one.

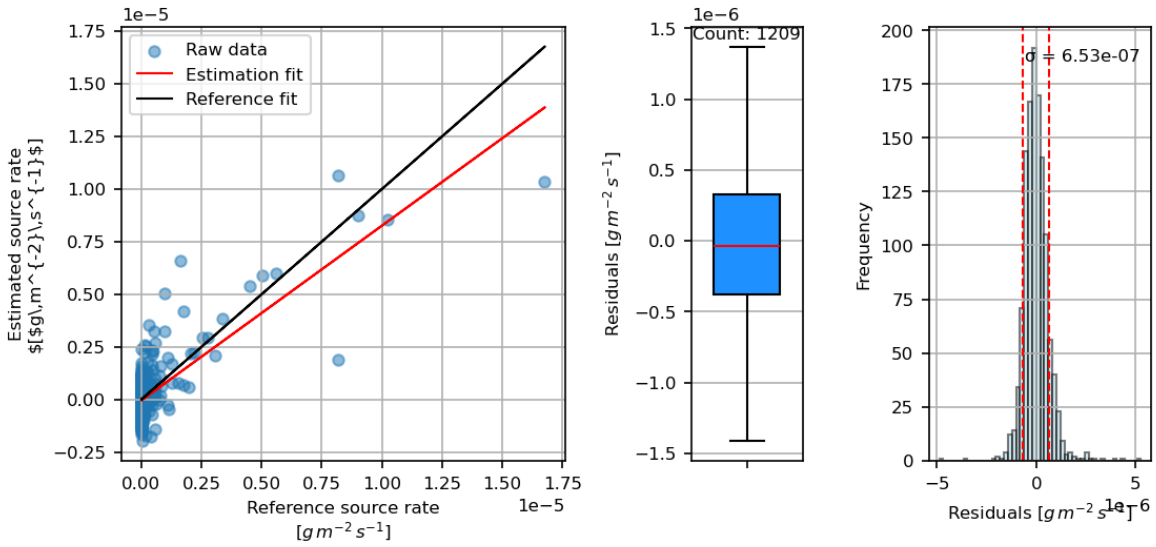

Figure 4.18: Results of the SQ1_0_C test run. Left: plot of each pixel's estimated emission value (x) compared to each reference value from the simulated source (y) overlayed with the corresponding fitted regression line (black) and reference (red). Middle: Distribution of the absolute error over the scene. Right: Histogram of the residuals around the reference values.

Some statistics can then be derived from this plot that can be used to assess system performance: first, the residuals Δq_i can be visualised as the vertical distance between q_i and the 1:1 line and their mean and standard deviations can be plotted on a histogram and box-plot (see Figure 4.18 middle and right) which gives a quick idea of the bias and spread of a run. Furthermore, a least-squares regression can be done on the points which yields a line of the form $m \cdot Q_{ref} + b$ where $m = 1$ and $b = 0$ indicate a perfect overlap with the reference line. The Pearson correlation coefficient r is also derived for the two quantities in order to inform on the spread of the residuals: indeed, a perfect line may still be obtained if residuals cancel out and so quantifying r is necessary to capture all the relevant information. These quantities will be used in chapter 5 to answer the research questions defined in section 3.2.

4.5.4. Uncertainty estimation

Finally, it is desirable to provide an uncertainty estimation along with the total source rate. This is done for TROPOMI observations by running a time-series where estimations are done weekly or monthly: the total emission estimation is then the average of the sub-estimations and the uncertainty is estimated as three standard deviations of the sub-estimations within the averaging period. This simplistic approach provides an uncertainty range and is simple to implement but is more akin to a measure of temporal variability and only holds for steady sources. Furthermore, shortening the averaging period changes the estimation's performance and requires multiple scenes making it computationally expensive.

A better approach is to aggregate the pixel-wise uncertainty of the final emission estimate using Equation 4.13. The value of each pixel's uncertainty is assumed to be the pixel-wise residual between the emission estimation and the reference estimation (seen in Figure 4.18). This assumption leads to uncertainty ranges which are representative of the pixel-wise spread but only works for the simulated observations. Further work is thus needed to find a valid pixel-wise estimation of the uncertainty for real observations.

$$Q_{est} = \Sigma_{i=1}^{N} E_i \cdot A_i \tag{4.13}$$

$$\sigma^2_{Q_{est}} = \Sigma_{i=1}^{N} (\sigma_i \cdot A_i)^2 \tag{4.14}$$

$$\sigma_{Q_{est}} = \sigma_d \cdot A_{pix} \cdot \sqrt{N_{pix}} \tag{4.15}$$

The first method is thus used for the Permian case study while the second is used for all synthetic observations with multi-point sources.

5

Results

This chapter will discuss the results of the verification and investigation tests conducted in this thesis. First, the tests using Gaussian plumes will be investigated in section 5.1, then the WRF results will be introduced in section 5.2 before looking at each sub-question: starting with SQ1 discussing the choice the gradient approximations in subsection 5.2.3, SQ2 assessing the impact of the estimators' order of operations subsection 5.2.4, subsection 5.2.5 will compare the background corrections and answer SQ3 while SQ4 will conclude on method optimisation in subsection 5.2.6. Finally, a case study will be conducted on the Permian basin in section 5.3.

5.1. Gaussian plumes

In order to establish a baseline and verify the implementation of the divergence-based methods, a series of tests are conducted using synthetic Gaussian plumes. These idealized cases are selected for their simplicity and analytical clarity, making them well-suited for method verification. Gaussian plumes provide a clear and controlled environment to test the behaviour of each component of the codebase, validate expected outputs, and ensure the robustness of the pipeline under ideal (non-realistic) conditions. The visual simplicity of these point sources allows for intuitive inspection of estimation results and serves as a reference point for interpreting outcomes from more complex or realistic datasets in later sections.

5.1.1. Verification

The verification approach comprises two stages. First, each variable of interest—such as the wind field, gradient components, divergence values, and final emission estimates is varied individually and the resulting emissions fields are inspected to ensure their spatial distribution and approximation error is within the expected bounds. This is followed by a structured testing loop that cycles through the three main codebase blocks (input, estimation, integration), and sweeps through all possible values of each setting for each block. This dual approach is intended to balance computational efficiency with the need to assess interactions between code components.

The domain investigated has an extent of 2.5 degrees and runs for a time period of 8 observations. Gaussian plumes used a wind speed of $w = 5m/s$, source rate of $Q = 10k/s$, constant of turbulent diffusion $K = 6000m^2/s$ and a direction changing by $\Delta\theta = 45^o$ with an added background of $B_0 = 1.0g/m^2$, noise of $\sigma_B = 0.1g/m^2$ and 1% missing data. No filtering was done and the estimation used a weekly flux-averaged divergence (E2) resampled to a regular 0.1 degree resolution with 'combo' gradient order, a median-masked background correction and perfect knowledge of the wind field. The combination of gradient direction was used as the perfectly uniform wind field rotated by increments of 45^o would otherwise yield artefacts on half the scenes. Only the diffusion correction (see Equation 2.4.6) was applied with $K = 6000m^2/s$ such that it perfectly matches the turbulent diffusion constant of the plumes generated. Finally, the emission field was integrated in a 100 km circle around the centre of the domain where the plume head is placed.

The results of the sensitivity analysis sweep are shown in Figure 5.1 which demonstrates that the error is generally centred around zero. A tendency towards underestimation is observed due to the addition of missing data (see Figure 5.1.2) while the rest of the outliers can be attributed to added noise (Figure 5.1.2) and changes (Figure 5.1.2) in the assumed constant of turbulent diffusion.

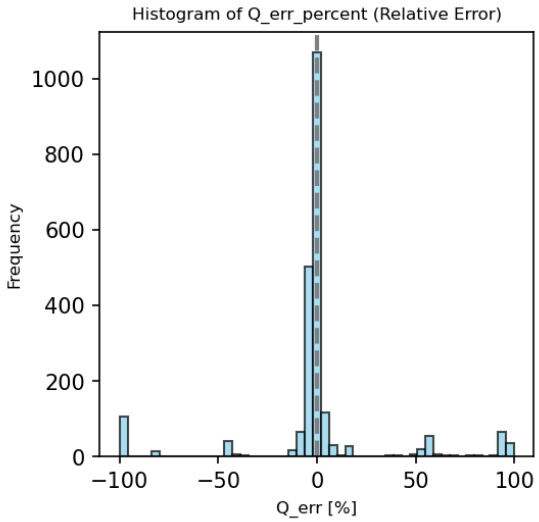

Figure 5.1: Histogram of the integrated source rate error over the range of trials

5.1.2. Impact of testing parameters

This section will inspect some of the results obtained in order to provide a controlled baseline for the behaviour of the divergence method and the impact of some parameters before delving into the more realistic WRF-Chem simulations.

Averaging

Averaging emission estimates over longer time periods offers clear advantages, notably through increased pixel coverage and reduced sensitivity to random noise, resulting in more stable and consistent outputs. However, this approach also comes with limitations, as it smooths out short-lived emission events and may obscure seasonal or episodic variability that could be of scientific or regulatory interest which should be considered when using these methods and for that reason a monthly average was chosen for E2.

The impact of averaging can be clearly shown by the next two examples. On the left, Figure 5.2 shows the enhancement (left-most) and estimated emission map (to its right) of a single plume which exhibits the “horseshoe” pattern, also observed in Roberts et al. 2023 and Koene, Brunner, and Kuhlmann 2024 where the source itself is clearly identified but the diffusion in the tail causes a seemingly ’negative’ emission on the centerline and a ’positive’ emission cross-wind which is due to the diffusion of the trace gas from the centre outwards. This artefact is characteristic of the divergence method on plume observations with relatively high diffusion (see subsection 2.4.1). On the right: Figure 5.3 shows the average enhancement of eight plumes, each rotated by 45^o in order to produce distinct observations, on the 3rd panel and the resulting divergence-averaged emission map in the right-most panel. The source in this case is even clearer and the horseshoe diffusion artefacts are smoothed out as the positive outer edges of one plume cover up the negative inner edge of their neighbours and cancel out. This is of course an ideal case in which the plumes are perfectly rotated but it exemplifies the potential of averaging. The integrated total sources of the single plume is estimated to be $Q_{est,1} = 7.1511 kg/s$ whereas the multi-plume estimates finds $Q_{est,8} = 9,9593 kg/s$ which is much closer to the true $Q_{ref} = 10.000 kg/s$.

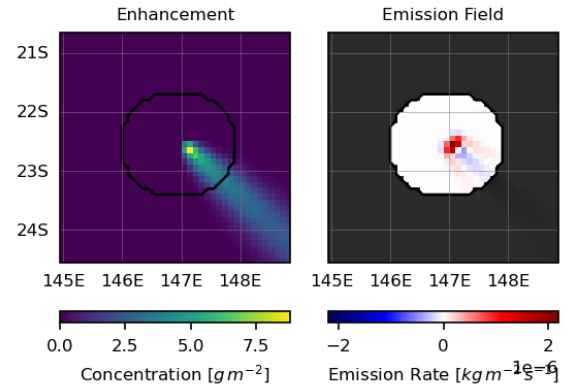

Figure 5.2: Enhancement of the simulated Gaussian column density of a single plume in uniform wind field (Left) and the resulting estimation (Right)

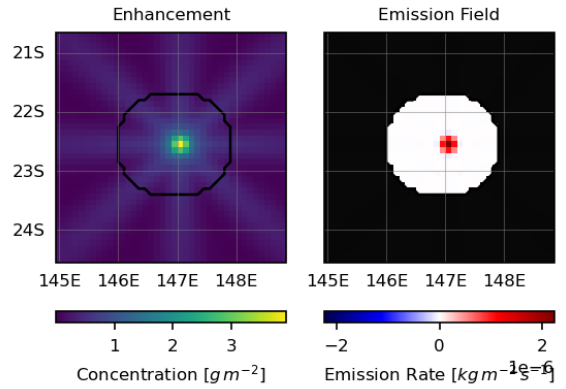

Figure 5.3: Enhancement of the simulated Gaussian column density of eight plumes in uniforms wind fields of varying directions (Left) and the resulting estimation (Right)

This can be seen to be generally true by filtering the results of the Gaussian sensitivity analysis by the length of the time period that is averaged and showing a box-plot of the results given all other varying settings in Figure 5.4. Given a start date of 2022/01/03 and an end day of 2022/01/03 (i.e. 3 in END_DAY_INT) we find an error of 2.5% to 6.0%, averaging over two days (i.e. ending on the 4th day) leads to both a lower underestimation and lower sensitivity to other parameters such as noise or missing data as indicated by the spread reducing to a range of 2.5% to 3.0%. Finally using 8 days yields an estimate of $Q_{est} = 9.987 \pm 0.07 kg/s$.

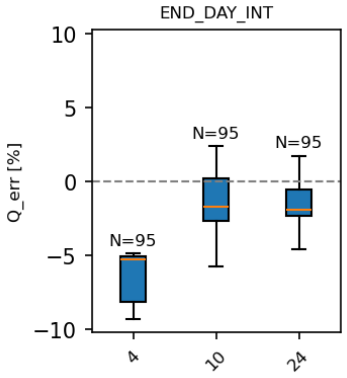

Figure 5.4: Boxplot of the results of Gaussian testing, aggregated per value of the end day parameter i.e. length of the averaging period or number of plume observations considered

Missing data

Missing data points were initially introduced into the Gaussian data sources to test the robustness of the divergence implementation with respect to nan and zero values, especially in the averaging and resampling phase. But an interesting observation to be made is that, because each pixel in the emission estimate grid requires all its neighbours to be valid pixels, a single missing point in the input grid results in 4-8 missing points in the output grid. This can be seen clearly in Figure 5.5 where 1% of pixels are missing in each of the 8 plumes averaged resulting in virtually no gaps in the column density average (left-most) whereas the emission map using the same data (left) already shows some NAN parts. Pushing this further to 25% of missing pixels yields Figure 5.6 where the column density grid starts to show gaps (right) but results in unusable emission map (right-most).

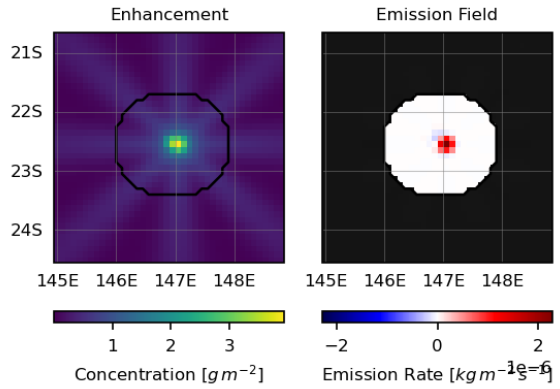

Figure 5.5: Enhancement of the simulated Gaussian column density with 1% of missing pixels (Left) and the resulting estimation (Right)

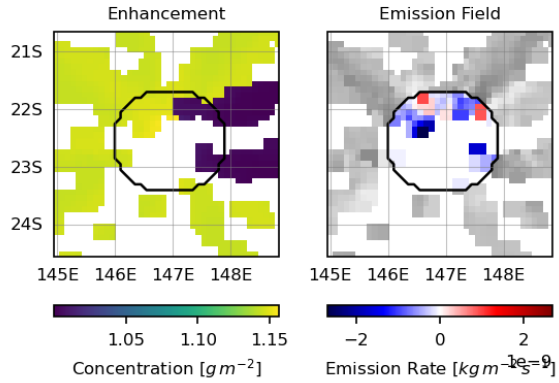

Figure 5.6: Enhancement of the simulated Gaussian column density with 25% of missing pixels (Left) and the resulting estimation (Right)

An example of an emission grid based on the WRF emitters in Figure 5.7 with a fourth order orthogonal gradient approximation clearly shows the 'cross' pattern caused by a few missing pixels in the scene. The results of the sensitivity shows that increasing the percentage of missing data both decreases the estimated emissions due to source pixels being masked and the uncertainty and sensitivity to other parameters increasing (see Figure 5.8).

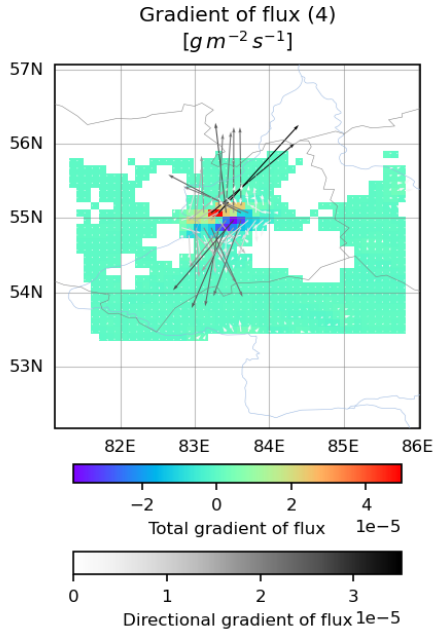

Figure 5.7: Example of the divergence field for a TROPOMI observation with few missing pixels and fourth order gradient.

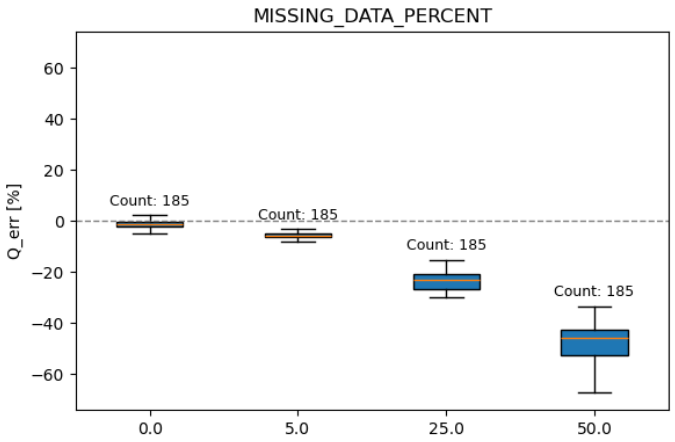

Figure 5.8: Boxplot of the results of Gaussian testing, aggregated per value of the Missing Data Percentage parameter

Background

The impact of the addition of both a flat and noise background component to the observations can be seen by comparing the enhancement of the column density for a 'clean' plume set in Figure 5.3 and a 'noisy' plume set in Figure 5.5. However, the impact on the estimation is surprisingly low as the clean observations yield $Q_{est,clean} = 9.9593kg/s$ whereas the noisy ones yield $Q_{est,noisy} = 9.9870kg/s$. This can be attributed to the fact a flat background will always have a null gradient and thus does not affect the results and that the Gaussian noise added here is independent from pixel to pixel meaning a fourth-order gradient approximation will be averaging it out to a quasi-zero gradient as well. The only

backgrounds truly affecting the divergence method are thus the ones with 'structure' due to orography convergent wind fields which have a non-zero gradient over a significant distance.

This is again seen in the box-plots below derived from the sensitivity analysis where the background component shows little to no influence in Figure 5.9 : the 1.0 setting is biased by the influence of missing data a seen previously which causes it to have a wider spread but all backgrounds settings tested have a median and average value within 5% of the reference emission. Figure 5.10 shows how an increase in noise, though mitigated, does increase the error and uncertainty of an estimation while Figure 5.11 shows the influence of background corrections are mostly negligible with the notable exception of the median and in particular median-masked method which is able to get rid of the noisy background and thus achieves a lower overall error by correctly identifying the plume (note that this is not generally applicable to TROPOMI or realistic observations where sources are distributed and backgrounds structured).

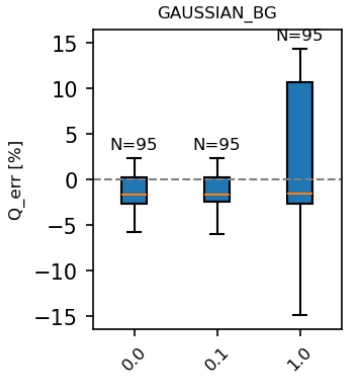

Figure 5.9: Boxplot of the results of Gaussian testing, aggregated per value of the flat background parameter

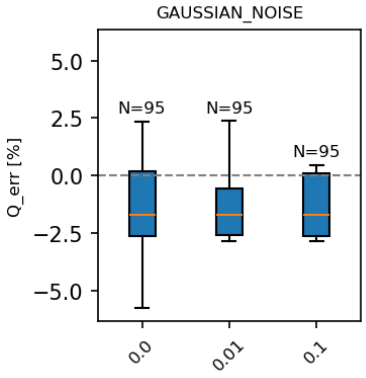

Figure 5.10: Boxplot of the results of Gaussian testing, aggregated per value of the Gaussian background noise parameter

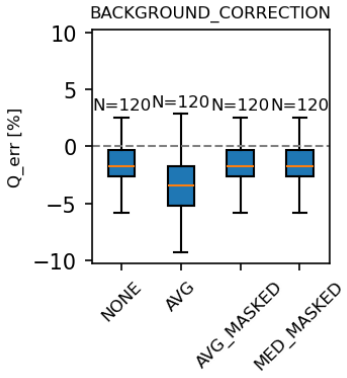

Figure 5.11: Boxplot of the results of Gaussian testing, aggregated per value of the background correction parameter

Diffusion

Finally the effect and validity of the diffusion-correction can be shown by looking at the subset of estimations without any correction (NONE) that still had a diffuse plume of $K = 6000m^2/s$ compared to the same set of plumes estimated with the diffusion correction enable and a constant of turbulent diffusion exactly known (6000). Figure 5.12 shows that the underestimation is drastically reduced, in accordance with the findings of Roberts et al. 2023.

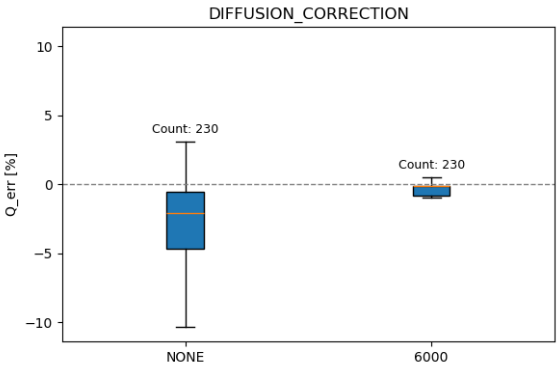

Figure 5.12: Boxplot of the results of Gaussian testing, aggregated per value of the Gaussian diffusion-correction parameter (using K=6000 in Gaussian generation)

5.2. Simulated WRF observations

The next section will discuss the results obtained by testing the divergence method and its variations with the WRF simulations of RUS-domain (see subsection 4.3.3). This significant jump in complexity will naturally lead to weaker estimates and more difficult interpretation of the results.

5.2.1. Sensitivity analysis

First, a sensitivity analysis was conducted, similarly to subsection 5.1.1 which will not be discussed in full here but instead shown where relevant as part of the discussion on the research questions in subsection 5.2.2. This was also the last step in verification of the divergence pipeline which was approached in the same way as the Gaussian verification (see results in Figure 5.13), ensuring the effects hidden by the simplicity of the Gaussian plumes (e.g. 180^o grid rotations being inconsequential due to plume symmetry). Wind fields resampling and multi-pixel source were checked to be handled properly and all inputs (see section 4.3) were correctly formatted and scaled.

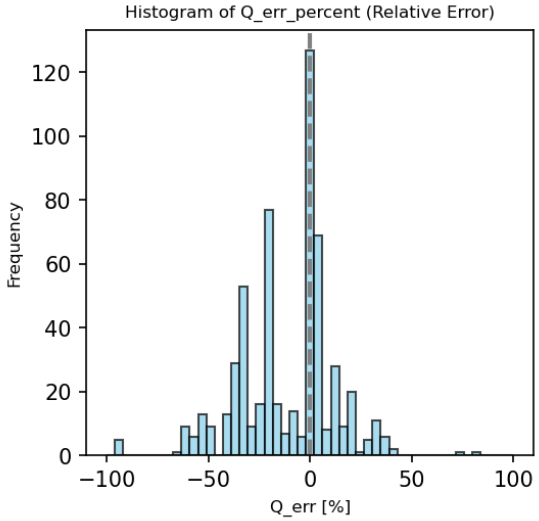

Figure 5.13: Histogram of the integrated source rate error over the range of WRF trials

5.2.2. Effects of parameters on synthetic observations

This subsection will now delve into the focus of this thesis: method and parameter optimisation through specific tests devised to answer the research questions defined in section 3.2.

5.2.3. Gradient approximations

First is the investigation of the impact of the numerical order of the gradient operator approximation (2, 4, combo) in order to answer SQ1.

A first look at the sensitivity plots of the Gaussians testing in Figure 5.14 shows results expected based on subsection 2.4.3 for ideal, background free observations in a uniform wind field, that is, the fourth order gradient performs best, second order performs worst and the combination sits in the middle. The same test with WRF simulations in Figure 5.15 reveals a more nuanced situation for realistic observations where the combo and second order seem to perform similarly.

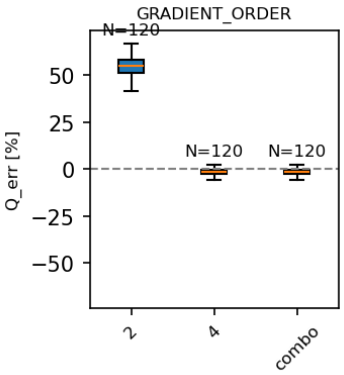

Figure 5.14: Boxplot of the integrated source rate error over the range of Gaussian trials with orders 2 / 4 / 2+4 combo.

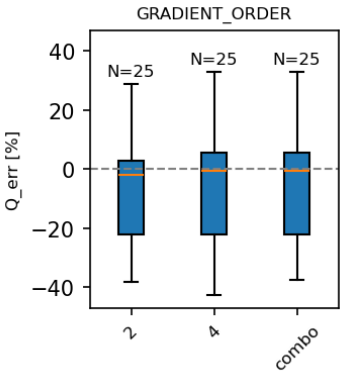

Figure 5.15: Boxplot of the integrated source rate error over the range of WRF trials with orders 2 / 4 / 2+4 combo.

In order to get a more in-depth understanding of the behaviour seen in Figure 5.15, three tests are defined using gradient order 2, 4 and combo, as per Table 5.1. These are using the monthly-averaged divergence E1 estimator over a year-long period (2022) with tracer 3 only (i.e. background-free) such that the influence of the gradient approximator on the estimation of point sources can be investigated first before adding a background in subsection 5.2.6. Since no backgrounds are present, no correction is applied. It should be noted that all results obtained at this stage are conditional upon the choice of estimator (here E1) which will be investigated next in subsection 5.2.4. A confirmation of the results is done for all estimators considered in subsection 5.2.6.

Table 5.1: Test definition for investigating research sub-question 1 (SQ1) on background free observations (0) for gradients order 2 (2), 4 (4) and combination (C)

TEST	WRF tracers	averaging period	gradient order	estimator	background correction
SQ1_0_2	3	monthly	2	DIV	none
SQ1_0_4	3	monthly	4	DIV	none
SQ1_0_C	3	monthly	combo	DIV	none

The results obtained are compared below: The first observation made is from Figure 5.16 which shows that more diffuse emitters with varied wind fields show a clear enhancement pattern after averaging of the support variables. Second, Figure 5.17 shows a clear emission spot of the same shape as tracer 3's EMIS file along with noise patterns around it. Looking at the emission map of gradient orders 4 or combo are scarcely informative as their pattern and magnitude look almost identical, the difference grids 4 and 2 is thus shown in Figure 5.18 which includes the expected difference in noise throughout the images as well as an underestimation of gradient order 2 at the main source point and an overestimation directly around it. This may be explained by the configuration of neighbouring pixels considered in gradient order 2 which notably exclude the middle pixel meaning the gradient of two directly adjacent pixels cannot be detected by this method whereas the fourth order gradients does have 'arms' of directly adjacent pixels. This makes the 4th order approximation more suitable to identify discrete or small sources. Finally, the difference between 4 and C is simply zero in all places except at the edges where the second order values are used.

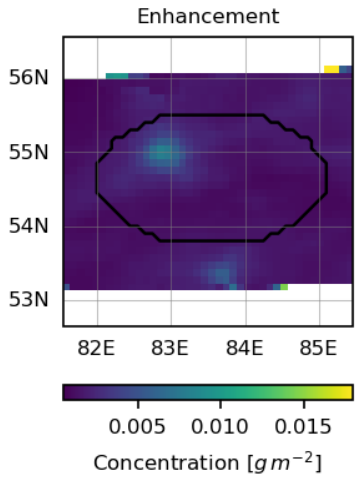

Figure 5.16: Averaged enhancement of the simulated observations

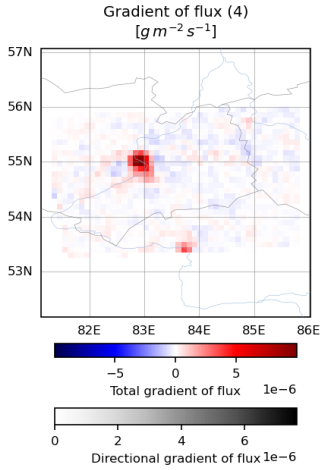

Figure 5.17: Resulting emission map based on Figure 5.16 with DIV estimator and second order gradient approximation

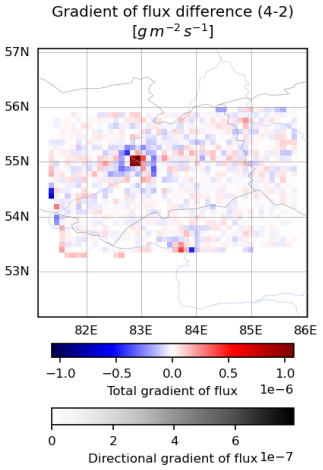

Figure 5.18: Difference between gradient of fluxes approximated with fourth and second order gradients (4-2)

Further insight is gained by examining the resulting statistics shown in Table 5.2: it can be seen that the variations in estimation of the total emissions E_{est} is relatively small compared to the error. It should also be noted that although order 2 has a marginally lower error (18.85%) compared to order 4 and combo (19-20%) the fourth, and to a lower extent the combination of orders, both exhibit better correlations with a slope m closer to 1 and a Pearson correlation coefficient $r > 0.8$. This means the better estimate of order 2 is likely a product of noise instead of an indicator of a better estimate.

Table 5.2: Test results for investigating research sub-question 1 (SQ1) on background free observations (0) for gradients order 2 (2), 4 (4) and combination (C)

Test ID	E_{true} [ton/h]	E_{est} [ton/h]	ΔE [%]	σ_E [ton/h]	σ_E [%]	slope m	bias b	Pearson r
SQ1_0_2	5	5.943	18.85	0.547	10.95	0.746	3.7E-09	0.753
SQ1_0_4	5	5.969	19.37	0.585	11.7	0.822	7.5E-10	0.763
SQ1_0_C	5	5.959	19.17	0.592	11.84	0.808	2.4E-09	0.754

The probable reason why 4 behaves better than 2 is two-fold: first, the error of the mathematical approximation is of two fewer order as per subsection 2.4.3, second, since 4 considers adjacent pixels it tends to 'smudge' or smoothen the divergence map from one pixel to the next yielding less noisy emission estimates whereas the gap in 2's center lead to absolutely uncorrelated adjacent pixels. This makes the fourth order method better for coarse grids or domains with noisy observations or small sources. The combo gradient acts exacly like 4 (by definition since it uses the fourth order gradient unless missing pixels prevent it) which explains why the correlation and total estimate are so close to the fourth-order in this case, trending to look closer to the second-order estimate as the proportion of missing pixels increase.

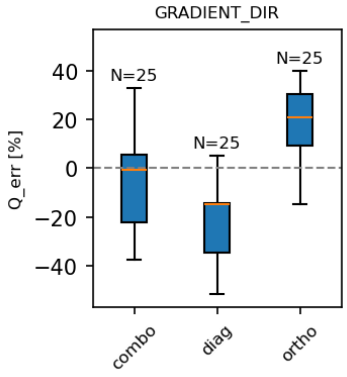

Figure 5.19: Boxplot of the integrated source rate error over the range of WRF trials, aggregated per gradient direction scheme.

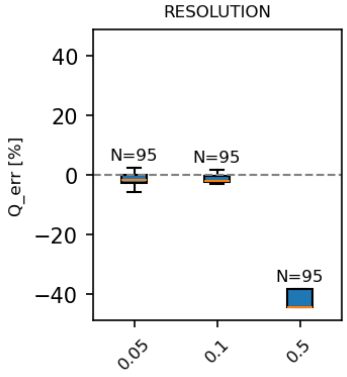

Figure 5.20: Boxplot of the integrated source rate error over the range of Gaussian trials, aggregated per resolution of the regular grid.

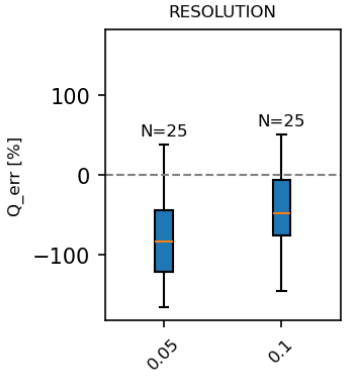

Figure 5.21: Boxplot of the integrated source rate error over the range of WRF trials, aggregated per resolution of the regular grid.

It should be noted that the gradient direction also has a notable impact as seen in Figure 5.19 based on the WRF results where both diagonal and orthogonal methods show significant bias compared to the combo (dynamic direction) method whose median emission estimate is has less than 5% error. The resolution of the regular target grid also has a significant effect: Figure 5.20 and Figure 5.21 show the impact of a coarser (0.1^o) and finer (0.05^o) grid for the Gaussian and WRF tests respectively. It can be seen that oversampling to a finer resolution has a negligible performance impact but coarsening the grid too much compared to the source dataset leads to higher errors. A finer grid does not seem to favour one numerical gradient approximation over another as no new data is added leading to the same trends.

5.2.4. Estimators

The order of operations distinguishing operators E1, E2 and DD are analysed similarly as subsection 5.2.3 by defining three specific test cases as per Table 5.3. These use the same settings as Table 5.1 except they all use combo gradient order since it was concluded to be the most representative and accurate. Both DIV,E1 and DD use a single-observation averaging period since they create each create one emission map per concentration map while DIV,E2 makes an emission map per 29-31 days (i.e. 20-50 observations). Once again the results here are conditional upon the choice of other parameters, especially the numerical order of the gradient (subsection 5.2.3), and thus need to be confirmed in subsection 5.2.6.

Table 5.3: Test definition for investigating research sub-question 2 (SQ2) on background free observations (0) for directional derivative averaged (DD), divergence averaged (DIVE1) and flux-average divergence (DIVE2) estimators

Test ID	WRF tracer	averaging period	gradient order	estimator	background correction
SQ2_0_DD	3	single	combo	DD	none
SQ2_0_DIVE1	3	single	combo	DIV	none
SQ2_0_DIVE2	3	monthly	combo	DIV	none

The tests results are tabulated in Table 5.4 where one can see that the variation in total estimated emissions ΔE is much wider than what was observed in Table 5.2 meaning the choice of estimator has a larger influence on the results than the choice of gradient approximator. Furthermore, it can be seen that DIV,E1 has the lowest error (0.6 %) followed by DIV,E2 (20%) and DD (25%) but DIV,E2 exhibits the best correlation with a slope of $m = 0.8$ and $r = 0.75$ while both DD and E1 have similarly mild results with a slope of about 0.55 and Pearson correlation coefficient of around 0.65. This can be interpreted similarly to the case of subsection 5.2.3 where DIV,E2 is the most reliable estimator with a better pixel-wise estimate whereas E1 and DD have lower confidence (i.e. worst correlation) but a better estimate likely by the result of noise.

Table 5.4: Test results for investigating research sub-question 2 (SQ2) on background free observations (0) for directional derivative averaged (DD), divergence averaged (E1) and flux-average divergence (E2) estimators

Test ID	E_{true} [ton/h]	E_{est} [ton/h]	ΔE [%]	σ_E [ton/h]	σ_E [%]	slope m	bias b	Pearson r
SQ2_0_DD	5	3.749	-25.02	0.569	11.38	0.573	5.8E-09	0.646
SQ2_0_DIVE1	5	4.969	-0.62	0.575	11.5	0.56	1.0E-08	0.633
SQ2_0_DIVE2	5	5.959	19.17	0.592	11.84	0.808	2.4E-09	0.754

Looking at Figure 5.24 one can notice that only a few points contribute to the upper end of the correlation, that is, there are few pixels in the scene with high emissions. This means a small amount of noise in and around the source pixels can result in very different m, b, r values. Furthermore, it can be seen that Figure 5.23 and Figure 5.22 look very similar in their points driving the estimation line, especially around the source with the same pixels being overestimated (top left) and drastically underestimated around $(1.6, 0.4)$ and $(3.4, 1.3)$ which exemplifies how E1 and DD are essentially the same on background-free observations. Finally, it can be noted in all figures that most of the pixels are seen below $Q_{ref} < 0.5[g \cdot s^{-1} \cdot m^{-2}]$ (i.e. background regions with little to no emitters) and their noise levels range $\pm 0.5[g \cdot s^{-1} \cdot m^{-2}]$ and observed in Figure 5.24 that the noise levels converge towards zero quasi-linearly, with emissions, as seen in the Gaussian tests of Figure 5.10 whereas E1 and DD have more fuzzy noise levels.

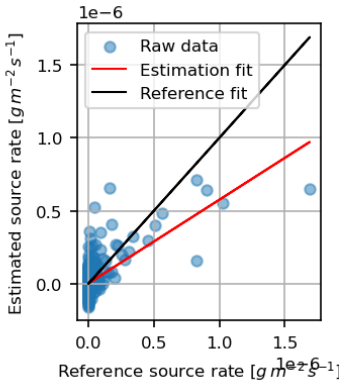

Figure 5.22: Fitted regression line (black) of each pixel's estimated emission value using DD (x) to each reference value from the simulated point source (y) overlayed with optimal expected reference (red)

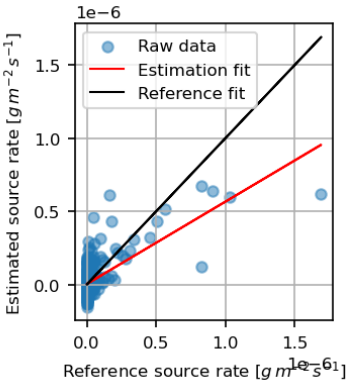

Figure 5.23: Fitted regression line (black) of each pixel's estimated emission value using DIV E1 (x) to each reference value from the simulated point source (y) overlayed with optimal expected reference (red)

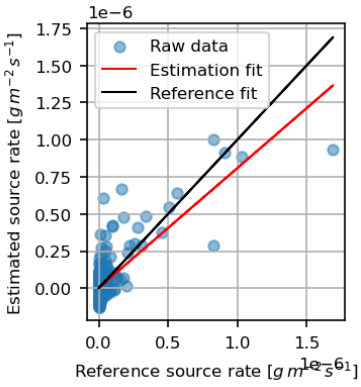

Figure 5.24: Fitted regression line (black) of each pixel's estimated emission value using DIV E2(x) to each reference value from the simulated point source (y) overlayed with optimal expected reference (red)

These observations reveal that the change in order of operation between E1 and DD is minimal and that the linearity of the gradient and product operators holds for complex applications (Equation 5.1) whereas the averaging operator results in wildly different outcomes. In order to investigate the reason for the difference between DD or E1 and E2, one can first look at the formulation of the estimators in Equation 2.17: since the concentration field and wind are quasi-perfect (no background, same field used in WRF-Chem and DIV) the difference cannot come from terms $\bar{u}$ or Ω. Furthermore, since E1 and DD behave in such a similar way, it can be seen through Equation 5.1 that the placement of the gradient operator is not causing the difference observed meaning we should look more closely at the flux-averaging step.

$$\bar{E}_{dd} = \langle \bar{u} \cdot \nabla(\Omega) \rangle \approx \bar{E}_{div,E1} = \langle \nabla(\bar{u} \cdot \Omega) \rangle \Rightarrow \bar{u} \cdot \nabla(\Omega) \approx \nabla(\bar{u} \cdot \Omega) \tag{5.1}$$

The resulting emission maps of E1 (Figure 5.25), E2 (Figure 5.26) and their difference E2-E1 (Figure 5.27 can further inform on the reasons why E2 is less noisy than either other methods. DD is not shown since it was seen to be similar in magnitude and spatial distribution to E1. Our first observation is that the maximum magnitude of the estimates in Figure 5.26 are higher ($2.0 \cdot 10^{-9}[kg \cdot m^{-2} \cdot s^{-1}]$)than in Figure 5.25 ($1.2 \cdot 10^{-9}[kg \cdot m^{-2} \cdot s^{-1}]$) which support the fact seen above that E2 has a lesser tendency towards underestimation. Furthermore, the noise distribution of E2 is of lesser relative magnitude and less structured than in E1 which shows large regions of positive and negative emissions which is not only an issue for total emission integration but also for visual inspection of a general-purpose emission map as it would make it more difficult to distinguish true sources from noise. Finally the difference of the two confirms these observations and reveals a maximum pixel-wise difference of about $0.5 \cdot 10^{-9}[kg \cdot m^{-2} \cdot s^{-1}]$ i.e. around 15% with a clear underestimation of E1 and DD around the source area compared to E2.

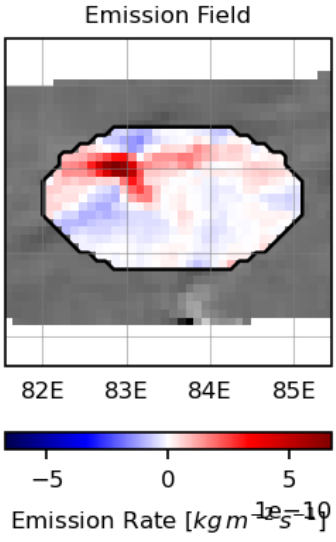

Figure 5.25: Resulting emission map with DIV-E1 estimator

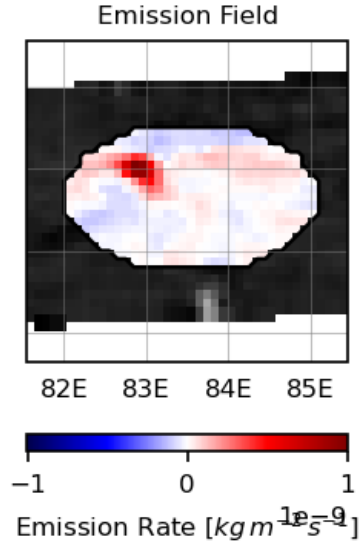

Figure 5.26: Resulting emission map with DIV-E2 estimator

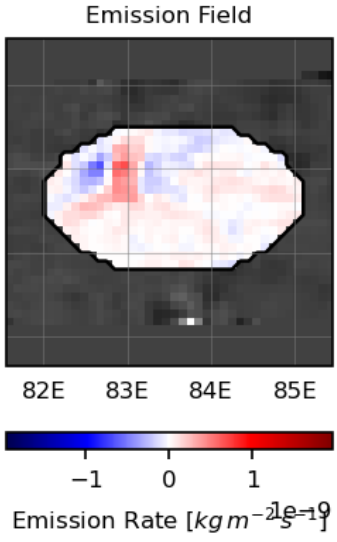

Figure 5.27: Difference between the emission maps with DIV E2-E1 estimators

In order to determine why flux-averaging yields better results than E1, a year-averaged test is conducted. The averaged results are first discussed below and intermediate vector fields are then plotted for three days of interest in order to better understand the behaviours at play in the following section. This analysis used a fourth-order orthogonal gradient in order to simplify comparisons and better highlight the effect of the estimator choice.

The average enhancement averaged over a year (Figure 5.28) already indicates a clear source spot since the observations here are background free and the CH4 is carried away from the source in every

direction. The average flux, seen in Figure 5.29 shows that, interestingly, the fluxes over a long time period seem to align in one main direction. Furthermore, the background is consistently close to zero and the source itself can be noticed to be quasi-null as well whereas the highest fluxes are observed directly downwind from the source in both the north-east and south-west directions. The effects of this flux distribution are clear from the resulting gradient Figure 5.30 which is even more defined that the monthly-averaged Figure 5.26: The gradient of the fluxes, i.e. the estimated emissions, are indeed highest at the source of the two outgoing flux lines and their tail is almost completely cancelled out. The background not only has a low magnitude but also a random direction which contrasts with the well-defined field of Figure 5.29.

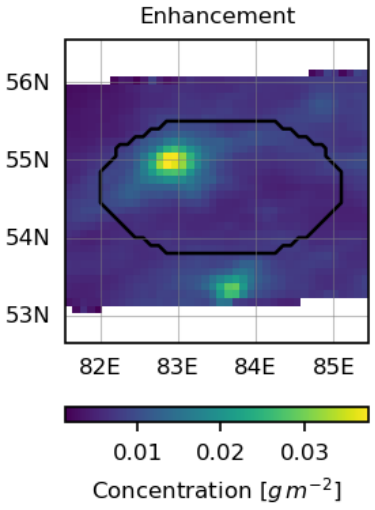

Figure 5.28: Yearly-averaged enhancement of the simulated observations

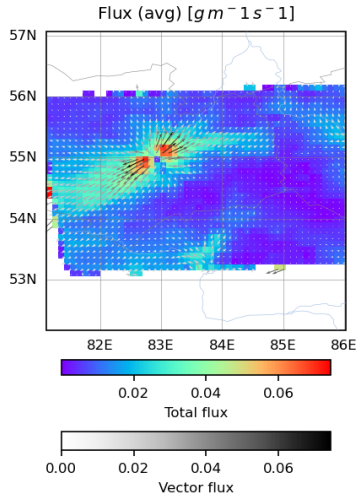

Figure 5.29: Averaged fluxes (yearly) of the simulated observations

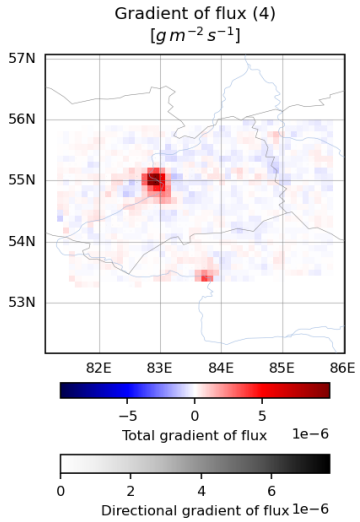

Figure 5.30: Gradient of averaged fluxes (yearly)

Day 12 has all the characteristics of a good day for using the divergence method: the wind field is uniform, the flux tail is straight and well-enhanced compared to the background and the source location can be easily inferred (Figure 5.31). Although the difference with respect to the average in Figure 5.32 shows the background fluxes are slightly higher than usual on that day, the location of the plume is clear and the noise relatively low. The result is Figure 5.33 where the source is clearly identified and the background quasi-null with the notable exception of a negative tail due to outwards diffusion, made clearer by the vectors of gradient direction, as seen in the Gaussian tests (Figure 5.2).

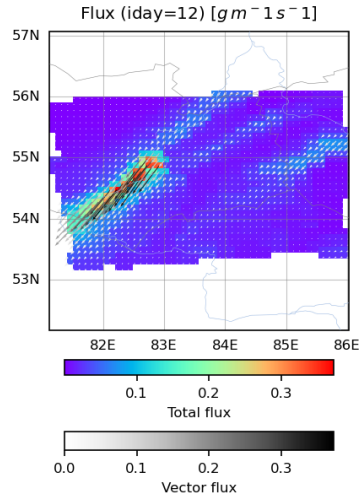

Figure 5.31: Flux of day 12

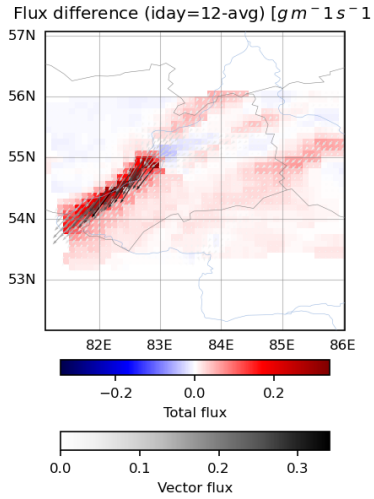

Figure 5.32: Flux difference of day 12 with respect to year-average

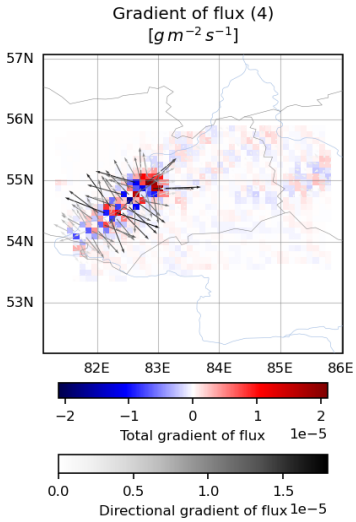

Figure 5.33: Gradient (4th Order) of the flux of day 12

The observation of day 152 (Figure 5.34) shows a curved wind field along which the plume is laid out and a mismatch between the real wind (along plume transport direction) and the estimated wind form GEOS-FP 50m (more uniform and with a south-north bias). Figure 5.35 also exemplifies a trend seen on many days where the plume is a net positive flux compared to the average and the background a net negative that seems to converge on the plume head or source. Figure 5.36 shows a surprising pattern: the source is identified, although smudged and slightly offset, and the tail exhibits a ”zebra” pattern of strong positive and negative estimates. This phenomena is likely due to aliasing - due to the wind field curvature, the gradient cross-plume interprets the outer part of the plume as a negative emission (trace gases are removed) and the inner part as a positive emission i.e. turning. This is combined with an aliasing artefact due to the relatively thin plume (2-4 pixels) whose gradient is computed with a 5-wide, 4th order gradient (a similar zebra noise pattern can also be seen to a lesser extent in Figure 5.33). Since these noise patterns appear frequently within plume tails and plumes will cover a vast amount of directions over a long enough time period, flux-averaging or divergence-averaging would reduce their impact.

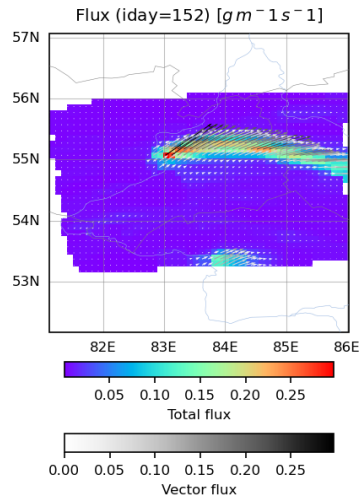

Figure 5.34: Flux of day 152

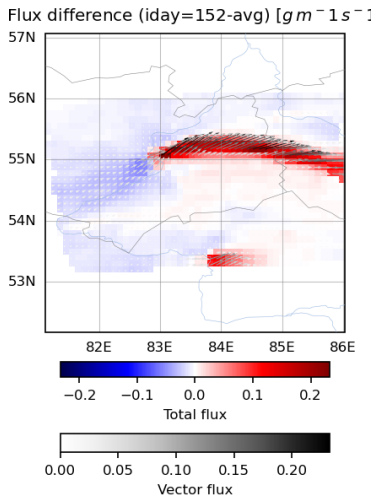

Figure 5.35: Flux difference of day 152 with respect to year-average

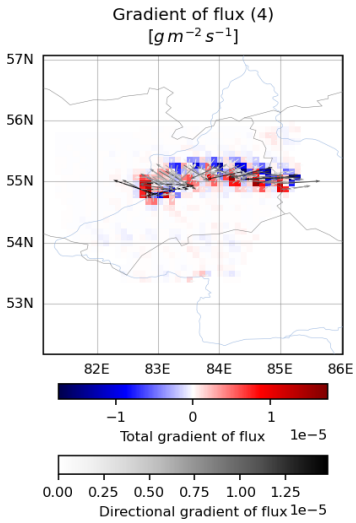

Figure 5.36: Gradient (4th Order) of the flux of day 152

Finally Day 83 shows, in Figure 5.37, what happens when the wind carries the trace gases into a region of missing data, effectively masking the tail of the plume. Although the flux at the source is clearly much higher than the yearly average (Figure 5.38) and would thus affect the year-averaged flux and the result of the E2 method, the missing neighbouring pixels render this observation useless when applying E1 or DD as the source region cannot be estimated as seen in Figure 5.39. One can also note that a similar effect is seen with the secondary source in Figure 5.34 around $(53.5^oN, 84.0^oE)$ which is masked out in Figure 5.36. Masking of source or near-source pixels is thus thought to be the leading factor in the superiority of E2 over E1 and DD estimators.

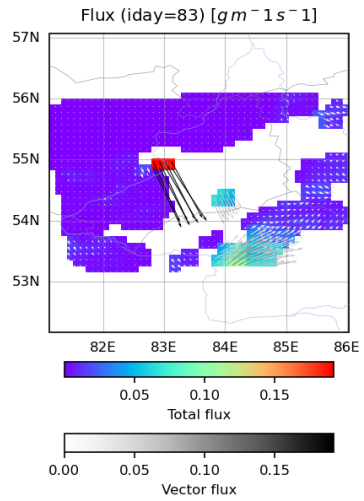

Figure 5.37: Flux of day 83

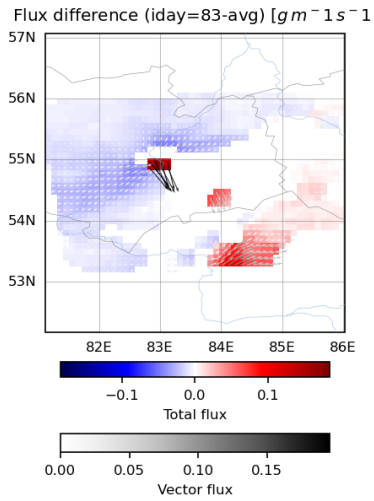

Figure 5.38: Flux difference of day 83 with respect to year-average

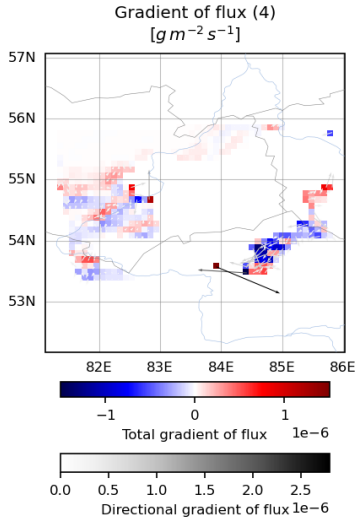

Figure 5.39: Gradient (4th Order) of the flux of day 83

A short inspection of the sensitivity analysis of the WRF averaging period in Figure 5.40 confirms the results seen before in Gaussians and in this section that averaging over multiple observations usually increase result reliability. Furthermore, filtering by estimator type where FLUX is the divergence-based E1 and E2 methods and CONC indicates the DD method, we can see in Figure 5.41 and Figure 5.42 that the influence of the estimator choice is of lesser importance when considering more complex data since the error is driven by other factors such as wind uncertainty. In either case, the DD estimators do not seem to offer a clear advantage over the baseline DIV method.

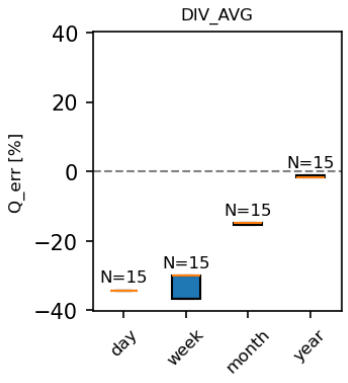

Figure 5.40: Boxplot of the integrated source rate error over the range of WRF trials, aggregated per averaging period.

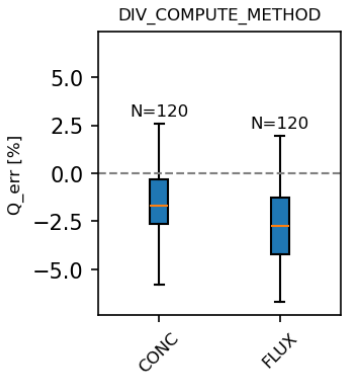

Figure 5.41: Boxplot of the integrated source rate error over the range of Gaussian trials, aggregated per estimator.

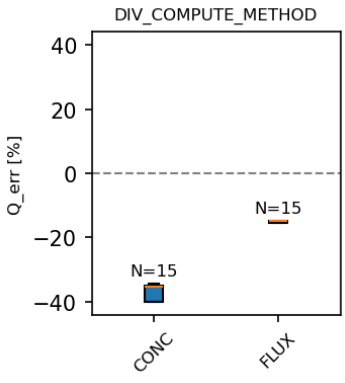

Figure 5.42: Boxplot of the integrated source rate error over the range of simulated WRF emission trials, aggregated per estimator.

5.2.5. Background correction

The last sub-question following this format is the investigation of background-correction performance. The background tracer (1) is added and three cases are tested for combo order, combo direction, DIV,E2 (monthly-averaged) estimator as per Table 5.5. The first, without any background correction (NONE) will serve as a reference and is not expected to provide useful estimates. The second will use the pressure correction (PRES) on the column density data and perform a background-removal correction on each observation based on the aggregated monthly concentrations and surface pressure. The third will perform a single correction on the monthly emission grids based on surface-level winds and topography (TOPO) using the assumed inverse scale height factor from Table 4.1.

Table 5.5: Test results for research sub-question 3 (SQ3) on observations with simulated backgrounds (1) for standard method (NONE), pressure-corrected column densities (PRES) and topography-corrected emissions (TOPO)

Test ID	WRF tracer	averaging period	gradient order	estimator	background correction
SQ3_1_NONE	1,3	monthly	combo	DIV	none
SQ3_1_PRES	1,3	monthly	combo	DIV	pressure
SQ3_1_TOPO	1,3	monthly	combo	DIV	topography

The statistics of the results shown in Table 5.6 immediately show that neither the uncorrected or topography-corrected emission estimates have any significant correlation with the WRF-EMIS grid with $m < 0$ and $r < 0$. This indicates the flux maps have high-magnitude noise that gets transferred through the gradient operator yielding estimates in the order of $q_i > 10^{-4}$ compared to $q_i < 10^{-6}$ for the pressure-corrected estimation. Furthermore, the error in either case is on the order of 1000% i.e. neither of these methods are valid for emission estimation as-is. The pressure-correction shows a good correlation with $m = 0.83$, $b \approx 0$ and $r = 0.7$ and the lowest error (45%) among the configurations tested. Figure 5.43 also shows the source pixels are all relatively close to the 1:1 line even though the noise level in the background is much higher than in Figure 5.24. The extremely large influence of background and background correction on errors and uncertainty is clearly seen here as the leading factor in errors for the divergence method.

Table 5.6: Test results for investigating research sub-question 3 (SQ3) on observations with simulated backgrounds (1) for standard method (NONE), pressure-corrected column densities (PRES) and topography-corrected emissions (TOPO)

Test ID	E_{true} [ton/h]	E_{est} [ton/h]	ΔE [%]	σ_E [ton/h]	σ_E [%]	slope m	bias b	Pearson r
SQ3_1_NONE	25	4396.398	17485.4	651.742	2606.94	-11.7	1.6E-05	-0.075
SQ3_1_PRES	25	13.574	-45.71	3.497	13.99	0.83	-4.3E-08	0.706
SQ3_1_TOPO	25	960.917	3743.63	786.331	3145.29	-0.72	-9.8E-06	-0.004

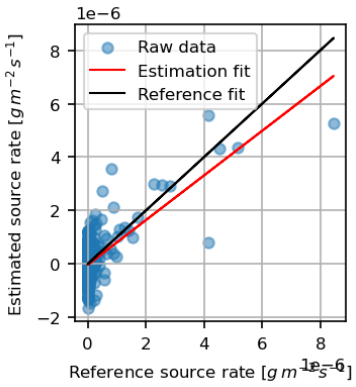

Figure 5.43: Fitted regression line (black) of each pixel's estimated emission value using PRESSURE (x) to each reference value from the simulated point source (y) overlayed with optimal expected reference (red)

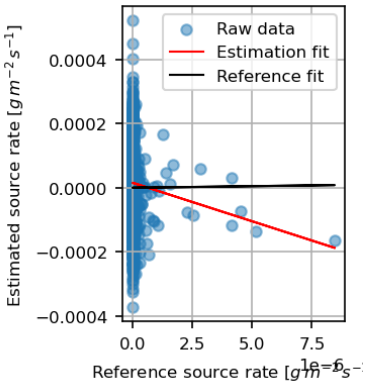

Figure 5.44: Fitted regression line (black) of each pixel's estimated emission value using NONE (x) to each reference value from the simulated point source (y) overlayed with optimal expected reference (red)

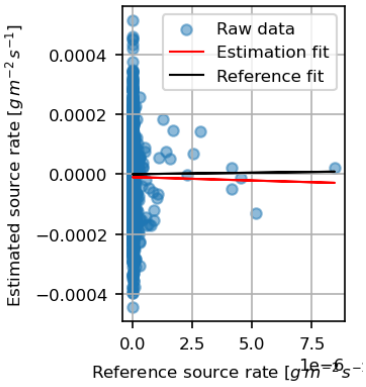

Figure 5.45: Fitted regression line (black) of each pixel's estimated emission value using TOPO (x) to each reference value from the simulated point source (y) overlayed with optimal expected reference (red)

The emission estimation maps shows the pressure-corrected Figure 5.46 identified a clear source area of magnitude $10^{-9}[kg \cdot m^{-2} \cdot s^{-1}]$ whereas the source is indistinguishable within Figure 5.48. The noise levels in both the topography-corrected emissions and the uncorrected emissions (seen in Figure 5.47) are on the order of $10^{-6}[kg \cdot m^{-2} \cdot s^{-1}]$, that is, three order of magnitudes higher than the signal observed in Figure 5.46. This means the pressure-correction was successfully able to filter out $\mathcal{O}(3)$ noise from the observations whereas the topography could not.

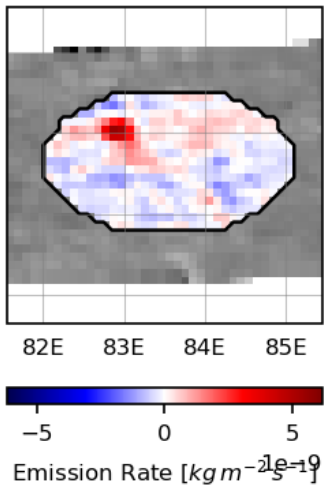

Figure 5.46: Resulting emission map with pressure correction

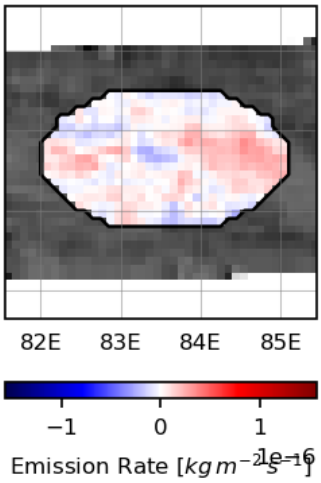

Figure 5.47: Resulting emission map with no corrections

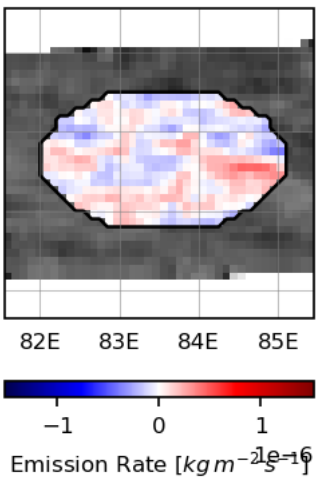

Figure 5.48: Resulting emission map with topography correction (X=0.006552)

A closer look at the topography correction is shown in Figure 5.49 where the uncorrected emissions, corrected emissions and correction term are shown from left to right. It can once again be seen that the magnitude of the correction is much too low to affect the results. it can, however, be seen that the correction does enhance the source region in the top-left of the image which means correctly tuned inverse scale height factor may yield much better results.

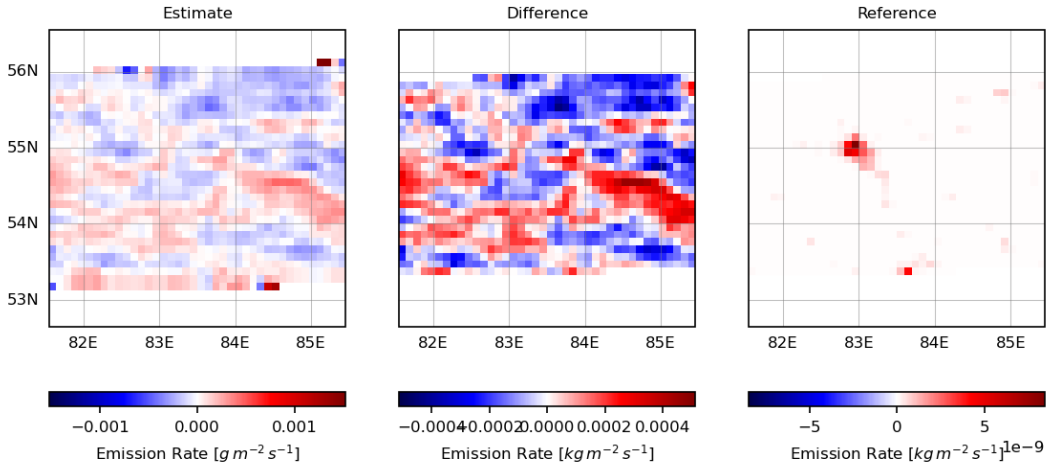

Figure 5.49: Uncorrected divergence map (left), topography correction (middle) and corrected emission map (right)

This is investigated as part of the sensitivity study on WRF simulations and shown in Figure 5.50 which aggregates the errors across the range of scale height factors derived in Table 4.1. $X = 0.008461$ which corresponds to $T = +50^{o}C$ does have a median error close to that of the pressure correction, although the sensitivity to other parameters is larger. This indicates the topography correction has the potential to be applied to correct the background if the magnitude of the correction is perfectly fitted to the domain and time of interest. It should be noted that the temperature yielding the best results here is not the physical temperature of the domain (Northern Russia) at the ground or at the effective wind height meaning using real temperature data is not guaranteed to yield any better results than assuming a reference temperature. Since the best scale height factor cannot be determined without prior simulations to estimate the relative abundances of trace gases throughout the air column as done in Sun 2022 or without 2D simulations with known emissions as shown in Figure 5.50, the topography-correction is concluded to be inapplicable to global TROPOMI methane without a new way of determining H in a reliable and automated way.

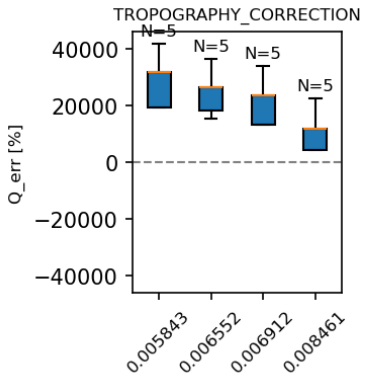

Figure 5.50: Boxplot of the integrated source rate error over the range of WRF trials, aggregated per topography correction factor X.

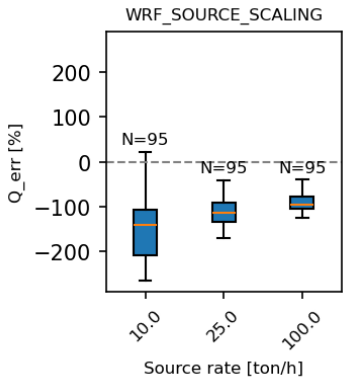

Figure 5.51: Boxplot of the integrated source rate error over the range of simulated WRF emission trials, aggregated per total integrated source rate.

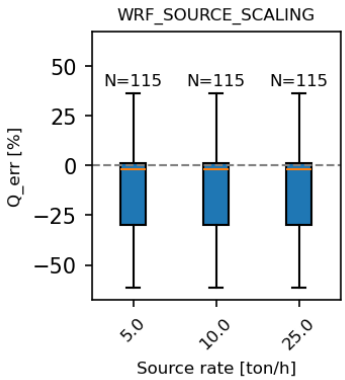

Figure 5.52: Boxplot of the integrated source rate error over the range of simulated background-free WRF emission trials, aggregated per total integrated source rate.

Determining the proper detection limit, that is, the minimum emission rate of a point source required to be detected by the method, would require a source fitting algorithm such as the on described in Beirle et al. 2023 and the study of varying source rates for both point and diffuse source across a variety of latitudes, surface albedos, etc. Such an analysis is thus outside the scope of this thesis.

However, the sensitivity analysis of the tests conducted shows that increasing the source rate of the WRF emission grids decreases the relative emission estimation error on observations tha contain a background component (see Figure 5.51). This is due to the increased prominence of the enhancement in the observations compared to the background which reduced in relative intensity. Indeed, the same test on background-free observation (Figure 5.52) shows no significant change in accuracy as the magnitude of the estimation and noise is scaled by the same amount. TROPOMI's usually accepted detection limit for methane plumes is around $Q_{min} = 5[ton/h]$ but it was seen that the divergence method's is closer to $Q_{min,DIV} = 25[ton/h]$ in the cases studied.

5.2.6. Multi-parameter optimisation

The final sub-question deals with the potential interactions between the parameters investigated so far i.e. whether any pair-wise combination of methods perform unexpectedly better or worse than what would be inferred from the conclusions ofsubsection 5.2.3, subsection 5.2.4 and subsection 5.2.5. Eight independent tests are devised to compare the fourth and combo (4+2) order of gradient approximation, DD and DIV,E2 estimators and the pressure and topography correction. All tests are conducted with a total source rate of $Q_{ref} = 25[ton/h]$ over a circular region of $R = 100[km]$.

Table 5.7: Test definition for investigating research sub-question 4 (SQ4) on observations with simulated backgrounds (1) for various combinations of the parameters tested in SQ1, SQ2 and SQ3

Test ID	WRF tracer	averaging period	gradient order	estimator	background correction
SQ4_4DDPRES	1,3	monthly	4	DD	pressure
SQ4_4DDTOPO	1,3	monthly	4	DD	topography
SQ4_4DIVPRES	1,3	monthly	4	DIV	pressure
SQ4_4DIVTOPO	1,3	monthly	4	DIV	topography
SQ4_CDDPRES	1,3	monthly	combo	DD	pressure
SQ4_CDDTOPO	1,3	monthly	combo	DD	topography
SQ4_CDIVPRES	1,3	monthly	combo	DIV	pressure
SQ4_CDIVTOPO	1,3	monthly	combo	DIV	topography

The results, shown in Table 5.8 shows an overall much higher error than in the background-free cases and a worse correlation, though notably the bias is always quasi-null. In all cases the pressure correction performs significantly better than the topography correction (as per subsection 5.2.5) and the difference between the flux-averaged divergence and the directional derivative estimator is similar to that observed in subsection 5.2.4 i.e. a marginally lower error for DD but a better correlation and thus higher confidence in the results for E2. The only change observed between the individual parameter testing done in the previous sections and this test is the fourth order gradient performing marginally better than the combination gradient in the case of pressure-corrected divergence estimation.

Table 5.8: Test results for investigating research sub-question 4 (SQ4) on observations with simulated backgrounds (1) for various combinations of the parameters tested in SQ1, SQ2 and SQ3

Test ID	E_{true} [ton/h]	E_{est} [ton/h]	ΔE [%]	σ_E [ton/h]	σ_E [%]	slope m	bias b	Pearson r
SQ4_4DDPRES	25	14.405	-42.4	3.650	14.6	0.626	2.4E-10	0.585
SQ4_4DDTOPO	25	-2931.120	-11824.4	431.514	1726.0	7.592	-2.0E-05	0.074
SQ4_4DIVPRES	25	13.669	-45.3	3.440	13.8	0.863	-6.0E-08	0.725
SQ4_4DIVTOPO	25	954.471	3717.8	790.776	3163.1	1.117	-1.2E-05	0.006
SQ4_CDDPRES	25	17.552	-29.8	3.054	12.2	0.566	2.0E-08	0.614
SQ4_CDDTOPO	25	-1688.471	-6853.8	214.399	857.6	6.361	-1.0E-05	0.124
SQ4_CDIVPRES	25	13.574	-45.7	3.497	14.0	0.830	-4.3E-08	0.706
SQ4_CDIVTOPO	25	960.917	3743.6	786.331	3145.3	-0.720	-9.8E-06	-0.004

A comparison of the emission estimation performance across all configurations for the ERA5 50m, ERA5 100m, GEOS 10m and GEOS 50m shows that the GEOS-FP source performs better than the

ERA-5 dataset (Figure 5.54). A lesser effect is seen on observations with a background component (Figure 5.53) where GEOS also has a wider spread than ERA5. This is not however a measure of the accuracy of the wind field datasets as the WRF simulations use GEOS-FP data to drive the chemical transport, it is expected that this dataset would perform better as the wind fields in the observations are perfectly consistent with the ones that drove the concentrations seen. Furthermore, the difference between the ERA5 and GEOS datasets, especially in background-corrected tests, indicates the choice of dataset has a lesser effect than the choice of estimator or background removal method.

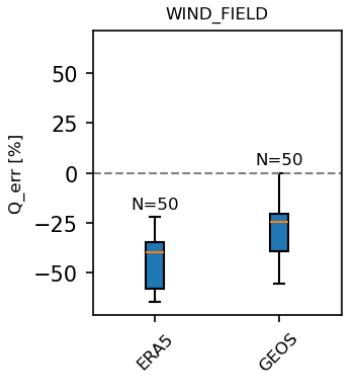

Figure 5.53: Boxplot of the integrated source rate error over the range of background-free WRF trials, aggregated per wind data source.

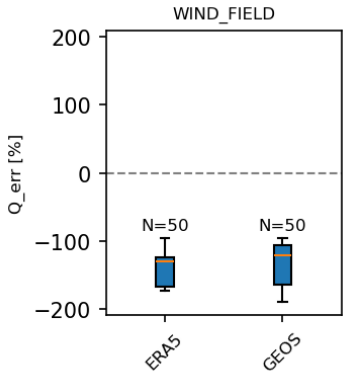

Figure 5.54: Boxplot of the integrated source rate error over the range of WRF trials, aggregated per wind data source.

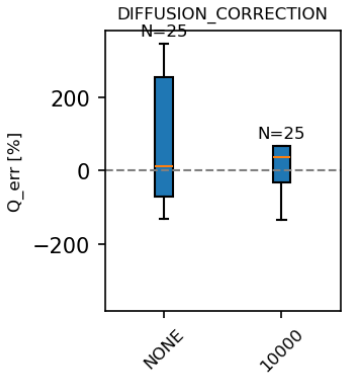

Figure 5.55: Boxplot of the integrated source rate error over the range of simulated background-free WRF emission trials, aggregated per diffusion correction constant.

Finally, trying to add the diffusion correction on WRF observations shows a significant improvement (Figure 5.55). However the applicability of such a correction is limited by the fact the correction constant K needs to fit the species' constant of turbulent diffusion as close as possible in order to effectively reduce the underestimation bias (Equation 2.4.6).

5.3. Estimating the yearly methane emissions in the Permian basin

The case study will focus on the Permian basin, a region thoroughly investigated by many authors as discussed in subsection 5.3.1, and will evaluate total yearly emissions based on the TROPOMI methane product and the optimal settings found so far (subsection 5.3.2. The results will then be compared to various other studies over the same region in order to assess the extent to which this implementation of the divergence method agrees with accepted methods.

5.3.1. Comparison to previous estimates

The Permian Basin, a major oil and gas (O&G) production region in the United States (Maasakkers et al. 2021), has been the subject of several studies aiming at estimating methane emissions using a range of different methods, including divergence, inversion, and inventory-based approaches. These case studies provide valuable benchmarks for evaluating the results of this thesis and understanding the variability in emission estimates.

Table 5.9: Estimates of the Permian methane emission rates (Tg/year) in literature, including reported uncertainties (+-), for the year 2019, 2020 and 2021. Variations in the studies' methods or assumptions are indicated in parenthesis and included for completeness.

	year	2019		2020		2021	
source	method	[Tg/yr]	+-	[Tg/yr]	+-	[Tg/yr]	+-
Roberts et al. 2023 (E1)	divergence	3.06	0.66	2.39	0.55	2.67	0.54
Roberts et al. 2023 (E2)	divergence	3.1	0.7	2.4	0.6	2.7	0.5
Veefkind et al. 2023	divergence	3	0.7				
Liu et al. 2021	divergence	3.06					
Schneising et al. 2020	inversion	3.18	1.13				
Zhang et al. 2020 (1.2Tga)	inversion	2.9	0.5				
Zhang et al. 2020	inversion	3.2	0.5				
Varon et al. 2023	inversion	4.3	1.1				
McNorton et al. 2022	inversion	2.3	0.5				
Shen et al. 2022 (0.6Tga)	inversion			2.9	0.4		
Shen et al. 2022 (2.2Tga)	inversion			3.7	0.5		
Lu et al. 2023	inversion	2.95	0.45	3.4	0.4		
EPA GHGI from Balcombe et al. 2018	inventory	0.62				0.93	#N/A
Omara et al. 2024	inventory					2.9	0.65

5.3.2. Region evaluation

The Permian was studied with an outer domain centred around $(32^oN, 103^oE)$, an extent of $R = 8^o$ in order to capture the wider surroundings and get the best out of the pressure-correction (see Figure 2.4.5) as shown in Figure 5.56. A coarser resolution of $r = 0.1^o$ was used instead of the TROPOMI-like $r = 0.05^o$ in order to run the analysis in a timely manner. This was done over a period of five years starting in 01/01/2018 and ending in 31/12/2024 which covers the studies shown in Table 5.9 with the notable exception of year 2022 due to a runtime issue in the presampling phase. The rest of the settings were chosen based on the results of subsection 5.2.6: A monthly-averaging scheme was used in order to capture an error estimate (as per subsection 4.5.4). The estimation settings used the flux-averaged divergence (E2) estimator with a combination of gradient directions and a combination of gradient order in order to maximise the available pixels each month and mitigate the short time-averaging period. The only correction used was the pressure-based background reduction method based on monthly data correlations and the GEOS-FP 50m wind field was used as the effective wind field on sensitivity analyses shown in Figure 5.54. Finally the emission maps will be integrated for all pixels within the area highlighted in Figure 5.57. Estimations for the sub-basins such as Midland are not computed since a more limited number of studies have been done for these individual areas.

Figure 5.56: Latitude-Longitude domain of the TROPOMI Permian region of interest

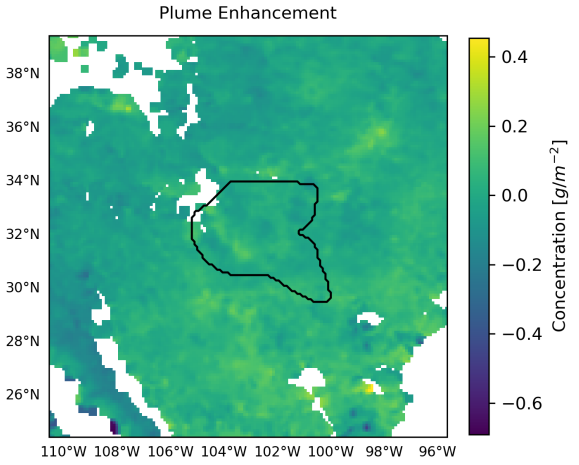

Figure 5.57: Domain boundaries of the Permian basin

The monthly time-series obtained is shown in Figure 5.58 along with a 4-month moving average (dot-

ted) and yearly estimations from Roberts et al. 2023 using a similar E2, 4th-order gradient divergence method. The wide variation in estimates, often negative, is a direct result of using a monthly averaging scheme but the averaging of all points within a year shows good agreement with estimates from literature on the 2019-2021 period.

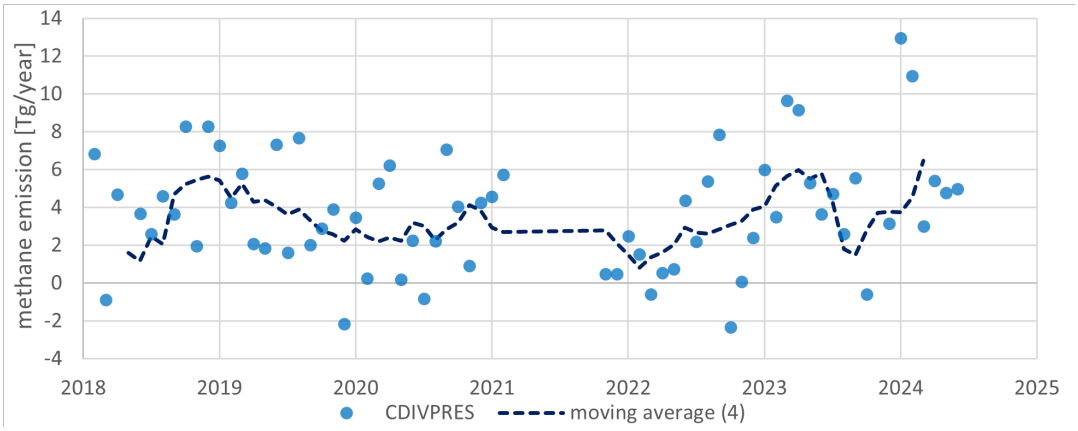

Figure 5.58: Time series of emission estimates over the whole Permian basin for the 2018-2024 period using monthly-averaged fluxes DIV method and pressure-correction

The average and standard deviation of the variability of the monthly estimates are shown per year in Figure 5.59 along with some estimations from literature and their uncertainty where divergence methods are shown in □ markers and inversions in ◊ markers. The yearly average of Permian emission estimates consistently lies within the uncertainty range of both inversion and divergence estimates from independent studies giving good confidence that this implementation is applicable for real TROPOMI CH4 data. The high uncertainty shown in our case is due to the few points considered (12 per year) and restriction to monthly flux-averaging. A better uncertainty estimation is thus needed for further discussion (see subsection 4.5.4).

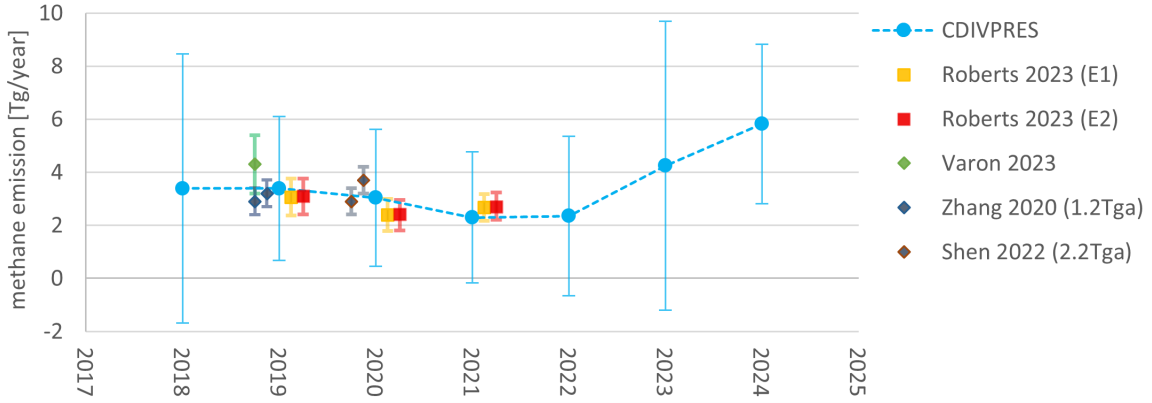

Figure 5.59: Yearly average of the estimates of Permian emissions using using the pressure-corrected monthly-averaged E2 estimator (CDIVPRES) and estimates from literature

A broader comparison can be done by averaging all estimates, including bottom-up estimations, from the reference studies shown in Table 5.9 and showing their variability with error bars in Figure 5.60. The results for 2019 yield an emission estimate of $Q_{avg} = 3.39$ [Tg/y] with a variability of ± 2.72 [Tg/y] compared to the average reference values of $Q_{ref} = 2.88$ [Tg/y] which places it between the 3.0 ± 0.7 [Tg/y] divergence estimate of Veefkind et al. 2023 and the 4.3 ± 1.1 [Tg/y] inversion estimate of Varon et al. 2023. Similar results are obtained for 2020 with $Q_{avg} = 3.04$ [Tg/y] compared to references of $Q_{ref} = 2.39$ to 3.7 [Tg/y]. Due to the missing data for 2021, the results shows a slight underestimation with $Q_{avg} = 2.29$ compared to top-down estimations of $Q_{ref} = 2.67$ to 2.90 [Tg/y]. Overall, comparison

of the yearly averaged emissions over the Permian basin using our configuration and implementation of the divergence method shows good agreement with literature. The results for the total period of 2018-2024 can thus be discussed with good confidence that the yearly-averaged monthly estimates of emissions in the region are representative of the real emissions of the Permian basin for those years.

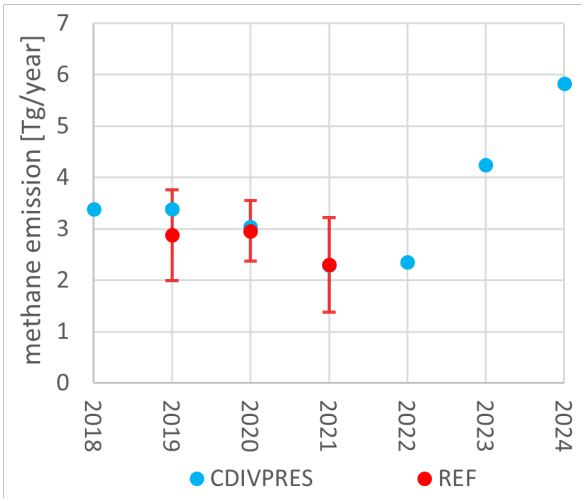

Figure 5.60: Yearly average of the estimates of Permian emissions using using the pressure-corrected monthly-averaged E2 estimator (CDIVPRES) and aggregated estimates from literature

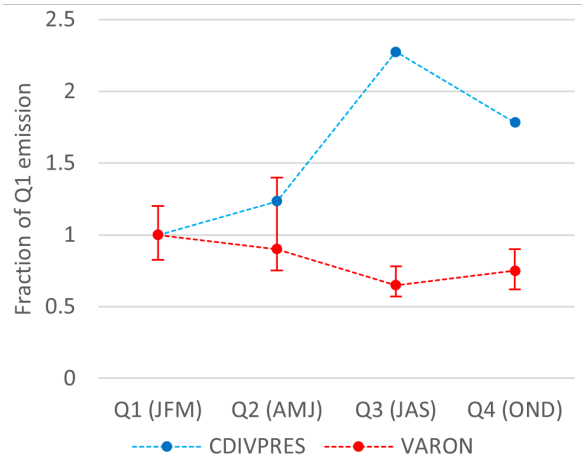

Figure 5.61: Seasonality of Permian emissions based on the pressure-corrected monthly-averaged E2 estimator (CDIVPRES)

Over the 2018-2021 period, a steady decrease of -32.3% is observed. This was also noted by Varon et al. 2023 which attributed it in part to "the reduction in new wells entering production during the COVID-19 pandemic". Furthermore, efforts from the states of Texas and New Mexico to reduce methane intensity, the ratio of gas emitted compared to the gas sent to market, to 2% by 2026 ((NMAC) 2021) seem to encourage O&G companies to keep their emissions steady while increasing production (Varon et al. 2025). By contrast, the 2021-2024 period shows a steep increase of 154% in total emissions. Although Varon et al. 2025 showed a slight up tick of 0.5 [Tg/y] from 2021 to 2022, no increase was seen for 2023 and no studies have investigated the Permian region in 2024. This may indicate that the initial improvements on efficiency of the O&G installations have reached their limits for the operators of the region while the production and demand for locally-sourced natural gas keeps increasing.

Finally, the weekly inversions estimations by Varon et al. 2023 and Varon et al. 2025 revealed a strong seasonal variability in the region. It was seen that CH4 emissions are highest in the winter months and decrease by as much as 35% in the summer. Looking at the estimates aggregated per quarter instead of per year (Figure 5.61) lets us compare the measure of seasonal variation in emission for our estimates (CDIVPRES) and Varon et al. 2025, expressed in fraction of the first quarter in order to exclude year-to-year variations. Interestingly, the trend observed by our estimations is the opposite from the one seen by Varon et al. 2025. This is likely due to the low number of data points considered in our case since the estimates are done monthly instead of weekly and the very wide range of month to month variability seen in Figure 5.58. It is possible however that the trend seen in Figure 5.61 is due to a systematic seasonal bias of the pressure-corrected divergence method which should be verified by further studies.

6

Conclusions and Recommendations

This final chapter will summarise the conclusions of the synthetic analysis in section 6.1 and of the case study in section 6.2. Possible future improvements to the method will be discussed in section 6.4.

6.1. Conclusion from synthetic observations

The aim of the analysis conducted with the synthetic Gaussian and WRF-Chem observations was to quantify the relative performance of methodology variations proposed in literature for trace gas emission estimations using the divergence method. Three key areas of interest were identified and explored in depth namely the choice of numerical order for the approximation of the gradient approximator, the choice of order of operations in the gradient computation and averaging steps (estimator choice) and the choice of background-removal method for methane.

Research sub-question 1 (SQ1): *"Which of the numerical gradient approximations order (4 or combination of 2+4 i.e. 'combo') yields the most accurate estimates for synthetic, background-free simulated TROPOMI methane observations?"*.

The conclusion of this first research sub-question of this thesis is that either the fourth-order or combination of orders perform better than the second order estimation. Which one of these two should be used depends on the use-case and objectives of the study: if one wants to create a general mapping of an area and capture the spatial distribution of emissions, especially on short time-scales (e.g. day, week, months) then the combo method is more fitting. Conversely, studies aiming at high-confidence source estimation over long time periods are better suited to using the fourth-order approximation.

Research sub-question 2 (SQ2): *"Which of the estimators (averaged divergence, flux-averaged divergence or averaged directional derivative) yields the most accurate estimates for synthetic, background-free TROPOMI-like methane observations?"*.

In terms of estimator performance, the directional derivative (DD) method does not seem to provide any advantage over the standard divergence (DIV) approaches. Moreover, the E2 variant generally outperforms E1 in pixel-wise accuracy, although the difference is less pronounced than in the Gaussian plume tests. Interestingly, while E2 provides the most accurate spatial emission patterns, E1 and DD can occasionally yields better total emission estimates, which may be influenced by specific noise conditions or sampling artefacts. The main underlying reason for these differences is the sensitivity of E1 and DD to missing data, where each missing pixel produces a large missing chunk in the emission estimation field resulting in underestimations. Additionally, curved or misaligned wind fields and diffusion have been observed to cause aliasing artefacts which need to be averaged out in the divergence maps.

Research sub-question 3 (SQ3): *"Which of the background correction methods (pressure correction or topography correction) yields the most accurate estimates for synthetic TROPOMI-like methane observations?"*

The last results from the investigation of individual parameters showed that real, structured, backgrounds drive the errors of the divergence method on methane observations and that the only globally applicable correction available at this time is based on monthly surface pressures since the topography corrections depends on an unknown fitted factor which cannot determined from the observations alone.

Research sub-question 4 (SQ4): *"Which combinations of numerical gradients, estimators and background corrections parametrisations yields the most accurate estimates of time-averaged and spatially integrated emissions for simulated TROPOMI methane observations?"*

The conclusions derived from investigating the parameters individually holds when combining the settings pair-wise. The influence of one parameter over another in the overall performance is largely obscured, if present, by the fact that the magnitude of the impact of some parameters is much larger than others. The choice of background correction method is seen to have the largest effect on accuracy ($\pm 3000\%$) due to the inapplicability of the topography correction. The choice of estimator remains important with differences of $\pm 5\%$ between the DD and E2 methods while the influence of the gradient order approximation is minimal ($\pm 1\%$).

6.2. Conclusion from Permian case-study

A case study of the Permian basin was then conducted. First to ascertain whether the conclusions drawn from section 6.1 are indeed applicable for real TROPOMI CH4 observations and second to investigate the, less studied, recent trends in emissions of the region.

Research sub-question 5 (SQ5): *"Are the yearly emissions, estimated through this implementation of the divergence method over the Permian basin, consistent with independent studies of the region?"*

The yearly averaged emissions over the Permian basin using the combined fourth and second order gradient, monthly flux-averaged estimator and pressure-corrected column densities divergence method shows good agreement with literature. The mean of the emission estimations landed within the uncertainty range of other top-down studies for 2019 and 2020 and was always between the lowest and highest yearly estimates found in literature. This consistency gave good confidence that, while the monthly variability of the results is high, the divergence method implemented in this thesis is a valid estimation method for TROPOMI methane emissions.

Research sub-question 6 (SQ6): *"How do the yearly methane emission estimates for recent years in the Permian basin, derived in this study, compare to temporal patterns reported in previous literature?"*

Finally the study period was extended from 2018 to 2024 in order to observe the overall trends of the region. In particular, the seasonal trend seen in our estimations strays far from the one seen by Varon et al. 2025 which probably indicates a systematic seasonal bias of the pressure-corrected divergence method. Looking at the yearly trends, a steady decrease of -32.3% was observed from to 2022 which aligns with other literature estimates. Conversely, analysis of the 2022 to 2024 period which has not yet been studied through other methods revealed a steep increase of 154% in total emissions.

6.3. Research conclusion

The overall objective and research question this thesis aimed to answer were:

Research objective: *"Investigate the impact of methodology and parameter variations in the generation of an emission map via the Divergence Method based on TROPOMI methane observations."*

Research question (RQ): *"Which combinations of divergence method parametrisations yields the most accurate estimates of emission for TROPOMI methane observations?"*

To this end, this thesis made several contributions to the literature. First, it identified the pitfalls of the topography correction when applied globally and higlighted the need for an efficient and reliable background correction. Second, it corroborated the findings of Roberts et al. 2023 regarding the order of operations of the estimator and reaffirmed that flux-averaging is a more accurate and robust method than either the divergence-average or directional derivative methods. Thirdly it presented a comprehensive and fair comparison of various gradient approximation schemes, estimators and corrections with the same dataset, sources and conditions such that these could be compared and jointly optimised.

This study also provided additional estimates of the Permian basin's emission in the 2019-2023 period which, despite being somewhat limited by the inherent uncertainty of the DIV method, supported evidence from previous analyses and further expanded it to the 2023-2024 years which revealed a surprisingly significant up-tick in methane emissions of that region. The ability to spot such a trend with a method that has a small computational cost while agreeing with much more advanced and expensive inversion methods highlights the value of the divergence method. The lack of user-defined domain-specific parameters also allow this divergence method to be applied globally and yield an early look at the emission trends of many regions of interest.

6.4. Recommendations

This section will first discuss methodology variations that were not investigated in this thesis but may have the potential to yield better results than the 'optimal' configuration used here (subsection 6.4.1). Known limitations of the current implementation will the be addressed in subsection 6.4.2. Finally, recommendations for future studies will be motivated in subsection 6.4.3.

6.4.1. Divergence method variations

First, central gradient approximations could be investigated. These may help to mitigate the aliasing artefacts seen in subsection 5.2.4 and reduce the gradient noise by including the central pixel in e.g. a third or fifth order directional derivative to replace the second and fourth order approximations over the same area. Indeed, such a central gradient would not cause any more missing data in the emission map while providing a reduction in the order of the truncation error. Second, the implementation of a plume mask for the data selection of the pressure correction could be used instead of the 25-percentile binning. This would more directly exclude the pixels meant to be enhanced resulting in better background reduction but would only be applicable for very large point sources. Third, a denoising step such as the one described in Hakkarainen et al. 2022 may reduce the influence of systematic and random errors in the data. This can be achieved using by spatially averaging the image with a simple mean filter or a more complex method such as block-matching and filtering (BM3D).

6.4.2. Current limitations

The lack of direct uncertainty estimation is the main limitation of the current implementation of the divergence method. As seen in section 5.3, the measure of variability is not representative of the accuracy of the method and requires sub-optimal estimations and computationally heavy time-series. A major overhaul of the codebase developed would be needed to include error propagation: a way to propagate the errors throughout every method step and yield a pixel-wise uncertainty associated with each pixel value. This pixel-wise uncertainty can be aggregated in the integration phase using the existing pipeline described in Equation 4.13 for WRF residual deviations. Alternatively, an ensemble approach using the sensitivity analysis data gathered could be used to derive uncertainty margins for the integrated emission estimate directly based on the ground-truth given by the WRF residuals. This would require more complete sensitivity runs across multiple geographical locations in order to include the regional impact of confounding factors such surface albedo and the presence of water bodies into the uncertainty estimate.

A potential source of inaccuracies in the current method are the geometrical approximations assumed throughout. Geometrical inaccuracies in the resampling (subsection 4.3.5) and pixel-area (Equation 4.10) computations could be amended with better, geodesy-based, computations which would improve the performance, especially in high-latitude regions. Similarly, using an weighted integration scheme along the domain boundaries instead of fully including or excluding a pixel would reduce the noise in integrated emissions on coarse observations.

That said, the main limitation of this codebase is the RAM limit of the local machine it is run on and the large amount of files being created in intermediate steps. Indeed, since the resampling is done in FORTRAN (f90 version) while the rest of the method is in python3, all the observations presampled need to be outputted to csv files on disk so they can be read by the f90 scripts. These scripts then need to output their own csv files that must be read and deleted by the next block of python code. The resampling process thus creates large amounts (a few gigabytes to terabytes per run) of files that could be avoided by passing these observations as variables instead. The large amount of memory

required in this operation often slowed down or crashed the program for large domains and limited the resolution 0.1^o in most cases. Furthermore, splitting the divergence estimation script into two parts: one that preprocesses the resampled observations, performs background reduction and computes the fluxes while the second performs flux-averaging and gradient computations would significantly increase the speed of the E2 estimator which could take advantage of the multi-core processing in place for the other methods.

6.4.3. Future studies

The main foreseen application of the divergence method within SRON is its use on global observations. This thesis showed it is applicable to any one region on earth as seen with the Russian WRF-Chem synthetic observations and Permian TROPOMI observations but further work is needed to prove its applicability in a wider and more representative range of geographical locations. Furthermore, the RAM limits mentioned prohibit the current implementation from being run globally everywhere at once, which would provide an invaluable emission map of yearly worldwide emission estimates. Such a map could be obtained by splitting the domain into sub-domains of e.g. $5\text{x}5^o$ which can be processed independently and stitched together. Although this subdivision approach could result in artefacts along the sub-domain boundaries, it would also yield a more accurate pressure-correction and is thus the recommended path forward.

Finally, further research should provide additional evidence for the recent increase in emissions of the Permian basin found in this thesis with independent methods in order to confirm or deny the significant increase and allow mitigation strategies to be put in place. It is thus recommended that further studies take a closer look at the recent years' methane emissions of the Permian basin to assess whether the increase revealed here is confirmed by other methods and, if so, what are the underlying reasons for the change in emission trends observed.

References

Alvarez, Ramón A. et al. (July 2018). “Assessment of methane emissions from the U.S. oil and gas supply chain”. en. In: *Science* 361.6398, pp. 186–188. ISSN: 0036-8075, 1095-9203. DOI: 10.1126/science.aar7204. URL: https://www.science.org/doi/10.1126/science.aar7204 (visited on 01/13/2025).

Apituley, Arnoud et al. (2022). *Sentinel-5 precursor/TROPOMI Level 2 Product User Manual Methane*. en.

Balcombe, Paul et al. (2018). “Methane emissions: choosing the right climate metric and time horizon”. en. In: *Environmental Science: Processes & Impacts* 20.10, pp. 1323–1339. ISSN: 2050-7887, 2050-7895. DOI: 10.1039/C8EM00414E. URL: https://xlink.rsc.org/?DOI=C8EM00414E (visited on 01/13/2025).

Beirle, Steffen et al. (Nov. 2019). “Pinpointing nitrogen oxide emissions from space”. en. In: *Science Advances* 5.11, eaax9800. ISSN: 2375-2548. DOI: 10.1126/sciadv.aax9800. URL: https://www.science.org/doi/10.1126/sciadv.aax9800 (visited on 01/13/2025).

Beirle, Steffen et al. (June 2021). “Catalog of NO_x emissions from point sources as derived from the divergence of the NO_2 flux for TROPOMI”. en. In: *Earth System Science Data* 13.6, pp. 2995–3012. ISSN: 1866-3516. DOI: 10.5194/essd-13-2995-2021. URL: https://essd.copernicus.org/articles/13/2995/2021/ (visited on 01/13/2025).

Beirle, Steffen et al. (July 2023). “Improved catalog of NO_x point source emissions (version 2)”. en. In: *Earth System Science Data* 15.7, pp. 3051–3073. ISSN: 1866-3516. DOI: 10.5194/essd-15-3051-2023. URL: https://essd.copernicus.org/articles/15/3051/2023/ (visited on 01/13/2025).

Broquet, Grégoire et al. (Feb. 2018). “The potential of satellite spectro-imagery for monitoring CO₂ emissions from large cities”. en. In: *Atmospheric Measurement Techniques* 11.2, pp. 681–708. ISSN: 1867-8548. DOI: 10.5194/amt-11-681-2018. URL: https://amt.copernicus.org/articles/11/681/2018/ (visited on 01/13/2025).

Commission, European and United States of America (2021). *Global Methane Pledge*. URL: https://www.ccacoalition.org/resources/global-methane-pledge.

Crosman, Erik (Jan. 2021). “Meteorological Drivers of Permian Basin Methane Anomalies Derived from TROPOMI”. en. In: *Remote Sensing* 13.5. Number: 5 Publisher: Multidisciplinary Digital Publishing Institute, p. 896. ISSN: 2072-4292. DOI: 10.3390/rs13050896. URL: https://www.mdpi.com/2072-4292/13/5/896 (visited on 01/14/2025).

Cusworth, Daniel H. et al. (July 2021). “Intermittency of Large Methane Emitters in the Permian Basin”. en. In: *Environmental Science & Technology Letters* 8.7, pp. 567–573. ISSN: 2328-8930, 2328-8930. DOI: 10.1021/acs.estlett.1c00173. URL: https://pubs.acs.org/doi/10.1021/acs.estlett.1c00173 (visited on 01/13/2025).

De Foy, Benjamin and James J Schauer (Feb. 2022). “An improved understanding of NOx emissions in South Asian megacities using TROPOMI NO_2 retrievals”. en. In: *Environmental Research Letters* 17.2, p. 024006. ISSN: 1748-9326. DOI: 10.1088/1748-9326/ac48b4. URL: https://iopscience.iop.org/article/10.1088/1748-9326/ac48b4 (visited on 01/13/2025).

Delfi, Shokufeh et al. (Dec. 2019). “Investigation of aerosols pollution across the eastern basin of Urmia lake using satellite remote sensing data and HYSPLIT model”. en. In: *Journal of Environmental Health Science and Engineering* 17.2, pp. 1107–1120. ISSN: 2052-336X. DOI: 10.1007/s40201-019-00425-3. URL: https://doi.org/10.1007/s40201-019-00425-3 (visited on 01/14/2025).

ECMWF (2025). *ERA-5*. URL: https://www.ecmwf.int/en/forecasts/dataset/ecmwf-reanalysis-v5.

European Commission. Joint Research Centre. (2017). *An operational anthropogenic CO2 emissions monitoring & verification system: baseline requirements, model components and functional architecture.* en. LU: Publications Office. URL: https://data.europa.eu/doi/10.2760/08644 (visited on 01/13/2025).

Freitas, Arthur Dias and Adalgiza Fornaro (Jan. 2022). “Atmospheric Formaldehyde Monitored by TROPOMI Satellite Instrument throughout 2020 over São Paulo State, Brazil”. en. In: *Remote Sensing* 14.13. Number: 13 Publisher: Multidisciplinary Digital Publishing Institute, p. 3032. ISSN: 2072-4292. DOI: 10.3390/rs14133032. URL: https://www.mdpi.com/2072-4292/14/13/3032 (visited on 01/14/2025).

Guanter, Luis et al. (Aug. 2024). “Multisatellite Data Depicts a Record-Breaking Methane Leak from a Well Blowout”. In: *Environmental Science & Technology Letters* 11.8. Publisher: American Chemical Society, pp. 825–830. DOI: 10.1021/acs.estlett.4c00399. URL: https://doi.org/10.1021/acs.estlett.4c00399 (visited on 08/04/2025).

Hakkarainen, Janne et al. (July 2022). “Analyzing Local Carbon Dioxide and Nitrogen Oxide Emissions From Space Using the Divergence Method: An Application to the Synthetic SMARTCARB Dataset”. en. In: *Frontiers in Remote Sensing* 3, p. 878731. ISSN: 2673-6187. DOI: 10.3389/frsen.2022.878731. URL: https://www.frontiersin.org/articles/10.3389/frsen.2022.878731/full (visited on 01/13/2025).

Houweling, S. et al. (May 2015). “An intercomparison of inverse models for estimating sources and sinks of CO_2 using GOSAT measurements”. en. In: *Journal of Geophysical Research: Atmospheres* 120.10, pp. 5253–5266. ISSN: 2169-897X, 2169-8996. DOI: 10.1002/2014JD022962. URL: https://agupubs.onlinelibrary.wiley.com/doi/10.1002/2014JD022962 (visited on 01/13/2025).

Intergovernmental Panel On Climate Change (Ipcc) (July 2023). *Climate Change 2021 – The Physical Science Basis: Working Group I Contribution to the Sixth Assessment Report of the Intergovernmental Panel on Climate Change*. en. 1st ed. Cambridge University Press. ISBN: 978-1-009-15789-6. DOI: 10.1017/9781009157896. URL: https://www.cambridge.org/core/product/identifier/9781009157896/type/book (visited on 01/13/2025).

Jacob, Daniel J. et al. (Nov. 2016). “Satellite observations of atmospheric methane and their value for quantifying methane emissions”. en. In: *Atmospheric Chemistry and Physics* 16.22, pp. 14371–14396. ISSN: 1680-7324. DOI: 10.5194/acp-16-14371-2016. URL: https://acp.copernicus.org/articles/16/14371/2016/ (visited on 01/13/2025).

Jacob, Daniel J. et al. (July 2022). “Quantifying methane emissions from the global scale down to point sources using satellite observations of atmospheric methane”. en. In: *Atmospheric Chemistry and Physics* 22.14, pp. 9617–9646. ISSN: 1680-7324. DOI: 10.5194/acp-22-9617-2022. URL: https://acp.copernicus.org/articles/22/9617/2022/ (visited on 01/13/2025).

Jongaramrungruang, Siraput et al. (Dec. 2019). “Towards accurate methane point-source quantification from high-resolution 2-D plume imagery”. English. In: *Atmospheric Measurement Techniques* 12.12. Publisher: Copernicus GmbH, pp. 6667–6681. ISSN: 1867-1381. DOI: 10.5194/amt-12-6667-2019. URL: https://amt.copernicus.org/articles/12/6667/2019/ (visited on 01/14/2025).

Jongaramrungruang, Siraput et al. (2021). “MethaNet – An AI-driven approach to quantifying methane point-source emission from high-resolution 2-D plume imagery”. In: *Remote Sensing of Environment*. DOI: https://doi.org/10.1016/j.rse.2021.112809.

Koene, E. F. M., D. Brunner, and G. Kuhlmann (June 2024). “On the Theory of the Divergence Method for Quantifying Source Emissions From Satellite Observations”. en. In: *Journal of Geophysical Research: Atmospheres* 129.12, e2023JD039904. ISSN: 2169-897X, 2169-8996. DOI: 10.1029/2023JD039904. URL: https://agupubs.onlinelibrary.wiley.com/doi/10.1029/2023JD039904 (visited on 01/13/2025).

Koene, Erik and Dominik Brunner (n.d.). “Assessment of plume model performance”. en. In: ().

Koene, Erik, Dominik Brunner, and Gerrit Kuhlmann (2021). “Documentation of plume detection and quantification methods”. en. In.

Lauvaux, T. et al. (Feb. 2022). “Global assessment of oil and gas methane ultra-emitters”. In: *Science* 375.6580. Publisher: American Association for the Advancement of Science, pp. 557–561. DOI: 10.1126/science.abj4351. URL: https://www.science.org/doi/10.1126/science.abj4351 (visited on 01/14/2025).

Liu, Mengyao et al. (Aug. 2020). “A new TROPOMI product for tropospheric NO₂ columns over East Asia with explicit aerosol corrections”. en. In: *Atmospheric Measurement Techniques* 13.8, pp. 4247–4259. ISSN: 1867-8548. DOI: 10.5194/amt-13-4247-2020. URL: https://amt.copernicus.org/articles/13/4247/2020/ (visited on 01/13/2025).

Liu, Mengyao et al. (Sept. 2021). “A New Divergence Method to Quantify Methane Emissions Using Observations of Sentinel□5P TROPOMI”. en. In: *Geophysical Research Letters* 48.18, e2021GL094151.

ISSN: 0094-8276, 1944-8007. DOI: 10.1029/2021GL094151. URL: https://agupubs.onlinelibrary.wiley.com/doi/10.1029/2021GL094151 (visited on 01/13/2025).

Lorente, Alba et al. (Jan. 2021). “Methane retrieved from TROPOMI: improvement of the data product and validation of the first 2 years of measurements”. English. In: *Atmospheric Measurement Techniques* 14.1. Publisher: Copernicus GmbH, pp. 665–684. ISSN: 1867-1381. DOI: 10.5194/amt-14-665-2021. URL: https://amt.copernicus.org/articles/14/665/2021/ (visited on 08/03/2025).

Lu, Xiao et al. (Apr. 2023). “Observation-derived 2010-2019 trends in methane emissions and intensities from US oil and gas fields tied to activity metrics”. en. In: *Proceedings of the National Academy of Sciences* 120.17, e2217900120. ISSN: 0027-8424, 1091-6490. DOI: 10.1073/pnas.2217900120. URL: https://pnas.org/doi/10.1073/pnas.2217900120 (visited on 01/13/2025).

Maasakkers, Joannes D. et al. (Mar. 2021). “2010–2015 North American methane emissions, sectoral contributions, and trends: a high-resolution inversion of GOSAT observations of atmospheric methane”. en. In: *Atmospheric Chemistry and Physics* 21.6, pp. 4339–4356. ISSN: 1680-7324. DOI: 10.5194/acp-21-4339-2021. URL: https://acp.copernicus.org/articles/21/4339/2021/ (visited on 01/13/2025).

Maasakkers, Joannes D. et al. (Mar. 2022). “Reconstructing and quantifying methane emissions from the full duration of a 38-day natural gas well blowout using space-based observations”. In: *Remote Sensing of Environment* 270, p. 112755. ISSN: 0034-4257. DOI: 10.1016/j.rse.2021.112755. URL: https://www.sciencedirect.com/science/article/pii/S0034425721004752 (visited on 05/09/2025).

McNorton, Joe et al. (May 2022). “Quantification of methane emissions from hotspots and during COVID-19 using a global atmospheric inversion”. en. In: *Atmospheric Chemistry and Physics* 22.9, pp. 5961–5981. ISSN: 1680-7324. DOI: 10.5194/acp-22-5961-2022. URL: https://acp.copernicus.org/articles/22/5961/2022/ (visited on 01/13/2025).

modelling, global and assimilation office (GMAO) (2025). *GEOS-FP*. URL: https://gmao.gsfc.nasa.gov/GMAO_products/NRT_products.php.

NASA (2025). *GEOS-Chem website*. en. URL: https://geoschem.github.io/index.html (visited on 08/03/2025).

(NMAC), New Mexico Administrative Code (2021). *N.M. Admin. Code § 19.15.27.9 - STATEWIDE NATURAL GAS CAPTURE REQUIREMENTS*. URL: https://www.srca.nm.gov/parts/title19/19.015.0027.html.

NOAA (2025a). *ETOPO global relief model*. URL: https://www.ncei.noaa.gov/products/etopo-global-relief-model.

— (2025b). *Hybrid Single-Particle Lagrangian Integrated Trajectory model by the Air Resource Laboratory*. URL: https://www.ready.noaa.gov/HYSPLIT.php.

Omara, Mark et al. (Sept. 2024). “Constructing a measurement-based spatially explicit inventory of US oil and gas methane emissions (2021)”. en. In: *Earth System Science Data* 16.9, pp. 3973–3991. ISSN: 1866-3516. DOI: 10.5194/essd-16-3973-2024. URL: https://essd.copernicus.org/articles/16/3973/2024/ (visited on 01/13/2025).

Peng, Shushi et al. (Dec. 2022). “Wetland emission and atmospheric sink changes explain methane growth in 2020”. en. In: *Nature* 612.7940, pp. 477–482. ISSN: 0028-0836, 1476-4687. DOI: 10.1038/s41586-022-05447-w. URL: https://www.nature.com/articles/s41586-022-05447-w (visited on 01/13/2025).

Plant, Genevieve et al. (2022). “Inefficient and unlit natural gas flares both emit large quantities of methane”. In: *Science* 377.6614, pp. 1566–1571. DOI: 10.1126/science.abq0385. eprint: https://www.science.org/doi/pdf/10.1126/science.abq0385. URL: https://www.science.org/doi/abs/10.1126/science.abq0385.

Rey-Pommier, Anthony et al. (Jan. 2025). “Mapping $$\text {NO}_{\text {x}}$$ emissions in Cyprus using TROPOMI observations: evaluation of the flux-divergence scheme using multiple parameter sets”. en. In: *Environmental Science and Pollution Research*. ISSN: 1614-7499. DOI: 10.1007/s11356-024-35851-w. URL: https://link.springer.com/10.1007/s11356-024-35851-w (visited on 01/13/2025).

Roberts, Clayton et al. (Nov. 2023). “Avoiding methane emission rate underestimates when using the divergence method”. en. In: *Environmental Research Letters* 18.11, p. 114033. ISSN: 1748-9326. DOI: 10.1088/1748-9326/ad0252. URL: https://iopscience.iop.org/article/10.1088/1748-9326/ad0252 (visited on 01/13/2025).

Rodgers, Clive D. (July 2000). “Inverse Methods For Atmospheric Sounding: Theory And Practice”. en. In: Google-Books-ID: Xv7sCgAAQBAJ.

Saunois, Marielle et al. (July 2020). “The Global Methane Budget 2000–2017”. en. In: *Earth System Science Data* 12.3, pp. 1561–1623. ISSN: 1866-3516. DOI: 10.5194/essd-12-1561-2020. URL: https://essd.copernicus.org/articles/12/1561/2020/ (visited on 01/13/2025).

Saunois, Marielle et al. (June 2024). *Global Methane Budget 2000–2020*. en. DOI: 10.5194/essd-2024-115. URL: https://essd.copernicus.org/preprints/essd-2024-115/ (visited on 01/13/2025).

Schneising, Oliver et al. (Aug. 2020). “Remote sensing of methane leakage from natural gas and petroleum systems revisited”. en. In: *Atmospheric Chemistry and Physics* 20.15, pp. 9169–9182. ISSN: 1680-7324. DOI: 10.5194/acp-20-9169-2020. URL: https://acp.copernicus.org/articles/20/9169/2020/ (visited on 01/13/2025).

Schuit, Berend J. et al. (2023). “Automated detection and monitoring of methane super-emitters using satellite data”. In: *Atmospheric Chemistry and Physics*.

Shen, Lu et al. (Sept. 2022). “Satellite quantification of oil and natural gas methane emissions in the US and Canada including contributions from individual basins”. en. In: *Atmospheric Chemistry and Physics* 22.17, pp. 11203–11215. ISSN: 1680-7324. DOI: 10.5194/acp-22-11203-2022. URL: https://acp.copernicus.org/articles/22/11203/2022/ (visited on 01/13/2025).

Shindell, Drew et al. (Jan. 2012). “Simultaneously Mitigating Near-Term Climate Change and Improving Human Health and Food Security”. en. In: *Science* 335.6065, pp. 183–189. ISSN: 0036-8075, 1095-9203. DOI: 10.1126/science.1210026. URL: https://www.science.org/doi/10.1126/science.1210026 (visited on 01/13/2025).

SRON (2025). *SRON earth group (methane)*. URL: https://www.sron.nl/en/pillars/science/earth/methane/.

Stockie, John M. (Jan. 2011). “The Mathematics of Atmospheric Dispersion Modeling”. In: *SIAM Review* 53.2. Publisher: Society for Industrial and Applied Mathematics, pp. 349–372. ISSN: 0036-1445. DOI: 10.1137/10080991X. URL: https://epubs.siam.org/doi/10.1137/10080991X (visited on 07/31/2025).

Sun, Kang (Dec. 2022). “Derivation of Emissions From Satellite□Observed Column Amounts and Its Application to TROPOMI NO_2 and CO Observations”. en. In: *Geophysical Research Letters* 49.23, e2022GL101102. ISSN: 0094-8276, 1944-8007. DOI: 10.1029/2022GL101102. URL: https://agupubs.onlinelibrary.wiley.com/doi/10.1029/2022GL101102 (visited on 01/13/2025).

Tratt, David M. et al. (2011). “Remotely sensed ammonia emission from fumarolic vents associated with a hydrothermally active fault in the Salton Sea Geothermal Field, California”. en. In: *Journal of Geophysical Research: Atmospheres* 116.D21. _eprint: https://onlinelibrary.wiley.com/doi/pdf/10.1029/2011JD016282. ISSN: 2156-2202. DOI: 10.1029/2011JD016282. URL: https://onlinelibrary.wiley.com/doi/abs/10.1029/2011JD016282 (visited on 01/14/2025).

Tratt, David M. et al. (Nov. 2014). “Airborne visualization and quantification of discrete methane sources in the environment”. In: *Remote Sensing of Environment* 154, pp. 74–88. ISSN: 0034-4257. DOI: 10.1016/j.rse.2014.08.011. URL: https://www.sciencedirect.com/science/article/pii/S0034425714003083 (visited on 01/14/2025).

Varon, Daniel J. et al. (Oct. 2018). “Quantifying methane point sources from fine-scale satellite observations of atmospheric methane plumes”. en. In: *Atmospheric Measurement Techniques* 11.10, pp. 5673–5686. ISSN: 1867-8548. DOI: 10.5194/amt-11-5673-2018. URL: https://amt.copernicus.org/articles/11/5673/2018/ (visited on 01/13/2025).

Varon, Daniel J. et al. (July 2023). “Continuous weekly monitoring of methane emissions from the Permian Basin by inversion of TROPOMI satellite observations”. en. In: *Atmospheric Chemistry and Physics* 23.13, pp. 7503–7520. ISSN: 1680-7324. DOI: 10.5194/acp-23-7503-2023. URL: https://acp.copernicus.org/articles/23/7503/2023/ (visited on 01/13/2025).

Varon, Daniel J. et al. (2025). “Seasonality and declining intensity of methane emissions from the Permian and nearby US oil and gas basins”. In: *EarthArXiv*. DOI: 10.31223/X56B2G.

Veefkind, J. P. et al. (Feb. 2023). “Widespread Frequent Methane Emissions From the Oil and Gas Industry in the Permian Basin”. en. In: *Journal of Geophysical Research: Atmospheres* 128.3, e2022JD037479. ISSN: 2169-897X, 2169-8996. DOI: 10.1029/2022JD037479. URL: https://agupubs.onlinelibrary.wiley.com/doi/10.1029/2022JD037479 (visited on 01/13/2025).

Veefkind, J.P. et al. (May 2012). “TROPOMI on the ESA Sentinel-5 Precursor: A GMES mission for global observations of the atmospheric composition for climate, air quality and ozone layer ap-

plications". en. In: *Remote Sensing of Environment* 120, pp. 70–83. ISSN: 00344257. DOI: 10.1016/j.rse.2011.09.027. URL: https://linkinghub.elsevier.com/retrieve/pii/S0034425712000661 (visited on 01/13/2025).

White, W.H. et al. (1976). "Formation and Transport of Secondary Air Pollutants: Ozone and Aerosols in the St. Louis Urban Plume | Science". In: URL: https://www.science.org/doi/abs/10.1126/science.959846 (visited on 01/14/2025).

Xu, Tianyi et al. (Feb. 2024). "Estimating Hourly Nitrogen Oxide Emissions over East Asia from Geostationary Satellite Measurements". en. In: *Environmental Science & Technology Letters* 11.2, pp. 122–129. ISSN: 2328-8930, 2328-8930. DOI: 10.1021/acs.estlett.3c00467. URL: https://pubs.acs.org/doi/10.1021/acs.estlett.3c00467 (visited on 01/13/2025).

Ye, Xinxin et al. (Apr. 2020). "Constraining Fossil Fuel CO_2 Emissions From Urban Area Using OCO□2 Observations of Total Column CO_2". en. In: *Journal of Geophysical Research: Atmospheres* 125.8, e2019JD030528. ISSN: 2169-897X, 2169-8996. DOI: 10.1029/2019JD030528. URL: https://agupubs.onlinelibrary.wiley.com/doi/10.1029/2019JD030528 (visited on 01/13/2025).

Zhang, Yuzhong et al. (Apr. 2020). "Quantifying methane emissions from the largest oil-producing basin in the United States from space". en. In: *Science Advances* 6.17, eaaz5120. ISSN: 2375-2548. DOI: 10.1126/sciadv.aaz5120. URL: https://www.science.org/doi/10.1126/sciadv.aaz5120 (visited on 01/13/2025).

A

Literature Summary

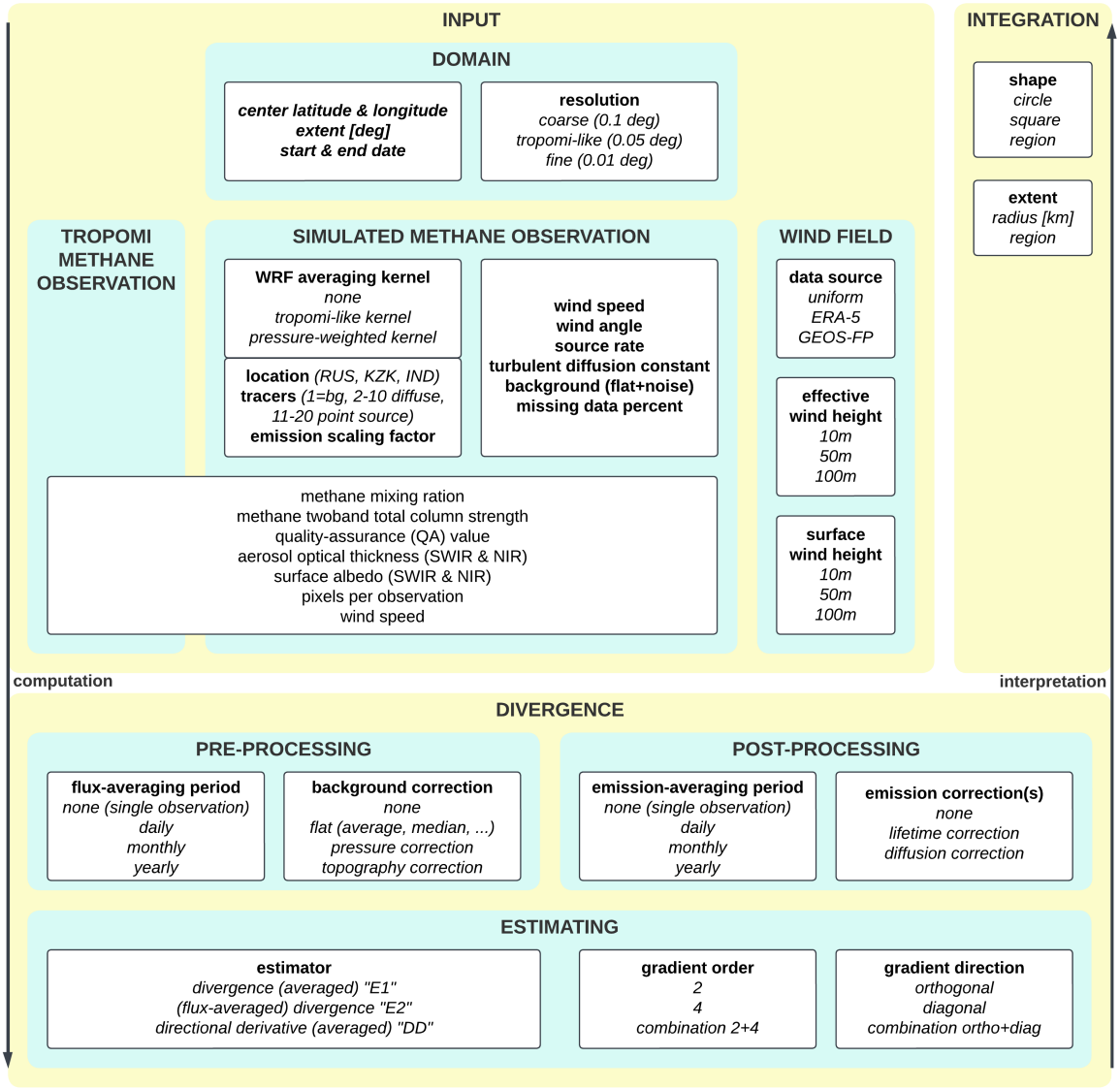

Figure A.1: diagram of method flow and summary of parameter choices

Table A.1: Summary of the parameters, assumptions and choices made in the literature

	Beirle 2019	Beirle 2021	Beirle 2023	Liu 2020	Liu 2021	de Foy 2022	Hakkarainen 2022	Sun 2022	Xu 2023	Roberts 2023	Veefkind 2023	Koene 2024
general												
gas	Nox	Nox	Nox	Nox	CH4	Nox	CO2	CO	NOX	CH4	CH4	CH4
instrument	TROPOMI	TROPOMI	TROPOMI	TROPOMI	TROPOMI	TROPOMI	synthetic (comso-G	TROPOMI	GEMS	synthetic (gaussian	TROPOMI	TROPOMI
INPUTS - domain												
grid size	0.027 latlon	0.025 latlon	0.025 latlon		0.20-0.25 latlon	1km lambert confo	0.05	0.2	0.02		0.05	
location	Riyadh (Saudi Arab	61S-61N	50S-72N			South Asia				Permian	Permian	
time period	12/2017-10/2018	2018-2019	05/2018-11/2021			11/2018-03/2021				2019-2021	2019	
INPUTS - CH4 product												
destriping	NA	NA	NA	NA	yes	NA	NA	NA	NA	NA		
albedo correction	NA	NA	NA	NA	yes	NA	NA	NA	NA	NA		
averaging kernel	NA	NA	NA	NA	no	NA	NA	NA	NA	NA		
elevation corrected	NA	NA	NA	NA	yes	NA	NA	NA	NA	NA		
INPUTS - filtering												
qa	0.75	0.75				0.7		0.7 NO2 & 0.5 CO				
CF	0.3	0.3										
SZA	NA	65	65						65			
VZA	NA	NA	56									
INPUTS - wind field												
product	EMCWF	EMCWF ERA5 6h 1(	EMCWF ERA5 6h 500m			ERA5	ERA5	ERA5	ERA5	ERA-5	ERA5	
resolution [deg]						1	0.1	0.25			0.25	
height	fixed 450m abive g	interpolated 300m	300 m AGL	500m		100m	900-950-1000 hPa	10,100m	800-1000 hPa	500m	14 lvls between 60(	500m
criteria		M>=1										
fluxes **w**	>2 m/s	> 2 m/s		1 < w < 10 m/s	1 < w < 10 m/s				>2m/s	> X ?		> X ?
pressure **p**	?	EMCWF ERA5 6h 1deg										
temperature? **T**	?	EMCWF										
DIV - preprocessing												
background correction	5th percentile	none			CAMS EAC4 10th percentile					pressure	pressure	
flux averaging					no	no		no		yes		
DIV - estimator												
gradient order	4				2	2,4		2		2,4	2,4	
gradient direction	ortho				ortho	ortho		ortho		ortho		
estimator	DIVE1	DIVE1	DD		DIVE1	DIV		DD		DIVE1, DIVE2		
DIV - postprocessing												
lifetime **τ**	4 +- 1.3		1.40 +- 0.24		inf	4 to 9 h	inf		4h or calculated from downwind line densities			
scaling factor **L**	1.32 +- 0.26	function										
constant of turbulent diffusion **K** [m2/s]										40		50-100
ratio **K/w**										10-400		
AMF correction		none	1.61 +- 0.32									
σ BM3D							4,8,10,15,30					
topography correction			H=1.5km					H=fit				
integration												
peak fititeration	semi-auto	auto										
peak fitpre-classification	none	multi-step										
peak fit function	linear bg + 2D gaus	linear bg + 2D gaussian				2D gaussian - bg						
peak removal	substracted	+-2 sigma to NAN										
peak stops after		<4% of initial										
integration radius **r** [m]		22 km	15 km			150km	0.1deg	60km	1deg	10^2 - 10^5	10km	

B

Codebase flowcharts

B.1. Variable-File flow diagram

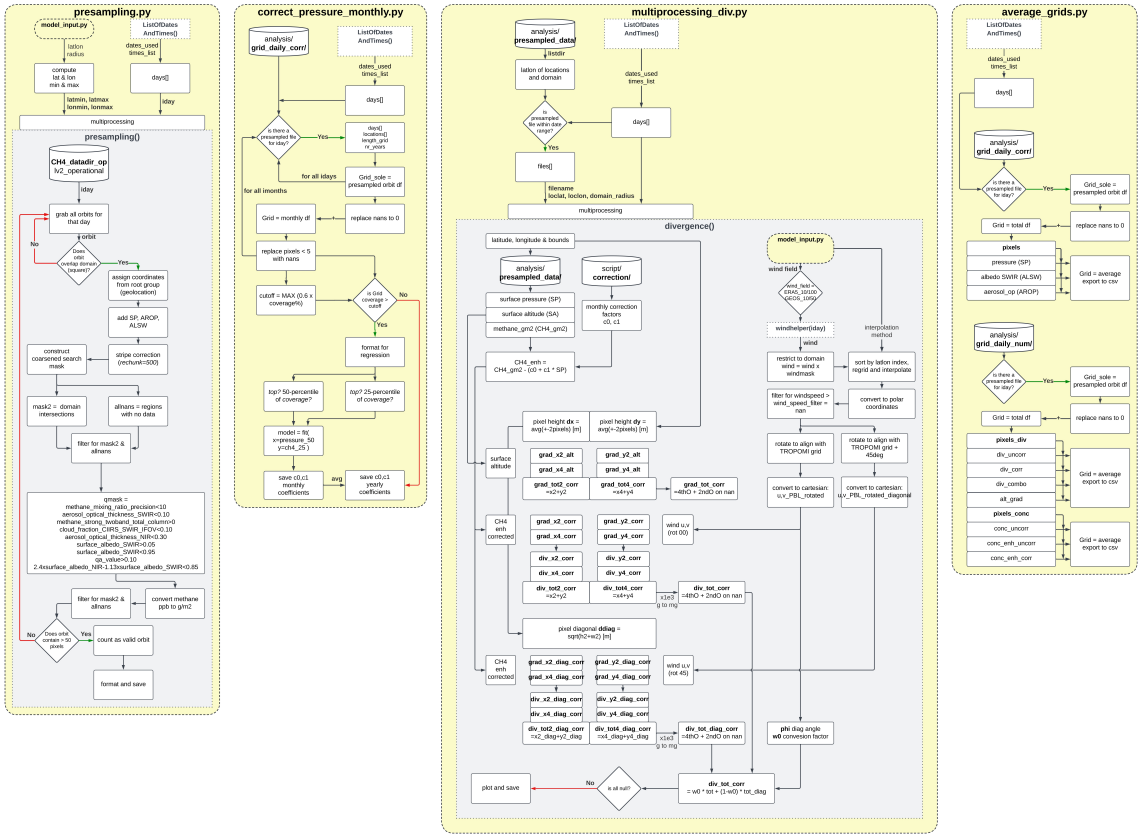

Figure B.1: Function call and file organisation

B.2. Functional flow diagrams

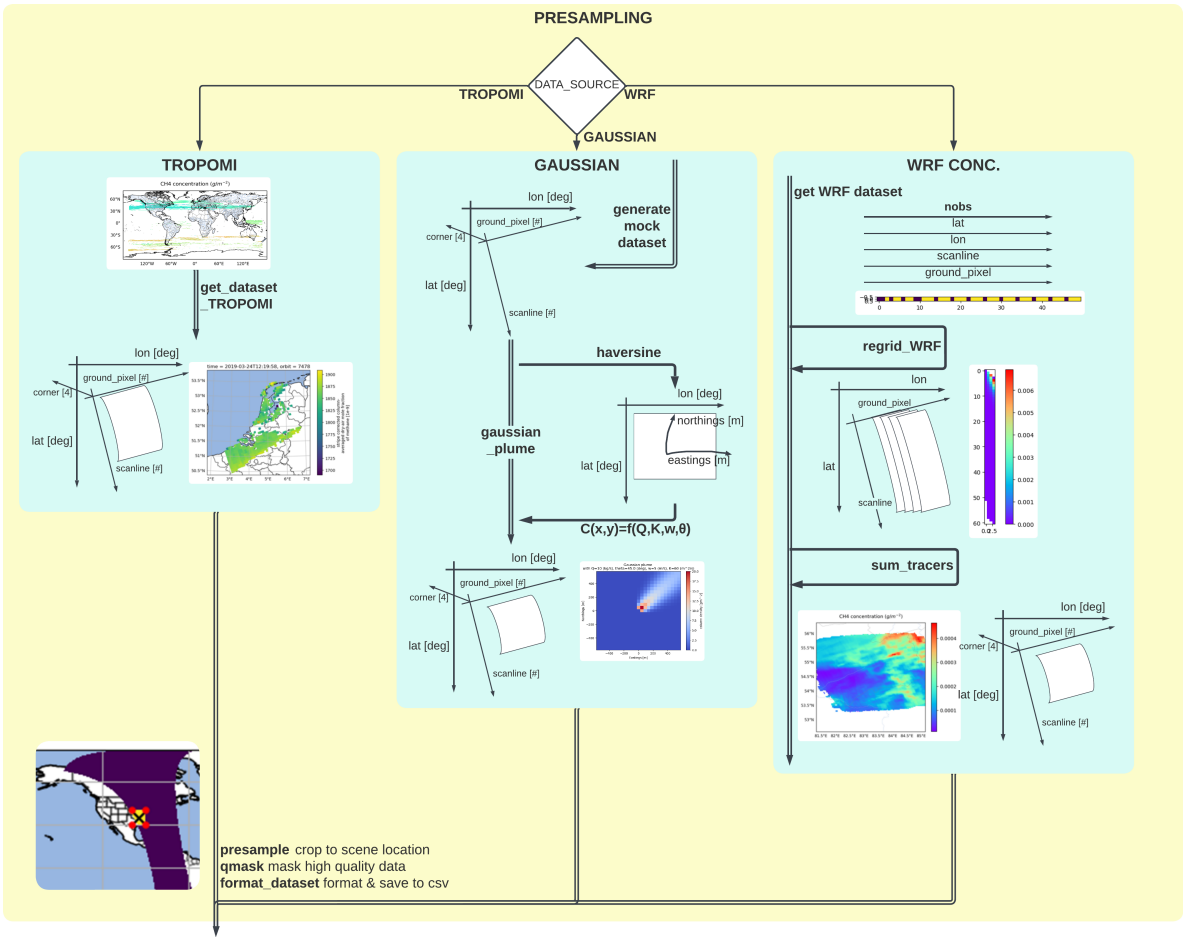

Figure B.2: diagram of presampling flow and processing steps for each data source

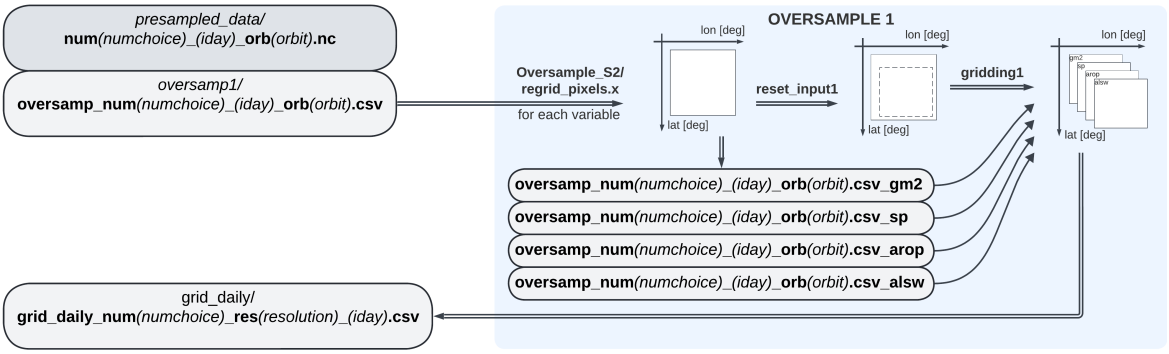

Figure B.3: diagram of concentration and support variables oversampling flow

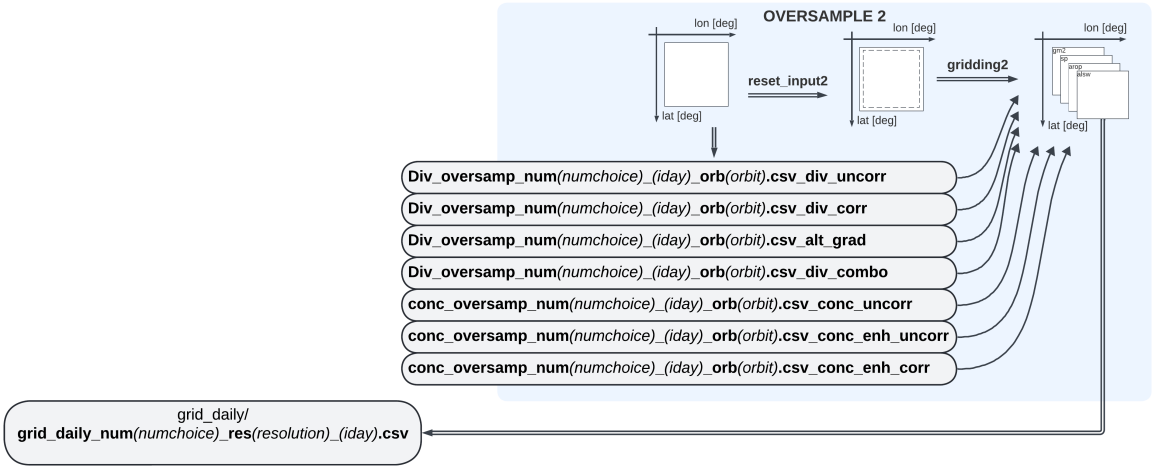

Figure B.4: diagram of emission and resulting parameters oversampling flow

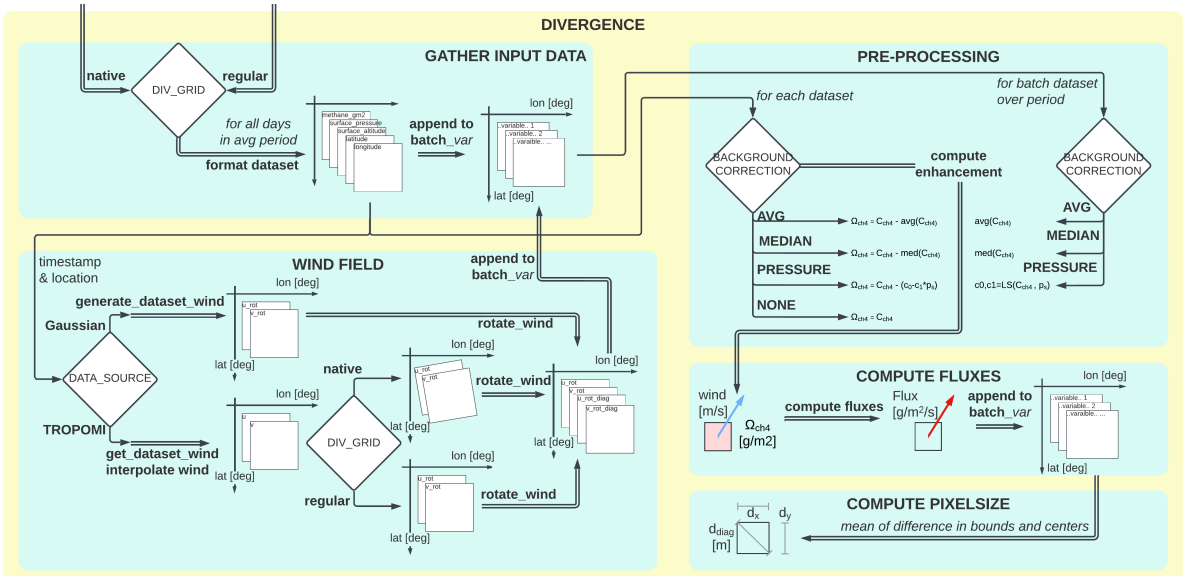

Figure B.5: diagram of divergence averaging and corrections flow

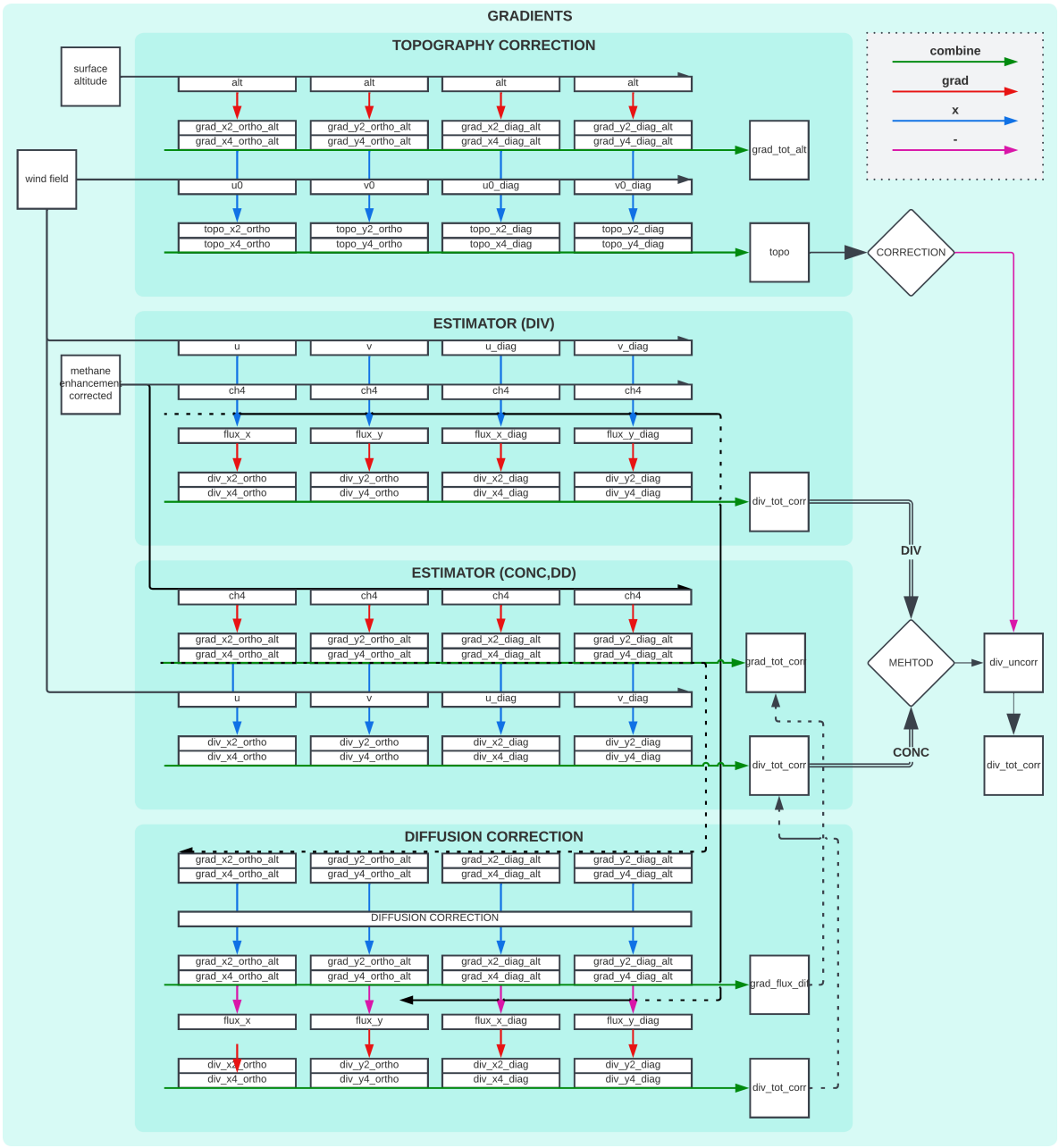

Figure B.6: diagram of gradient computations and aggregation flow